Russian Chemical Reviews **84** (5) 498 – 539 (2015) © 2015 Russian Academy of Sciences and Turpion Ltd

DOI 10.1070/RCR4411

Stability and thermal evolution of transition metal and silicon clusters

V A Polukhin,[a, b] N A Vatolin [a]

[a] *Institute of Metallurgy of the Ural Branch, Russian Academy of Sciences ul. Amundsena 101, 620016 Ekaterinburg, Russian Federation*
[b] *Institute of Materials Science and Metallurgy of the Ural Federal University named after the First President of Russia B N Yeltsin ul. Mira 28, 620002 Ekaterinburg, Russian Federation*

The results of computer simulation studies of transition metal and silicon clusters published in the last decade are summarized. Comparative analysis of the stability and thermal evolution of nanoclusters is performed depending on the preparation method, type of bonds, atom packing, coherence of the constituent nanofragments, surface morphology and change in the relationship between the short- and long-range ordering with increasing size. Taking account of the substrate nature and dimensionality of the cluster disperse systems being simulated, most important structure-dependent kinetic and mechanical characteristics are discussed, including specific temperature ranges of disordering corresponding to isomerization and quasi-melting.
The bibliography includes 263 references.

Contents

I. Introduction 498
II. Nanoclusters. Size effects 500
III. Simulation of the structure of transition metal nanoclusters 502
IV. Thermal stability and size effects during heating of isolated clusters: isomerization, order – disorder transition, hysteresis 507
V. Specific details of thermal size effects in the cluster/substrate systems 513
VI. Stability and thermal size effects of silicon clusters determined by the specific character of covalent bonds 529
VII. Conclusion 535

I. Introduction

The achievements of fundamental science in the studies of functional materials implemented in modern technologies constitute the basis for progress in a number of fields such as information technology, high-temperature chemistry, transport and space technology. Development of such technologies implies the possibility of efficient control over the formation of material structure at the atomic and molecular level, diagnosis of material characteristics with allowance for quantum effects along all (or selected) dimensions and self-assembly of nano-sized fragments or particles as elements of dissipative systems.[1, 2]

V A Polukhin Doctor of Physical and Mathematical Sciences, Chief Researcher at the IMET UrB RAS, Professor at the IMMt UrFU. Telephone: +7(343)232 – 9091, e-mail: pvalery@nm.ru
N A Vatolin Academician, Chief Researcher at the IMET UrB RAS. Telephone: +7(343)267 – 9421, e-mail: vatolin@imet.mplik.ru
Current research interests of the authors: theory of liquid state, physical chemistry of metallurgical processes, structure and properties of metal melts.

Received 17 May 2013
Uspekhi Khimii **84** (5) 498 – 539 (2015); translated by Z P Svitanko

The design of new materials (nanoalloys, fullerites and metal carbon, supramolecular, cluster, nanostructured and heterostructured multicomponent systems) and development of high-resolution experimental methods of structure analysis [scanning tunnelling (STM) and atomic force (AFM) microscopy] are factors that have determined the formation of a new area of materials sciences based not only on achievements of technology but also on the computer methods for the phase formation control and examination and quantum chemical calculation methods.

The control over material properties can be efficient only under thermodynamically non-equilibrium conditions with formation of specific dissipative structures that are homogeneous on the macroscopic scale. The cluster state of matter, which is intermediate between the atomic/molecular and phase states, can serve for the design of innovative materials. This refers, in particular, to the cluster-disperse heterostructured materials possessing unique characteristics and manufactured using critical technologies with controlled heat and mass transfer at the stages of condensation, nanocluster assembling, intense clustering, relaxation annealing, quenching, ion plasma treatment, *etc*.[3 – 7]

Effective planning of experiments on the synthesis of inorganic nanomaterials with specified functional characteristics requires the development of adequate microscopic

models proceeding from a new principle of structuring: from an atom *via* a cluster to the amorphous aperiodic quasi-crystalline nanostructure rather than from the traditional atom–crystal paradigm. These models rely on the information on the electronic structure and the nature of interatomic interactions in nanomaterials gained by means of modern computational methods — molecular dynamics (MD) and Monte Carlo (MC) methods — which serve as the scientific base of nanotechnologies, together with the quantum theory of interparticle interactions.[8–13] These methods deal with objects at the atomic and molecular level; they do not concern the subatomic level of elementary particles (electrons, positrons, photons) and do not violate the Heisenberg principle.

The experimental studies of the physicochemical processes at the atomic and molecular level are highly complicated due to complexity and high cost of the equipment and due to difficulty of synchronization of the temporal scales of the processes involved (femto, pico and macro). The use of traditional analytical approaches is also faced with difficulties (for example, the undecidable many-body problem). In view of this, it is the computer simulation using physically substantiated interparticle interaction potentials that serves to elucidate the key regularities of the formation and growth of nanoclusters, morphological features of the surface, successive formation of coordination spheres and structural transitions.[9, 13–22]

Research into the mechanism of cluster formation and growth as the initial stage of condensation in the vapour–gas medium or crystallization in melts gives the key to the understanding of the origination and formation of phase states depending on the thermodynamic parameters of primary nucleation.[14] The complexity of generation of functional clusters is related to the fact that it is difficult to meet the basic requirements placed on them, namely, the cluster should have a specified shape and a perfect interface structure.

A topical problem faced by implementation of nanotechnologies is not the proper synthesis of clusters but rather attainment of the thermodynamic stability and durable service characteristics. Stabilized clusters are necessary elements of the developing nanotechnologies.

Molecular dynamic studies of the thermal stability of nano-sized metal clusters with an optimal ratio of non-crystalline and crystalline coordinations in the structure are topical for both fundamental science and technology. Combination of investigations along these lines[14–17] opens up prospects for practical application of the obtained results, in particular, for planning of real experiments on the production of new disperse materials with a set of physicochemical, magnetic and optical characteristics needed for the design of new electronic devices indicating transition to a new miniaturization level, *viz.*, from micro- to nano-range. Nanoclusters of transition metals attached to substrates and arranged to two-dimensional structures can serve as functional elements with a high information capacity or catalytic activity. For example, the use of nanodispersed catalysts based on Ni, Co, Mo and W nanoclusters sharply enhances some processes such as catalytic hydrocracking, dewaxing of heavy oil fractions, hydroisomerization of petrol fractions for the production of high-octane fuels, hydrotreatment, hydrogenation and dehydration of methylphenylcarbinol, while the use of nanoclusters of platinum group metals (Pt, Ag, Ru, Pd) accelerates hydrocarbon reforming, isomerization and hydrogenation.[18]

The efficiency of catalysis (the stationary rather than dynamically fragmented version of the catalytic system) is determined by the cooperative effect: the catalytic activity is inherent not in the separate stable clusters of perfect shape but in the thermally stable groups of clusters, 2D spacers, arranged on the support surface. Naturally, the activity depends also on the number of atoms in the most catalytically active sites: at the vertices or edges. For clusters of some metals (for example, platinum), the highest catalytic activity is achieved when atoms are located in high-coordinate sites at the faces, while high density of edges can create additional potential barrier to the reaction kinetics. In the case of catalysis using nanoparticles, the interaction of nanoparticles with the substrate material (far from being inert, in the general case) also plays a considerable role. By selecting the substrate, it is possible to enhance the interaction of atoms with it, to control the cluster thermal stability and to raise the cluster melting point.

Despite the studies on nanocatalysis that are in progress,[18–23] the chemical nanomechanics of the atom-and-molecular transformations of catalyst precursors has not been ultimately elucidated as yet.

Two-dimensional systems suitable for the design of optoelectronic devices were manufactured by chemical vapour deposition (CVD) or metal epitaxy on substrates prepared beforehand. These systems are metal nanoclusters deposited and regularly spaced at cryogenic temperatures on oxide or graphene (G) substrates having relatively large surface area.

The most efficient CVD procedure for the manufacture of materials with a required geometry of graphene stacks composed of several monoatomic planes is the epitaxy of the carbon vapour phase obtained by thermal decomposition of ethylene on a substrate (usually, Ir, Pd, Ni, Ru or SiC). This procedure was used to synthesize heterostructured materials with special metal/graphene contact interfaces involving the (0001) planes of cobalt and ruthenium and the (111) planes of nickel, platinum, palladium and iridium.[24–26] It was found experimentally that moiré superlattices of the Ir/G heterostructure are most stable.[27]

It should be emphasized that isolated clusters represent an intermediate pre-phase form of matter organization as atomic-and-molecular precursor configurations with their structure and specific properties being determined by a minor volume and the effect of non-autonomous surface layer with a high density of dangling bonds. The clusters with comparable numbers of atoms on the surface and in the bulk tend to exhibit variable atomic coordinations. The classification of the structures being formed is conventional; in essence, it is virtual and is determined based on the most stable and long-lived ordered atomic configurations with coherence on the short-range order scale with no long-range order.

This review considers the results of simulation of the properties of transition metal clusters not only as separate objects[6–10] but also as components of new heterostructured nanomaterials. The synthesis of clusters is presented as a multistage process comprising nucleation, growth, coalescence and agglomeration, and structural changes corresponding to each stage are analyzed. The formation processes of specific cluster layered structures arising at the interfaces upon the contact of metal films and clusters with

graphene are discussed in detail. Graphene in layered materials is considered not only as the natural and optimal substrate but also as a reinforcing protective coating which stabilizes the functional characteristics of composites.

In order to understand how the nature of bonds and structure (relationship between the short- and long-range order) affect the cluster thermal evolution and stability, silicon clusters with a covalent type of bonding are considered apart from the transition metal clusters.[11] The stability of silicene, a 2D silicon crystal, and its clusters in which the planar sp^2 bonds are unstable, similarly to these bonds in the fullerene-like carbon nanoclusters, is briefly analyzed. These structures can be stabilized by being placed on specially selected metal substrates [for example, Ag(111)]. Silicene, like graphene, exhibits chemical, protective and reinforcing properties and also possesses unique electronic characteristics.

II. Nanoclusters. Size effects

The properties of nanoparticles depend on their chemical composition, size, crystal structure defectiveness, morphology and other factors.[8–10,27] The packing density of atoms in the structure can be measured by the packing factor (n) — the ratio of the volume of atoms to the volume of a polyhedral cluster built of these atoms.

Structure †	Ih	fcc	hcp	bcc	pc	sph
n	0.78	0.74	0.74	0.68	0.52	0.34

Nanoclusters are characterized by the general notion 'isolated nanoparticle,' which is quite arbitrary, because it is almost impossible to obtain a nanoparticle that would not interact with the environment or with the neighbouring particles.

The addition of subsequent shells gives rise to cluster series. The fullest classification of one- and two-element clusters is presented in the Cambridge Cluster Database comprising, in particular, Cini, Mackay, Dzugutov, Marx, Bergman and other cluster series.[28–42]

In experiment, it is difficult to point out nanoparticles that do not interact with the environment;[35–38] as a rule, they interact with the material of measuring instruments.[39] When the size of objects is in the nano-range, the percentage of specifically coordinated and interacting surface atoms substantially increases as compared with atoms in the bulk. Therefore, it should be emphasized that physicochemical properties of nanoparticles depend rather on their size and surface morphology but not on the nature of atoms, molecules and the packing type and perfection. If the scale of some observed physical phenomenon is commensurable with at least one of the three particle dimensions in the nano-range, then, in accordance with the quantum theory,[10,39] quantum size effects should be considered in the description of this phenomenon. Depending on the number of these dimensions (D) in the nano-limit, nanosystems are classified into zero- ($D = 0$), one- ($D = 1$) and two-dimensional ($D = 2$); examples are quantum dots, nanowires and quantum wells.

† Structure designations: Ih is icosahedral, fcc is face-centred cubic, hcp is hexagonal close-packed, bcc is body-centred cubic, pc is primitive cubic; sph is sphalerite type.

The geometric regularities of filling by atoms of concentric shells j spaced by the distance r_{ij} from the central ith atom have been ascertained.[43,44] The number of atoms in the jth shell (N_j) is determined by the formula

$$N_j = a_j j^2 + b_j j + c_j \quad (1)$$

where the factors a_j, b_j and c_j vary over a finite range together with the number of shell j. For a cluster with a simple fcc structure

$$N_j = 4j^2 + 2 \; (j > 0)$$

while in the case of bcc structure

$$N_j = 6j^2 + 2$$

In the general case, for clusters with regular filling and with the coordination number Z, the number of atoms in the ith shell obeys the rule

$$N_j = (Z - 2)j^2 + 2$$

If the atom radius R is known, the number of atoms forming the cluster (N_Σ) can be estimated from the cluster size (L) using the relation

$$N_\Sigma = \left(\frac{L}{2R}\right)^3$$

Metal clusters of size from 0.5 to 5 nm comprise about a thousand atoms.

For clusters with cubooctahedral and icosahedral coordinations, N_j is determined by formula (1) and N_Σ can be found as follows:

$$N_\Sigma = \frac{1}{3}(10m^3 + 15m^2 + 11m + 3)$$

where m is the number of coordination shells. For these clusters, N_Σ = 13, 55, 147, 309, 561... In the case of hcp clusters, N_Σ = 13, 57, 153, 321, 581... In the Ih clusters of >10 nm size, an increase in the number of atoms leads to an increase in the deformation stress energy due to the mismatch of the topology of packing in the Euclidean space (the angular defect of packing is 0.02 rad.); simultaneously, the stability and competitiveness of the Ih structure decrease (*i.e.*, the decrease in the surface energy does not make up for the growth of elastic deformation energy).

Based on primary coordinations with allowance for the specific character of bonds, elementary groups are distinguished as well as 'secondary' superclusters that dictate the subsequent chain of more large-scale structuring including the symbiosis of aperiodic and periodic structures upon their coherent connection into hybrid systems — 'centaurs'.[41] This symbiosis does not rule out the synthesis of clusters with similar topology combined through the interaction of polytetrahedral structures (for example, Bergman polyhedra, 'quadrangular stars').[40,41] The polyhedral clusters arouse enhanced interest of the crystal chemists and materials scientists, because they provide the base for coherently structured ordering not only in nano- and quasi-crystalline but also in amorphous ultradisperse and liquid phases. An important issue for structural chemistry is

analysis of the properties of polyhedral multilayer clusters. These clusters can be regarded as not only independent nanoparticles but also as short-range order structural units that serve to form long-range order connections in complex phases combining different types of symmetry.

To date, efficient algorithms for the analysis of intermetallic compounds determining the specific geometry of the interatomic bond networks rather than the successive hierarchy of clusters have been developed.[42–46] For example, the structure of the $TbNi_2$ intermetallic formed by two-layer 63-atom clusters of the same type can be described in conformity with the hierarchical structure of the shells in the following way: 1@12@50 or 1Ni@6(Ni + Tb)@(36Ni + 14Tb). The number of atomic contacts (bonds) of each cluster with its neighbours is 12. Nanoclusters of this type are often encountered in other intermetallic compounds, for example, in Laves phases ($MgCu_2$, $MgZn_2$ and $MgNi_2$).[47] When analyzing the structure of materials in the nano-range, the regularities of their assembly should be taken into account apart from the dimensionality of structural units.[45,46]

Systematization of unusual structural types of ordering markedly extended the base of polyhedral close packings of spheres upon introduction of a substructure of wedge distortions, on the scale of the short-range order, as disclination networks that coherently make up for the angular defects of regular polytetrahedral packings. A possible alternative to the disclination networks is systematization of the coherent naturally forming polytetrahedral configurations using computer simulation involving specifically parametrized potential functions for the description of interatomic interactions.[32,42] For enhancement of interatomic correlations on the short-range scale, the following potential was proposed:[32]

$$r_{ij} \leqslant \sqrt{2}\, r_0$$

where r_0 is a value close to the statistically average interatomic distance in the system being considered. As a result, not only regular polytetrahedral configurations were distinguished on this scale and their symmetry was described, but also the statistical geometric analysis of their coupling (coherent cross-linking) in the structure was performed. The structural properties, the energy and the character of interatomic bonds have been studied in most detail for highly symmetric clusters with <100 atoms. As primary building blocks, these clusters with optimized structure determine also the stability of larger functional clusters (of 5–10 nm size).

Single clusters are prepared by the following key methods:

— chemical thermal decomposition of metal salts,[6] organometallic synthesis from a solution with stabilizing ligands;[48]

— mechanochemical synthesis by long-term (up to 300 h) grinding in ball and planetary mills of powders of pure metals or refractory compounds — metal borides, carbides and nitrides (*e.g.*, 7–10 nm $Ti_{44}C_{56}$ nanoclusters are prepared by mechanochemical activation over a period of $\sim$150 h);[49]

— electric explosion and detonation synthesis.[4]

The regular close-packed clusters of pure metals (for example, Au_{55}, Ni_{147}, Pt_{309} and Pd_{561}) are highly reactive; upon the reactions, they form new structures. For stabilization, shells, most often of organic ligands (L), are arranged around the surface of such clusters.[3,4] For example, 1.4 nm gold clusters were stabilized in two stages with triphenylphosphine, $[Au_{55}(PPh_3)_{12}C_{16}]$, while platinum and palladium clusters were stabilized by phenanthroline (1,10-phen), $[Pt_{309}(1,10\text{-phen})_{36}O_{30}$ and $Pd_{561}(1,10\text{-phen})_{36}O_{200}]$.[6] Transition metal clusters can be stabilized using various micellar groups, the sizes of their cavities determining the cluster size. For example, using toluene and surfactants, the 'chemical' stabilization of a cobalt cluster of 3 nm diameter was carried out.[50]

The stability of a nanocluster also depends on the character of interaction of valence electrons of the constituent atoms. The averaged 'molecular potential' of a nanocluster determines the configuration of the electron orbitals corresponding to the energy minimum for the filled levels. For clusters consisting of a few atoms, the $2p^6$, $1f^{11}$, $2s^2$; $1d^{10}$, $1p^6$ and $1s^2$ levels were found by solving the Schrödinger equation within the jelly model (Fig. 1).[5] A stable atomic structure with completely filled regular electron shells and minimum energy ensures the cluster stability. The numbers of atoms in clusters with atomic structures corresponding to the condition of filling of electron shells form the electronic magic series. The stability of small (up to 3 nm) clusters is rather determined by the energy balance of the electronic structure and that of larger clusters is dictated by the energy balance of the atomic structure.

Poole and Owens[39] followed the dependence of the properties of Al_{12}, Al_{13}, Al_{19}, Al_{20}, Al_{23} and Al_{24} nanoclusters on the electronic magic numbers while analyzing their reactivity towards oxygen. The clusters of this series are reactive (exceptions being almost inert Al_{13} and Al_{23}). The cluster reactivity depends not only on the number but also on the structure of atoms. This was clearly demonstrated in a study of gold clusters, which had an Ih structure in the 3–5 nm range of size (the bulk crystals have a fcc structure).[3]

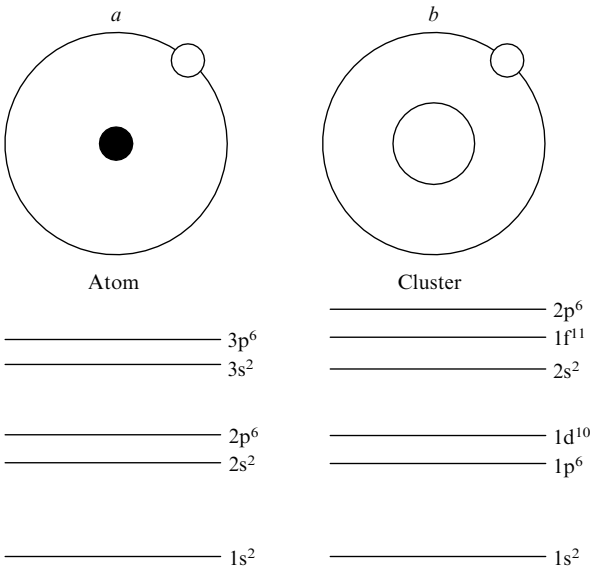


Figure 1. Energy levels of argon atom (*a*) and few-atom cluster (*b*) in the jelly model.[5]

As the metal particle size moves to the nano-range, the interatomic distances and lattice parameters change. It was found by electron diffraction that a decrease in the aluminium nanoparticle size from 20 to 6 nm brings about a 1.5% decrease in the lattice constant;[51] in the case of silver and gold nanoparticles, the decrease in the lattice constant is 0.1% as the nanoparticle size decreases from 40 to 10 nm.[49] However, for some nanoparticles, the opposite situation is observed: the lattice constant increases following decrease in the particle size (an example is CeO_2),[49] and for some metals (in particular, for Bi and Pb), no change in the lattice parameters was noted upon increase in the particle diameter from 5 to 8 nm.[52]

As the lattice constant of clusters decreases, the effect of dangling bonds of the atoms of outer shells becomes more pronounced and interatomic distances shorten, which brings about shear stresses and their relaxation in the near-surface layers. The atom density gradient thus arising may be of oscillating character and the oscillation period may differ from the period of the Friedel oscillations of the electron density. Charge density splitting gives rise to an electric double layer and the cluster surface becomes charged. Stress relaxation with allowance for the overall size effect can influence in different ways some characteristics such as density (cluster volume), phonon spectra, thermal expansion, heat capacity and so on. Frequency redistribution in the photon spectrum in the nano-limit is related to the appearance, in the low-frequency region, of a threshold frequency ($\omega_{\min}$) and waves with wavelengths not exceeding twice the particle size (d)

$$\omega_{\min} \approx \frac{c}{2d}$$

where c is the speed of sound. This implies one more size effect: as the particle diameter decreases and the particle morphology changes, the phonon spectrum shifts to higher frequency, which, in turn, dictates the size dependence of heat capacity and the general pattern of its temperature dependence.

The optical properties of nanodisperse materials ($<10-15$ nm particle size) also acquire some specific features: for example, grained films and colloid solutions become intensely coloured. Bulk metals tend to exhibit broad-band optical absorption by conduction electrons, while the absorption spectra of the finely dispersed Ag, Cu, Mg, In, Li and Na phases show peaks in the visible region but on going to the IR region, sharp decline in the absorption instead of growth is observed. Note that in the case of grained gold films (4 nm particles), the absorption maximum is in the range of 560–600 nm.[35]

The size effects manifested in the optical properties are related to the oscillating frequency dependence of the dielectric constant

$$\varepsilon(\omega) = \varepsilon_1(\omega) + \mathrm{i}\,\varepsilon_2(\omega)$$

caused by the discrete nature of the electron energy levels. In the nanorange, the imaginary component ε_2 is inversely proportional to the cluster radius R (in the general case, to the size of nanoparticles having any shape, not necessarily spherical)

$$\varepsilon_2^*(\omega) = \frac{\varepsilon_2(\omega)}{R},$$

where ε_2 is the imaginary component for a bulk (macro) system. However, due to the scatter of nanoparticle sizes and shapes, the oscillations are smoothed; nevertheless, the most significant differences from bulk samples are still retained for averaged values.

In semiconductors, the size effects are related to the fact that excitons, which represent weakly bound electron–hole pairs, have the crucial effect on the properties. Indeed, the high-frequency displacement of the band in the case of 10–12 nm CdSe nanoparticles[53] is accounted for by redistribution of the exciton excitation energies. As the molecular semiconductors diminish, the size effects, in particular, luminescence, start to be manifested if the scale of exciton excitations is comparable with the size of molecules.[54]

III. Simulation of the structure of transition metal nanoclusters

Computer simulation was applied to carry out numerous studies of the formation of transition metal nanoclusters (Al, Co, Cu, Ni, Ag, Au, Pd and Pt) in a vapour–gas medium and to perform detailed analysis of their internal structure and surface morphology.[55–67] One factor determining the nanocluster (crystallite) shape in the real cluster formation processes is the temperature dependence of the rate of coverage of faces by atoms. The temperature and kinetic energy ranges of these attached atoms (fragments) and the energy barriers they overcome determine not only the growth rate and details of attachment mechanism but also the structure formation regularities and deviations of the configurations of the formed clusters from regular configurations. The information about all factors affecting cluster growth and shape is presented for some substances as Nakaya diagrams.[9, 10]

The shape formation can be efficiently controlled by adding surfactants affecting the adsorption kinetics. While interpreting the mechanisms of nanocluster structuring during condensation and structural transformations on heating, it is necessary to take into account the thermodynamic instability of the generated states (isomerization), which is manifested as continuous variation of the predominating coordinations as a sign of structural instability. Copper, nickel and palladium clusters were studied by computer simulation most thoroughly.[61, 62, 64]

In the computer model database,[65–70] the interparticle interaction potentials calculated in different approximations differ in the complexity and in the accuracy of considering the many-body interactions. When choosing particular procedures for transition metal clusters, the specific features of these clusters should be taken into account, in particular, the presence of an open surface, structure regularity and interaction with the substrate.

In the present review, many-body potentials are analyzed for the interaction of transition metal atoms of isolated clusters and the clusters located on the substrate and contacting with other phases. In the analysis of binding energies (E) of atoms for transition metal clusters, preference is usually given to the estimation of many-body potentials according to Sutton–Chen potential versions[10]

$$E = \varepsilon\left[\frac{1}{2}\sum_i\sum_{j>i} V_0(r_{ij}) - C(\rho_i)^{1/2}\right]$$

where $V_o(r_{ij})$ is the contribution of the repulsion forces between atoms i and j spaced by distance r_{ij} to the bond energy; ρ_i is the electron density at the point of atom i; ε and C are fitting parameters to the results of quantum mechanical calculations or to experimental characteristics (*e.g.*, bulk elastic moduli).

The potential energy of nano-sized systems and palladium surface can also be estimated using the Cleri–Rosato potentials parametrized based on tight-binding calculations,[65]

$$E_{Cl} = \sum_i (E_b^{(i)} + E_r^{(i)})$$

$$E_b^{(i)} = \left\{ \sum_{j, r_{ij} < r_c} \xi^2 \exp\left[-\frac{q}{\alpha} \left(\frac{r_{ij}}{r_0} - 1 \right) \right] \right\}^{\alpha}$$

$$E_r^{(i)} = \sum_{j, r_{ij} < r_c} A \exp\left[-p \left(\frac{r_{ij}}{r_0} - 1 \right) \right]$$

$E_b^{(i)}$ is the band energy, $E_r^{(i)}$ is the repulsion energy (Born–Mayer), r_{ij} is the distance between atom i and the closest neighbouring atom j located in a sphere with the cutoff radius r_0; the values of ξ, q, α, A, p are determined by fitting to theoretical or experimental cohesive energy of lattice parameters of bulk samples, compressibility of the bulk metal, elastic modulus, *etc.*

Some other potentials are also used. The interactions of atoms of the fcc Ni_{561} nanoclusters with the substrate material (silica) can be calculated [10, 66] using the Lennard-Jones potential (by describing the Si—Ni and O—Ni atom–atom interactions by fitting parameters reported by Sato

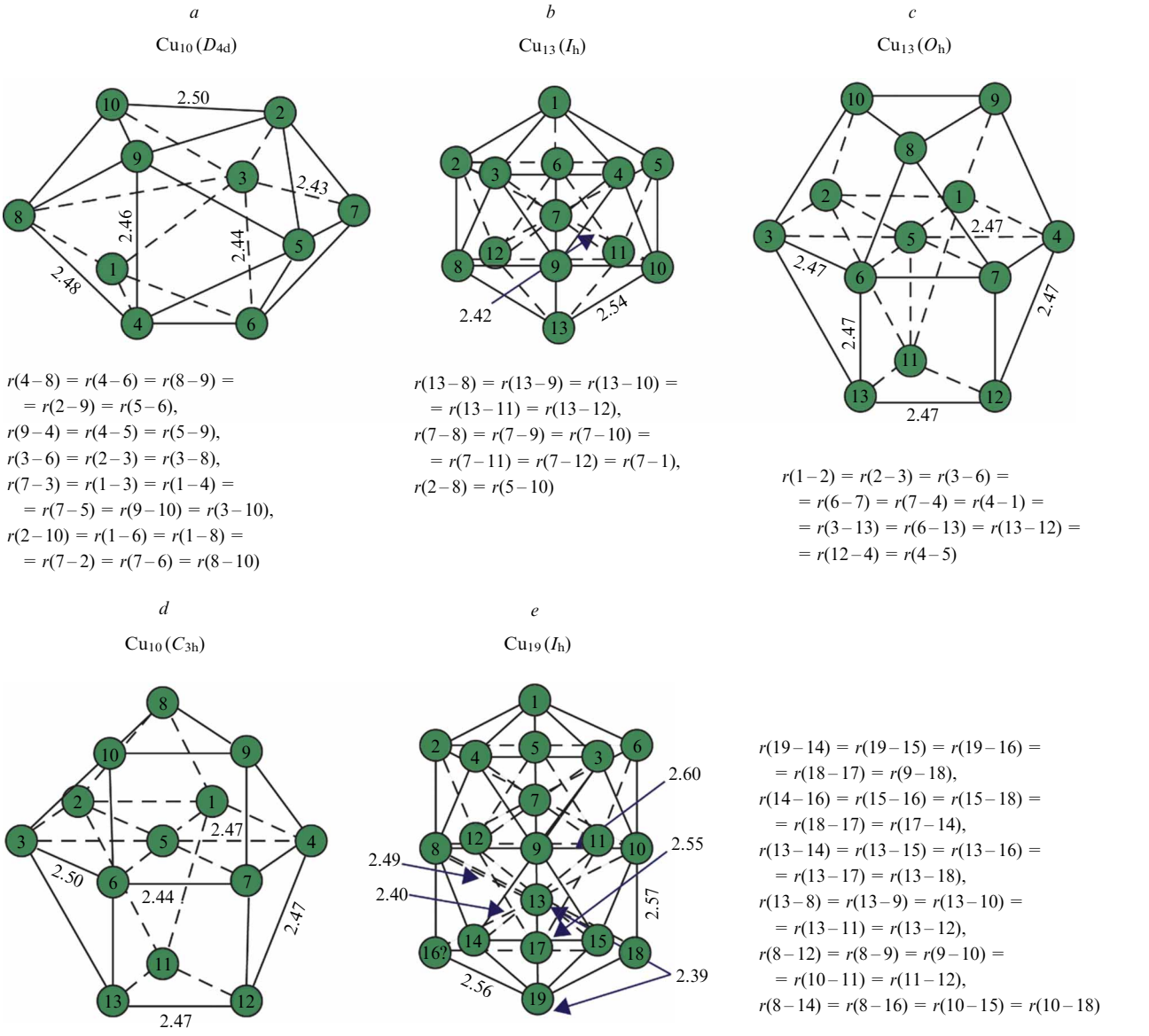


Figure 2. Examples of highly symmetrical close packings of atoms in copper clusters (the distances are in Åangströms).[33]
(*a*) Tetragonal antiprism, (*b*) icosahedron, (*c*) hexoctahedron, (*d*) trigonal bipyramid, (*e*) double icosahedron.[33]

et al.[66]); in the case of the Ih Pd_{561} cluster and graphene substrate, the Pd–C interaction was calculated using the Morse potential for binary systems parametrized using quantum chemical calculations,[10]

$$\Phi(r_{ij}) = \frac{q_i q_j}{r_{ij}} + D_{ij}\left\{\exp\left[\gamma_{ij}\left(1 - \frac{r_{ij}}{r_{ij}^{(0)}}\right)\right] - 2\exp\left[\frac{\gamma_{ij}}{2}\left(1 - \frac{r_{ij}}{r_{ij}^{(0)}}\right)\right]\right\}$$

where the first term describes the Coulomb interaction of charges q_i and q_j on Pd and C atoms; r_{ij} are the Pd–C interatomic distances; D_{ij}, γ_{ij} are fitting parameters to experimental values of the cohesive energy for the interface between graphene and palladium planes.

In the modelling of metal–carbon systems, various rules of combining exponential potentials such as the Morse potential are used to estimate the M–C interatomic interactions.[10]

Rusina *et al.*[33] performed the structure classification for energetically most stable highly symmetrical atom packings in copper clusters starting from dimers and up to 19-atom clusters in terms of the electron density functional theory (Fig. 2). Among the optimized 3D structures, most stable are the tetrahedron (Cu_4), bipyramid (Cu_5), regular octahedron (Cu_6), Archimedean antiprism (Cu_{10}), and icosahedra ($n \geqslant 12$). The data were obtained from the results of simulation in the low-temperature region taking into account only the dynamics of thermal vibrations.

For thermodynamic conditions corresponding to a temperature close to 0 K, MD simulation was carried out (the results are discussed below) not only for magic (N from 13 to 147) but also for other [68] clusters using potentials similar to the Sutton–Chen potential [embedded atom model (EAM)]. The dependences of the specific energies of silver and iron clusters on the number of atoms forming them are shown in Fig. 3, while Table 1 gives the estimates of energies for a number of most stable metal clusters relative to the energy of the locally stable liquid silver clusters with the same number of atoms. The cluster stability was estimated using statistical geometric analysis of tetrahedricity and octahedricity distribution of Delaunay simplices.[69] Each cluster was characterized by the standard deviation of the tetrahedricity and octahedricity and by the number of constructed simplices. A cluster was considered to be locally stable if the sum of standard deviations did not exceed 1/5 of this sum for a silver cluster taken as the reference. According to the comparison results, clusters with cuboctahedral coordinations typical of the fcc structure can be regarded as most stable, while the clusters with configurations typical of a bcc structure had defective many-particle shells and possessed no symmetric structure. For comparison, Table 1 presents the results of statistical geometric analysis for a fcc model of argon constructed based on the short-range Lennard-Jones (LJ) pair potential and reflecting a different nature of interatomic bonds. No significant differences from fcc metals were revealed, because both the packing density and the high contribution of the repulsion potential served as counterbalances for disordering processes for the argon model.

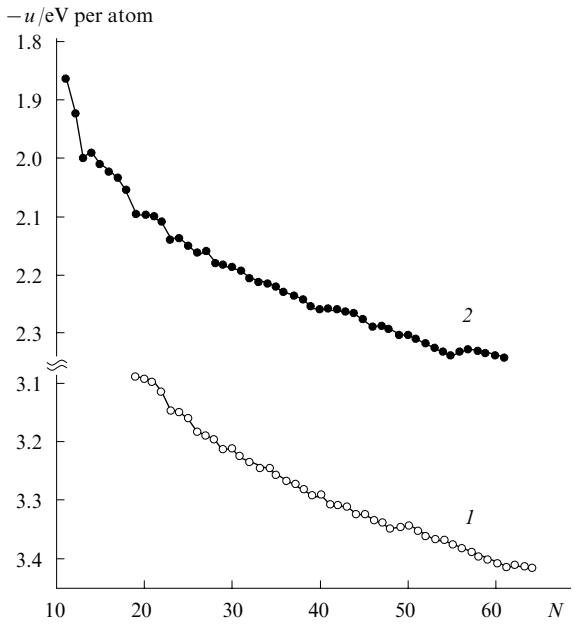


Figure 3. Specific energies ($u = U/N$) of iron (*1*) and silver (*2*) clusters *vs.* the number of atoms they contain (MD calculation with EAM potentials).[68]

For more profound study of the dynamics of atoms and nucleation processes, it is necessary to take into account the effect of the cooling rate and the final temperature on the physical parameters of nanoparticles. For this purpose, cooling of a vapour–gas Cu system with three different cooling rates, $V_{cool} = 0.05$, 0.025 and 0.005 K ps^{-1}, and two final temperatures $T = 373$ and 77 K was studied by the MD method.[71] These final temperatures were selected in view of the fact that not only inert gases but also liquid nitrogen and even usual water (boiling points of 77 and 373 K, respectively) are used as cooling agents in the facilities for the production of metal nanopowders.

From the standpoint of efficiency of planning of industrial processes, it is important to elucidate the degree to which the temperature factor, together with other factors, affects the size and structures of the nanoparticles formed. Within the framework of the statistical computer methods being developed [both classical (MD and MC)[8, 71, 72] and quantum methods like the Car–Parinello method[73]] using the multiple-processor computations of cluster series (LAMMHS[13]), it is possible to elucidate this effect on the real vapour–gas condensation processes. For this purpose, one should study virtual analogues of the elementary events of the atom and cluster kinetics such as the formation of primary atomic configurations (dimers, trimers and so on), their growth by atom-by-atom deposition and *via* mutual collisions and the subsequent coalescence and coagulation processes at specified thermodynamic and kinetic parameters.

The results of MD calculations of the structures and forms of copper nanoclusters condensed from the gas phase depending on the final temperature and cooling rates are presented in Table 2. Data for six computer experiments are given, which demonstrate that the rate of cooling of the gas mixture affects the number of the obtained particles for an invariable number (85 000) of atoms at the initial similation stage. When the cooling rate was decreased 10-fold, the number of the resulting particles decreased 2.7-fold at the final temperature of 77 K and 3.1-fold at the final temperature of 373 K. This correlation is quite reasonable as in the case of slow cooling, there is enough kinetic energy in the system for rather large particles to be formed during chaotic

Table 1. Most stable configurations of clusters of specified size and locally stable silver clusters.[68]

Parameter	N	fcc clusters					bcc clusters					
		Ag	Cu	Ni	A1	Ar(LJ)	Cs	Fe (Ref. 8)	Fe (Ref. 10)	K	Ta	Ag(liq.)
I	13	0.0	0.0	0.0	0.0	0.01	0.02	0.0	0.01	0.0	0.0	0.06
II		0.0	0.0	0.01	0.01	0.01	0.01	0.0	0.0	0.01	0.0	0.17
III		20	20	20	20	20	20	20	20	20	20	20
I	19	0.0	0.0	0.01	0.01	0.03	0.04	0.01	0.01	0.02	0.0	0.18
II		0.0	0.0	0.01	0.01	0.01	0.06	0.01	0.01	0.04	0.01	0.2
III		40	40	40	40	40	40	40	40	40	40	39
I	23	0.0	0.01	0.01	0.01	0.01	0.02	0.04	0.01	0.03	0.18	0.35
II		0.0	0.01	0.01	0.01	0.01	0.03	0.08	0.01	0.04	0.21	0.38
III		56	56	56	56	56	56	56	56	56	51	57
I	26	0.0	0.01	0.32	0.01	0.01	0.05	0.04	0.01	0.06	0.26	0.23
II		0.0	0.0	0.43	0.01	0.02	0.05	0.07	0.02	0.04	0.25	0.3
III		69	69	61	69	69	69	69	69	69	60	63
I	28	0.0	0.08	0.01	0.28	0.29	0.06	0.27	0.28	0.4	0.28	0.3
II		0.0	0.05	0.02	0.26	0.26	0.06	0.24	0.25	0.4	0.3	0.22
III		69	73	69	78	78	71	78	77	79	70	75
I	32	0.0	0.01	0.09	0.40	0.55	0.33	0.55	0.56	0.71	0.29	0.24
II		0.0	0.01	0.1	0.25	0.42	0.24	0.42	0.43	0.61	0.22	0.34
III		86	86	82	90	95	82	95	95	97	85	88
I	39	0.0	0.24	0.24	0.35	0.07	0.39	0.34	0.35	0.35	0.23	0.38
II		0.0	0.42	0.41	0.52	0.1	0.43	0.43	0.53	0.40	0.31	0.36
III		110	110	110	117	112	106	119	116	124	109	119
I	40	0.0	0.01	0.22	0.39	0.5	0.11	0.31	0.42	0.62	0.21	0.62
II		0.0	0.02	0.19	0.33	0.47	0.05	0.29	0.38	0.64	0.14	0.48
III		107	107	114	121	124	106	121	125	133	109	127
I	46	0.0	0.54	0.72	0.53	0.54	0.31	0.5	0.54	0.51	0.72	0.62
II		0.0	0.5	0.67	0.46	0.57	0.34	0.47	0.45	0.51	0.62	0.54
III		130	134	139	147	141	136	152	147	145	153	144
I	49	0.0	0.42	0.37	0.52	0.31	0.16	0.4	0.5	0.41	0.25	0.39
II		0.0	0.46	0.44	0.44	0.38	0.26	0.42	0.44	0.45	0.28	0.36
III		144	147	151	162	147	142	161	162	161	148	159
I	55	0.0	0.0	0.01	0.09	0.16	0.1	0.8	0.74	0.61	0.54	0.54
II		0.0	0.01	0.02	0.01	0.03	0.06	0.66	0.62	0.56	0.39	0.39
III		164	164	164	160	176	160	187	193	189	176	189
I	147	0.0	0.08	0.15	0.12	0.27	0.38	1.17	1.5	1.23	0.89	1.78
II		0.0	0.07	0.07	0.08	0.08	0.36	1.05	1.33	1.17	0.68	1.63
III		549	552	560	542	584	560	619	635	610	564	663

Note. Three numbers in each cell characterize the deviations of the tetrahedricity (parameter I) and octahedricity (parameter II) defined as the distances between the tetrahedricity and octahedricity vectors of the considered clusters and the reference silver clusters (for the latter, the values are zero); parameter III is the number of Delaunay simplices.

Table 2. Contents of various structures and forms of copper nanoclusters synthesized by gas phase deposition.[71, 74]

V_{cool} /K ps^{-1}	T/K	Number of clusters	Content of nanoclusters (%) with the structure				Content of nanoclusters (%) with the shape	
			fcc (hcp)	Ih	Dh [a]	amorphous	chain	spherical
0.05	77	46	22.02	45.83	20.87	11.28	76.08	23.92
0.025	77	35	22.51	41.93	30.02	5.54	74.28	25.72
0.005	77	17	23.59	26.82	49.59	0	58.83	41.17
0.05	373	19	22.57	31.38	46.05	0	89.47	10.53
0.025	373	13	29.43	30.07	40.5	0	84.61	15.39
0.005	373	6	38.33	26.67	35	0	83.34	16.66

[a] Designation of the decahedral structure.

motions and atom–cluster and cluster–cluster collisions. The statistical average time range for the nucleation of critical-size clusters from several tens of atoms with prospects for further growth was estimated at 30–60 ns.[13,58] In computer experiments, the size of these particles was attained upon combination of nuclei of even 10 nm size. In this case, further growth can be implemented through the subsequent coalescence of tens of smaller clusters.

For the change in thermodynamic conditions, it is necessary to take into account the appearance of a faceted structure of the cluster surface, which determines the course of coalescence and coagulation processes. The variation of the nanoparticle structure as a function of the cooling rate was consistently analyzed.[71,74] As expected, transition to close-packed structures took place irrespective of the final cooling temperatures. However, detailed analysis demonstrated that at high final temperature, the content of Dh clusters decreased with a decrease in the cooling rate compared with their content at 77 K. This is related to the fact that the Dh structure was intermediate between the icosahedral and close-packed fcc and hcp structures under conditions where there was enough kinetic energy initiating internal rearrangements in the system.[74]

It follows from the data of Table 2 that the most favourable conditions for the formation of clusters with close-packed fcc or hcp structures appeared in the system with a cooling rate of 0.005 K ps^{-1} and a final cooling temperature of 373 K. The calculated Cu–Cu bond energies for these regular packings (with interatomic distances of 0.235–0.270 nm) are limited to the range of 2.5–2.8 eV per atom; the bond energies for larger and more stable clusters with a regular structure were 3.15–3.25 eV per atom in the low-temperature region (200–400 K).

Of interest are the ratios of the structures and shapes of nanoclusters formed by different mechanisms in systems with different final temperatures. A comparative analysis of structures obtained at 77 and 373 K showed the predominance of close packings (fcc, hcp, Dh) in a system with the final temperature of 373 K; no amorphous particles were present. This is associated, first of all, with the fact that the energy of clusters is sufficient for optimizing their internal structure under conditions of free motion in the specified volume of the model space over a rather short period of time ($\sim$20 nm). The particles obtained under these conditions represent a sort of aggregates made of a large number of smaller particles stuck together and they have rather large surface area. It was shown that spherical clusters are formed, most often, when the cooling fluid temperature is about 77 K; they consist of icosahedral and decahedral particles aggregated without forming a common coherent structure or specific faceting of a common polytetrahedral cluster.

Clusters with predominantly fcc and hcp structures are, most often, worm-shaped. The vast majority of clusters having this shape are agglomerates consisting of several tens of smaller clusters that agglomerated during free motion in the system at temperatures close to the temperature of cooling gas or vapour being fed to the reactor. In this case, the kinetic energy is insufficient for fusing together the primary nanoparticles; therefore, the clusters mainly stick together (most often, through interatomic interaction forces) without the formation of coherent boundaries. The particles obtained under these conditions are large, the largest one containing 37 140 atoms and having resulted from collision and sticking together of more than 20 smaller clusters. Particles of this type tend to have a rather great surface area, which is necessary for catalytic applications where the contact area with other reaction components is crucial for catalyst efficiency.[75,76]

The most favourable conditions for the synthesis of Ih nanoparticles were created by the cooling rate of 0.05 K ps^{-1} down to 77 K final temperature. Under these conditions, about half of the particles formed had the Ih structure and comprised not more than 1000 atoms. Particularly, such copper clusters are demanded for the manufacture of ductile steel.

During the gas phase synthesis, the clusters can be formed according to two key scenarios:

— a cluster is formed without relaxation (or with incomplete relaxation), which is observed when inert gases (in particular, argon) are employed to cool the vapour–gas mixture; in this case, a shell structure according to the multifractal diplo type is formed on rapidly rotating and colliding clusters (Fig. 4);[74,77,78]

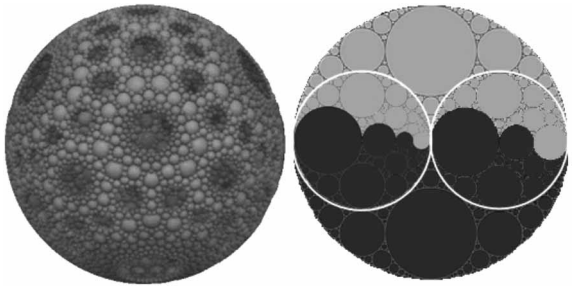


Figure 4. Surface (*a*) and equatorial cross-section (*b*) morphology of multifractal diplo clusters.[74]

— the formation process of a large cluster comprises all of the stages with relaxation: nucleation, condensation, growth of single clusters, cluster collisions and coalescence (Fig. 5).[74,79]

The relaxation of the model system activated by the stored energy of clusters and coordination restructuring of diplos resulted in the formation of coherent boundaries within the cluster. During each relaxation step, a coherent structure formed as a result of thermally activated diffusion rearrangements. Thus, instead of disordering boundaries, in the multifractal diplo structures, coherent couplings of fragments with topologically compatible coordinations were obtained throughout the whole cluster.

In the case of formation of competing structuring centres with comparable surface energies and chemical potentials, the cluster was split into two particles, an interface appeared and two independent shells of the separating clusters formed.

As can be seen in Fig. 5, the cluster formation (bottom-up along the time scale)[13,74,79,80] in the metastable gas phase started with homogeneous nucleation.[13,62,64] After completion of this process, different mechanisms of the subsequent growth are possible, the most important of these being agglomeration and coalescence.[14,71,80] The cluster agglomeration includes the stage of accretion virtually without change in the shape. Upon coalescence, the

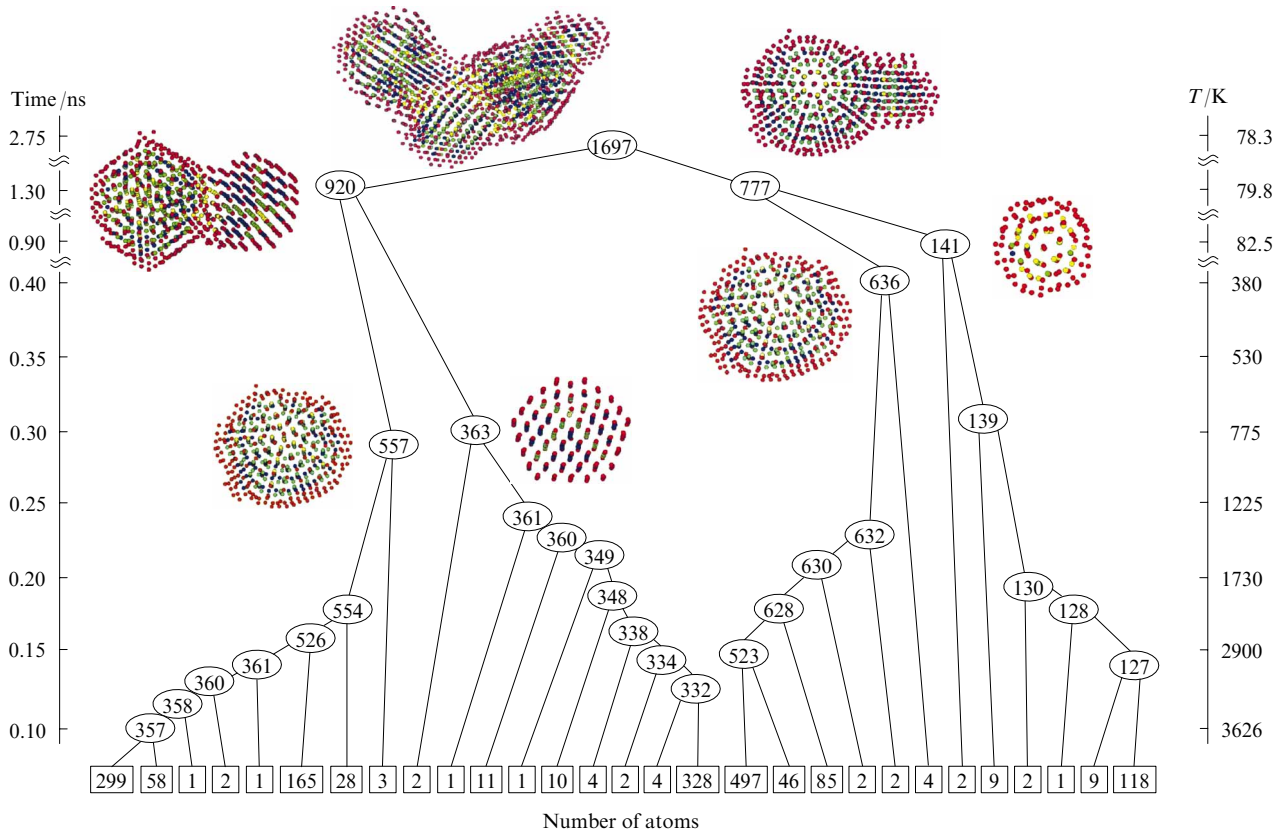


Figure 5. Illustration of the cluster condensation process lasting for 2.75 ns and including nucleation, condensation of single clusters and cluster coalescence upon collision to give a 1697-atom integral cluster.[74]

clusters are fused to one another to give a single particle with a shape differing from the shapes of the primary clusters before the collision. Under certain thermodynamic conditions, a coherent cluster structure is formed (all atoms both in the bulk and on the surface are considered). The results are in good agreement with the data of computer investigations of the condensation of nickel nanoparticles,[15,80] which demonstrated that coalescence plays an important role at early stages of the synthesis, that is, when the temperature in the system is high. In the case of intense cooling with an inert gas, the temperature rapidly decreases, and agglomeration giving multifractal diplo structures (see above) becomes the predominant growth mechanism. When such processes considerably predominated, the synthesized particles acquired various shapes and their coordination segments were composed of different crystalline structures.

IV. Thermal stability and size effects during heating of isolated clusters: isomerization, order–disorder transition, hysteresis

An important issue for the design of functional nanoclusters is the research into the mechanisms of stabilization of nanodispersed state. First of all, this concerns the thermal stability of isolated clusters and maintenance of the multilevel 2D system they form upon attachment to the substrate. Other problems include the initial formation of a geometrically perfect internal atomic packing and surfaces of single nano-sized (~2 nm) clusters followed by their precise spacing during positioning on the substrate. The optimal number of transition metal atoms in nanoclusters does not exceed a thousand. The thermal evolution of nanoclusters of exactly this size was studied by the MD technique.[17,61–67,71,72]

Analysis of the results of MD simulation of heating of fcc nickel, copper and palladium clusters with size variation and the data obtained for other metals, in particular, for gold and silver,[8,12] revealed specific thermal size effects manifested as atomic packing rearrangements and a decrease in the structure stability. The researchers established the influence of the initial structure characteristics of the nanoclusters, heating modes and kinetic factors during thermally activated development of diffusion on the nanostructuring processes — thermal evolution of clusters comprising isomerization, quasi-melting‡ and decay of the regular structure classified as an analogue of the order–disorder phase transition in bulk systems.

IV.1. Isomerization

According to MD results,[71,72,74,80] melting of nickel, palladium and gold clusters, unlike melting of macroscopic solids, is extended over a considerable temperature range, which is matched by quasi-melting in the solid-like state. On

‡ The terms 'isomerization' and 'quasi-melting' were introduced in 1989 by nanoscience classics R S Berry and D J Wales,[31] who analyzed unusual states of clusters.

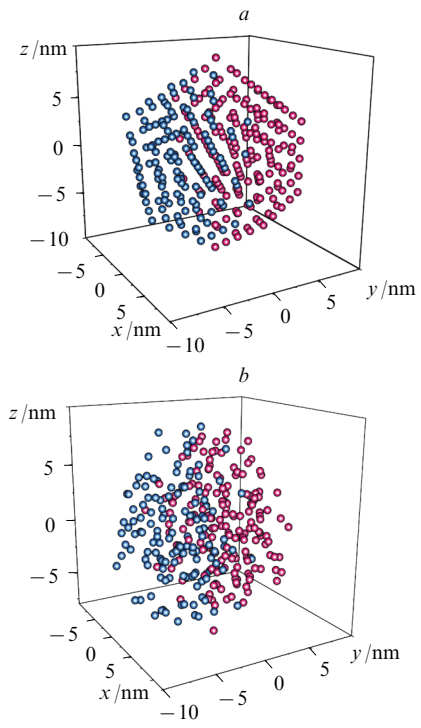


Figure 6. Ni_{561} nanoclusters with initial Ih structure at 300 (*a*) and 1500 K (*b*).[9,81]

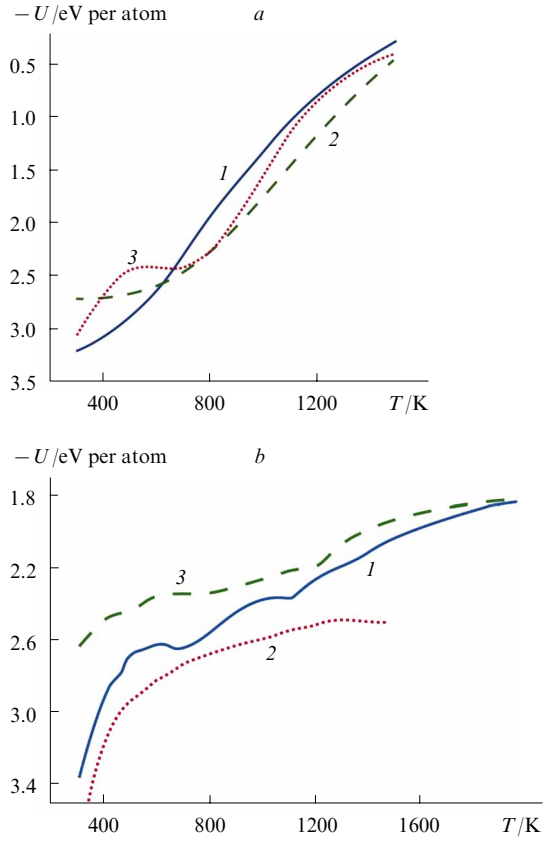


Figure 7. Temperature dependences of the potential energy of nickel nanoclusters with different initial structures.[83]
(*a*): Ni_{561} cluster with initial structures: fcc (*1*), bcc (*2*), Ih (*3*); (*b*): heating of isolated Ni_{309} fcc clusters (*1*), Ni_{561} Ih clusters (*2*), glass transition of the Ni_{309} melt (*3*).

heating, the Ih clusters of the above-listed metals (for example, nickel) comprising < 1000 atoms proved to be energetically more stable (Fig. 6). The potential energy changes corresponded to the kinetics of structural interconversions (Fig. 7).

While the solid-like state of the cluster was maintained, its structure changed considerably following temperature rise and enhancement of the diffusion motion (*e.g.*, transient hybrid forms appeared as a result of heterogeneous accretion of structures of different types). The quasi-melting stage was preceded by structural rearrangements, which were regarded as thermal nanosize effects. These rearrangements, classified as isomerization, preceded the proper melting, the initial stage of which was the appearance of adatoms and vacancies.[81–84]

Polukhin *et al.*[64,67] employed MD simulation of the thermal evolution of perfect Ni_N and Pd_N nanoclusters comprising 13 to 561 atoms and having different initial structures (fcc, bcc or Ih) upon stepwise heating (50 K steps) from 300 to 1350 K.

In the simulation of heating of fcc nickel and palladium nanoclusters, specific thermal size effects were identified, caused by change in the atomic packing and a loss of structure stability initiated by cuboctahedral to icosahedral packing transformation. By analogy with macroscopic solids, melting of clusters with a perfect polyhedral structure started from the surface; it was initiated by displacements of atoms located at the vertices and edges followed by displacements of atoms located on adjacent faces and in the outer shell, while atoms of the inner shells (centre) were rigidly fixed at their sites.

The specific thermal size effects manifested as atomic packing rearrangements and deterioration of the structure stability induced by development of the diffusion mobility and cuboctahedral to icosahedral packing transformation were also detected in the case of relaxation annealing of copper clusters (Fig. 8). This mechanism of diffusion in nanoclusters is related to the absence of vacancies, dislocations and disclinations and developed grain boundary surface inherent in real polycrystalline metals.[85]

The temperature variation of the potential energy of clusters during heating to complete melting and subsequent cooling gives rise to caloric hysteresis loops, the characteristic features of which are determined by the cluster size and the direction of temperature change (heating or cooling) (Fig. 9). For example, in the case of the Au_{135} cluster, the transformation of the fcc structure into the Ih structure occurred during heating at 395–405 K, while during cooling, the structure instability region was manifested as sharp energy changes at higher temperatures (in the 520–530 K range).[63] The transformations were manifested most clearly as the shift to higher temperature of kinks and peaks corresponding to isomerization. In the case of the Cu_{201} cluster, this thermal size effect is manifested as a sharp decrease in the energy (actually, a kink) in the 750 –755 K range and as resolution of an additional structure as a prepeak (see Fig. 9 *b*).[71,80] Heating of the Ni_{1697} cluster (see Fig. 9 *c*) resulted in a partial replacement of the hybrid structure (fcc + Dh + Ih) by mainly polytetrahedral packings (Ino + Dh + Ih). This process is reflected by a kink in the

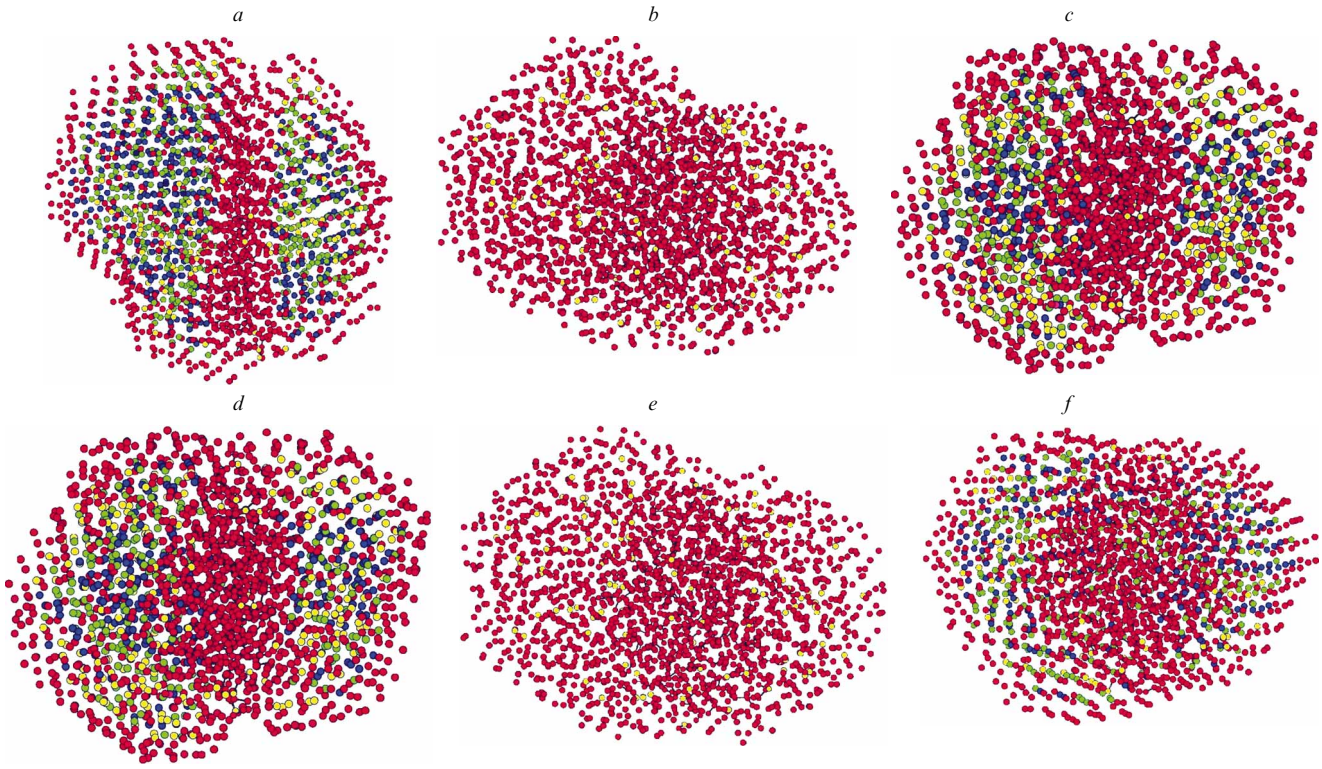


Figure 8. Melting and crystallization dynamics of the Cu_{2119} cluster at 400 (*a*), 800 (*b*), 1500 (*c*), 1200 (*d*), 800 (*e*) and 400 K (*f*).[74, 84]

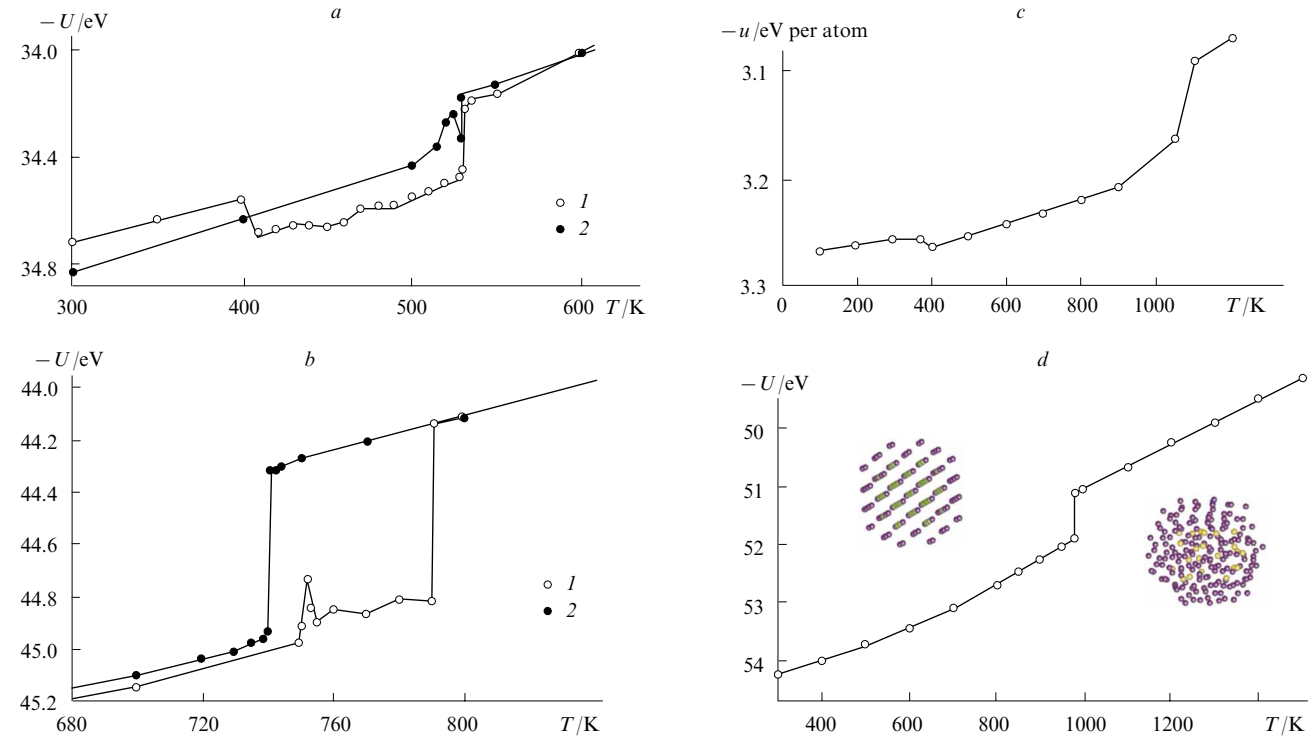


Figure 9. Temperature dependences of the potential energy during melting (*1*) and crystallization (*2*) for Au_{135} (*a*),[71, 79] Cu_{201} (*b*) and Ni_{1697} (*c*) and illustration of the disorder of the initial Ni_{201} fcc structure (*d*).[74, 80]

temperature dependence of the potential energy in the range of 380–400 K and an energy decrease, while during heating from 850 to 1080 K it is responsible for replacement of the smooth increase in energy to 850 K by a sharp rise. For the Ni_{201} cluster, the kink is located in the range of ~980 K (Fig. 9 *d*). These changes can be treated as being due to the destruction of the shell structure of the cluster; they are manifested as shifts of the kinks and peaks corresponding to isomerization to higher temperatures. The simulation of the thermal evolution of nickel clusters demonstrated higher stability of the fcc structure and a noticeable increase in its stability upon increase in the cluster size. Transitions from the fcc to Ih packing took place at 285 K (Ni_{135}) and at 352 K (Ni_{177}), *i.e.*, the stability of the fcc structure increased with increase in the cluster size.[86]

The thermal size effects are also manifested in the temperature dependences of other characteristics, for example, the internal pressure and internal stress (Figs 10 and 11) over a broad temperature range even when liquid- and solid-like states coexist (during quasi-melting). The non-monotonic temperature dependence of the internal pressure reflects complex structure transformations and modification of the cluster state on heating.

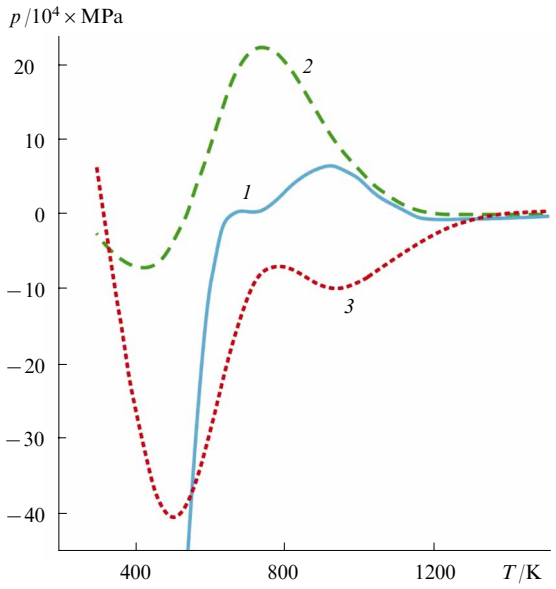


Figure 10. Temperature dependences of the internal pressure (p) for the Ni_{309} clusters with the fcc (*1*), bcc (*2*) and Ih (*3*) structures.[83]

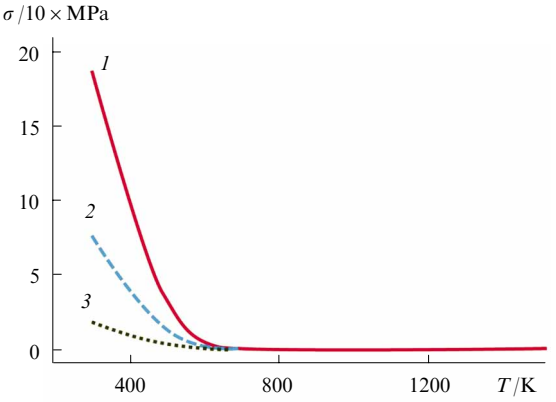


Figure 11. Temperature dependences of the internal stress (σ) for fcc (*1*), bcc (*2*) and Ih (*3*) clusters.[83]

IV.2. Specific details of the order–disorder transition

Specific thermal size effects are caused by an increase in the atom diffusion velocity. The diffusion in nanoclusters during heating is initiated by intensification of surface atom displacements and the appearance of pair structure defects — vertex atoms displaced on the surface (classified as adatoms) and vacancies that drift in the surface shell along the edges.

An increase in the fraction of surface atoms affects the specific details of the diffusion mobility mechanisms determined by the cluster surface morphology. Upon heating, the kinetic energy (activation energy) of the near-surface layer atoms becomes sufficient to transform a part of the surface atoms to adatoms; this transformation is the initial phase of diffusion. Further development of the diffusion is determined by switching-on of the mechanism of interchange of edge atoms and subsequently (as heating is continued) also face atoms. When heating is terminated, the vacancy drift may end in vacancy deformation between two coordination sites (vacancy splitting) but as the diffusion process propagates deep into the cluster, the stability of vacancies increases. The subsequent increase in the number of adatoms due to departure of atoms from the cluster surface shell may occur if heat is supplied or upon pronounced kinetic energy fluctuations.

The transition of cluster shells into the fluid state with the disappearance of faceted and then shell structure completes the melting phase transition analogue. The possibility of non-stationary states such as isomerization and quasi-melting for nanosystems does not contradict experimental data.[3,85–90] During heating, the energy of atoms increased to a level sufficient for optimization of the whole structure. With the solid-like state being maintained, the cluster structure experienced strong coordination fluctuations during heating accompanied by the formation of transient hybrid forms (see Figs 8, 12), which were defined as thermal nanosize effects preceding the proper melting process. For example, for the Cu_{1697} cluster, the structure transition (analogue of melting) was completed at 1200 K by the final stage of quasi-melting involving successive transition of all shells into the fluid state.[87] The completion marked the structure branching point: further heating induced development of the melting process with 'structure homogenization' of the melt, while cooling led to probable restoration of the initial state (depending on the cooling rate).

Simulation of the heating of copper clusters revealed a characteristic hysteresis region (Fig. 13) confined by two temperatures, which were called, by analogy with bulk systems, melting and crystallization points. For nanoclusters of the metals considered here, these temperatures were markedly different, although the regions of coexistence of fluid and solid-like states were present. The temperature hysteresis region markedly changed with the change in the number of atoms in nanoparticles: as the cluster size increased, the region narrowed down, while the potential energy increased according to a steeper pattern resembling the pattern of caloric curves for bulk systems.[71]

It was noted above that perfect clusters contain no adsorbed or own adatoms, which are always present on the surface of bulk crystals at ambient temperatures; they

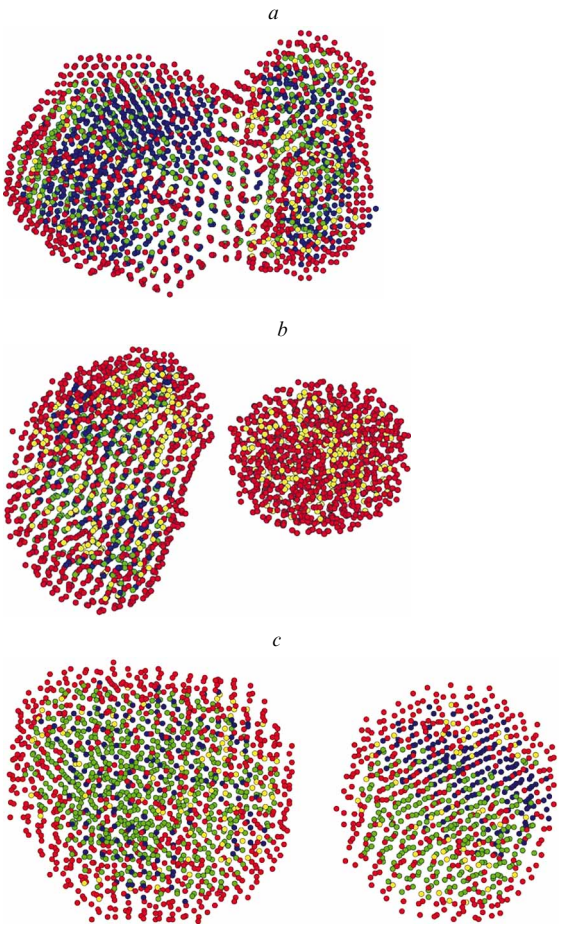


Figure 12. Thermal evolution of the copper nanocluster heated from 400 (*a*) to 800 K (*b*) and relaxing for 20 ns (*c*).[74]

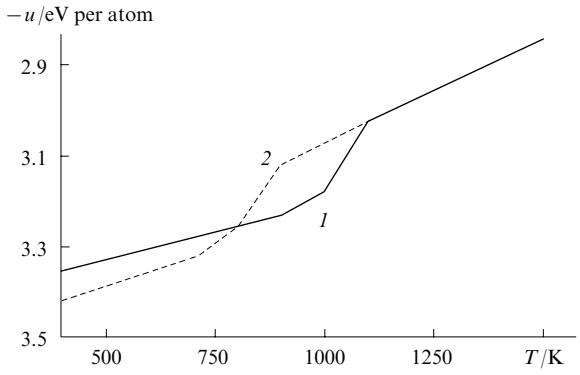


Figure 13. Temperature dependences of the specific potential energy during melting (*1*) and crystallization (*2*) of the Cu_{2119} cluster.[74]

determine the mechanisms of development of surface diffusion, which destabilizes the structure of the adjacent shells. To switch-on these mechanisms in a morphologically perfect cluster, it is necessary to create thermal conditions under which some of the near-surface atoms can be transformed into adatoms capable of migration over the cluster surface. In other words, a certain activation energy (E_a) is required to convert a surface-coordinated atom to an adatom. The atoms located at the vertices and edges of the cluster in the quantity N_0 are most susceptible to this thermally activated transformation. With the assumption that heating the cluster to temperature T would produce N_a of such atoms, the activation mechanism can be described by the exponent

$$N_a = N_0 \exp\left(-\frac{E_a}{k_B T}\right)$$

The atoms at the edges and vertices that migrate from their initial equilibrium positions form primary vacancies (pop-in defects) and adatoms (pop-out defects) of, for example, the sixth additionally arising shell of M_{561} clusters.[9]

The thermal size effects are manifested in both a substantial decrease in the cluster melting points, as can be seen from caloric curves, and the pattern of the temperature dependence of the kinetic diffusion coefficients[§] and shear viscosity. Thus the full diffusion coefficient (D) for the Ni_{561} cluster comprises considerably different components — radial $D_r(T)$ and tangential $D_\tau(T)$ components — with the activation energy variation at 650 K: from 0.41 to 0.28 eV for E_r and from 0.19 to 0.15 eV for E_τ .

From the time dependence of the root-mean-square displacement of atoms at 1500 K calculated for nickel clusters, the following diffusion coefficients were found:[9]

Cluster	Ni_{309}	Ni_{309}	Ni_{309}	Ni_{561}
Structure	fcc	bcc	Ih	Ih
$D/10^{-6}\times$ cm^2 s^{-1}	5.3	5.1	6.3	4.9

The substantial increase in the ratio of the root-mean-square diffusion displacement of an atom to the average interatomic distance with a decrease in the nanocluster size is also manifested as a thermal size effect. As compared with the 13% Lindemann criterion for macroscopic systems, this ratio had a radial dependence even in the stage of nanocluster quasi-melting and increased from 10% for central atoms to 40% for peripheral atoms (a shift by 2–3 interatomic distances along the edges in 10^{-11} s). After disordering (fusion) of the whole cluster at >850 K, the root-mean-square displacement in 10^{-11} s was 1 nm for surface atoms; only 60% of atoms had this displacement in the fourth shell, there were 15% of such atoms in the third shell, and out of the 13 central atoms there were none. Analysis of atom displacements upon heating and melting of nanoclusters demonstrated that oppositely directed components of diffusion motion are present in each coordination shell.

Since operational study of the crystallizing phase growth from molten clusters is difficult due to restricted size of the model and duration of nucleation, Polukhin *et al.*[83] studied superfast quenching to give metastable states: amorphous, X-ray amorphous with local structure fragment coherence and quasi-crystalline with predominant icosahedral packing.

The amorphous state of palladium and nickel can be obtained from a melt when the quenching rate is not less

§ For clusters with tangential and radial displacements of atoms and a gradient change in the structure and even in the states of shells, diffusion is a more appropriate term than self-diffusion, which is used by some authors (see, for example, Refs 3, 9 and 86).

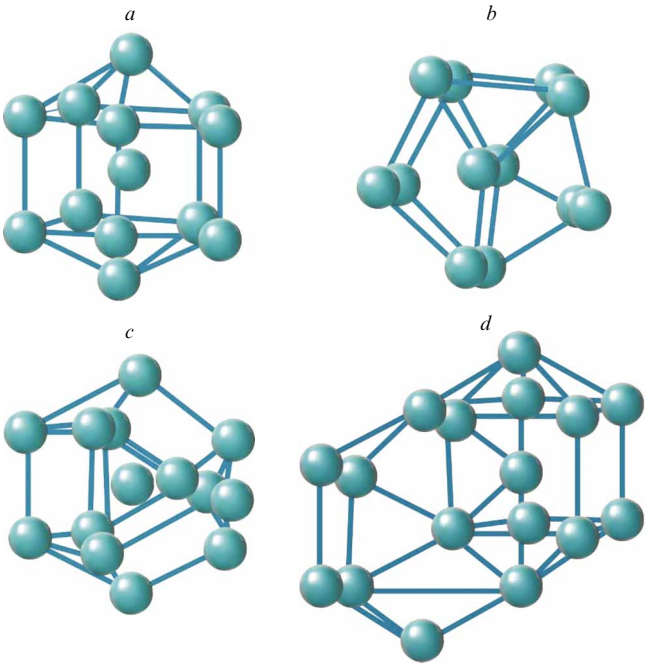


Figure 14. Ino decahedron, side view (*a*) and top view (*b*), the coordination polyhedron of the hcp lattice (*c*) and combined coordinations of the Ino polyhedron and hcp (*d*).[9, 64]

$10^{11}-10^{12}$ K s^{-1}, *i.e.*, in the mode where the computer simulation of cooling can be performed in conformity with real processes. In the case of slower cooling, hybrid forms between octa- and cuboctahedral, amorphous, icosahedral, quasi-crystalline and other structures can appear (Fig. 14).[64] Structural changes that occur on fast cooling are irreversible (the amorphous-type structure is retained; at ~300 K, a glass-like cluster is formed). Note that this was followed most clearly for iron clusters.[9]

The structures of Ni_{561} nanoclusters, unlike Pd_{561}, contain hybrid Ino decahedra. The solid-like state of nickel clusters with regular bcc or Ih structure (or, much less probably, fcc structure) is generated only upon very slow cooling. Nanoparticles of palladium, as well as other platinum group metals with the stable Ih structure,[14, 89–92] also tend to form various hybrids, which arise as a result of coherent coupling of the Ih and hcp packings (approximately in 2 : 1 ratio). These hybrids are decahedron and Friauf truncated tetrahedron with four triangular and four hexagonal faces.[9] Larger structures composed of 20 Friauf polyhedra — Bergman polyhedra, which have both five- and six-membered faces — also form hybrids. This is typical, most of all, of nickel;[9, 90–92] similar structures are also formed upon free condensation of copper nanoparticles from the gas phase.

It is noteworthy that the growth dynamics of nanoclusters (see, for example, Fig. 15) is dictated by the stochastic mechanism of their collisions with the aggregation probability predominating over the decay probability provided that the primary nuclei have reached critical size with several tens of atoms.[93] During smooth heating, melting and subsequent crystallization of these nanoparticles, as noted above, an interface can appear and structure splitting or twinning may occur to give two independent shells of separating clusters (see Figs 8, 16), *i.e.*, the situation resembles the formation of a grain-boundary structure in eutectic alloys. During cooling of the Cu_{2119} nanocluster, the potential energy per atom (see Fig. 13) has decreased, which attests to structure stabilization.[74]

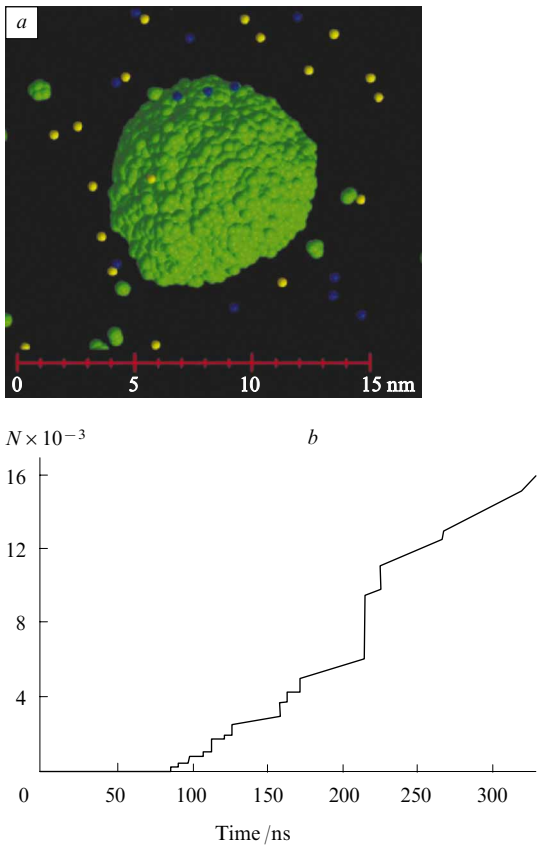


Figure 15. Increase in the cluster size (*a*) and the number of atoms in the cluster (*b*) over 328.8 nm.[93]
The steps correspond to the cluster growth upon coalescence with other particles.

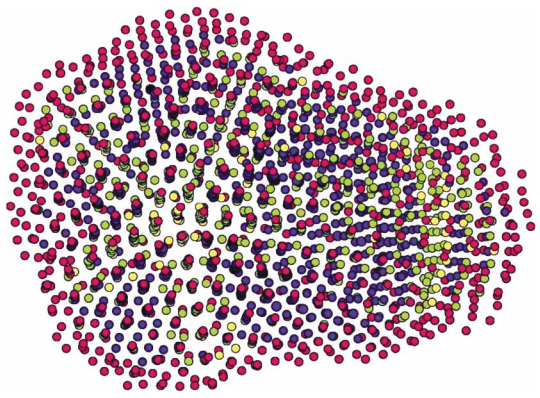


Figure 16. Structure of the Cu_{2119} cluster synthesized from the gas–vapour phase projected on the *xy* plane.[74]

The discrepancy between the MD simulation data and experimental results obtained in the studies of condensation of the vapour–gas mixture is related, most of all, to impossibility to exactly reproduce the real condensation conditions.[49] First of all, this concerns heat removal in the

gas–cluster system[93–95] and maintenance of the required ratio between the partial pressures of the metal vapour and the buffer gas.[96] Due to interaction of metal atoms, energy redistribution upon collisions of the cluster nuclei depends little not only on the cooling gas temperature but also on the density of the vapour–gas mixture (dissociation energy of the Cu_2 dimer is estimated at 2.0 eV, and the thermal motion energy of atoms in clusters is 0.3–0.37 eV for clusters comprising several tens of atoms and ~0.37 eV for clusters of 500 atoms).[93] The time required for the equilibrium to establish upon redistribution of the cluster rotational and vibrational degrees of freedom is shorter than the relaxation times of the internal degrees of freedom.

Thus, melting of the model transition metal clusters occurs *via* transition of regular structure to a disordered structure with high migration mobility of atoms rather than upon a phase change. The mechanism of melting of such clusters is more complicated than the melting mechanism of macroscopic crystals: in the nanorange, melting starts at temperatures that are less than half the crystal melting point, proceeds over a wider temperature range (~1/3 of the heating range) and comprises several stages.[67,74] The nanosize effects in the clusters — small objects with marked density fluctuations and continuous redistribution of the kinetic and potential energy — start to be manifested before melting as structural transitions with continuous interconversion of coordinations (isomerization) and the loss of structure stability.

V. Specific details of thermal size effects in the cluster/substrate systems

The unique properties of nanoclusters are affected by not only the internal coordination and surface morphology,[74,97] but also by their self-assembly as non-aggregated 2D-arrays on substrates or as 3D-arrays in solutions and framework structures and also upon their formation under conditions of coating (encapsulation) by, for example, fullerene-like shells (according to the 'onion' type).[98,99] The electron rearrangements in nanoclusters occur over picoseconds and cannot always be monitored by modern measuring instruments. Important thermally activated processes accompanied by various quantum effects, in particular, the considerable decrease in the electron free path length occur on this spatial and temporal scale. The substrate affects the general surface topology, structure and the charge state of clusters and the self-assembly processes; it is involved in cooperative interaction and electron density redistribution, which, in particular, influences the catalytic efficiency.

The activity of nano-sized clusters is associated with a substantial growth of conductivity of the immobilizer material, which thus acquires semiconductor properties upon electron density redistribution throughout the whole catalytic assembly consisting of metal nanoparticles and the immobilizer.[73] The electron density redistribution enhances the catalytic activity only in the case of the optimal number of atoms in each nanocluster. The average conductivity of this assembly depends not only on the nanocluster size and shape but also on the mutual arrangement of nanoclusters and density of their arrangement on the substrate. For the assemblies of ~2 nm Ni, Pd and Pt nanoparticles, non-activated electrotransport mechanism operates even at relatively low density of arrangement.

V.1. Fragmentation of cluster catalysts

Bukhtiyarov and co-workers[75,100] developed an original approach to the molecular design of heterogeneous catalysts and discussed the 'size effect' problem for different-scale materials ranging from macroscopic to nano-sized ones. A number of active components were studied and the possibility of improving the properties of heterogeneous catalysts such as activity, selectivity and stability was demonstrated, which corresponds to new fundamental advances of the surface theory.[101]

As a development of the known Balandin ideas (see monographs[6,7]) concerning the multiplet theory of catalysis, it was stated[21,22,100] that for the description of selectivity of the chemical processes, it is insufficient to consider only the structural compliance of the precursors and catalysts. If the stabilizing ligand forms rather strong bonds with the catalyst, then chemical transformations can actually involve only one type of metal nanoparticles throughout the whole chemical process with limited displacements of atoms within the vibration amplitude or interatomic distances. In other cases, the catalysts in the reaction mixture are represented by a set of interconverting different-type metal particles of both precursor clusters and their fragments constituting, according to Ananikov and Beletskaya,[22] a 'cocktail' (Fig. 17 *a*, *b*). The term 'cocktail', in their opinion, implies the presence of a definite catalysis mechanism, structure and composition and has nothing to do with the obscure notion 'centres of unidentified nature'. Indeed, in complex Heck and cross-coupling reactions, leaching may be not limited to the removal of only single atoms but be accompanied by fragmentation of clusters on substrates.

Figure 17 *c* illustrates the nanomechanics of complex leaching of the cluster catalyst precursors (M_N) upon their interaction, successive destruction and migration of single atoms and several-atom fragments into the solution in the reaction steps (R is substituent, X is reactant) and the *in situ* formation of high-performance catalytic 'cocktail' with the subsequent interconversion and possible self-assembly of cluster fragments at the final stage. In this case, additional centres of catalysis would appear on dissociated fragments; like the precursor clusters, they also would disintegrate with abstraction of single metal atoms under the action of the oxidant present in the solution,[22,102] which was actually observed in the experiment.[103]

Heterogeneous catalytic reactions involving nano-sized palladium particles have specific features caused by atom dynamics and particle fragmentation. During leaching, atoms of the precursor nanocluster may oscillate, being located on the surface, migrating to the solution (even in groups during fragmentation of the precursor cluster[22]) and moving away by interatomic or longer distances. They can remain in the solution for some time or till the end of the reaction if there are no chemical prerequisites for their self-assembly (at least partial) to the initial states. Leaching can be substantially accelerated upon the addition of other reagents (atoms).[104] The ability of metal nanoparticles to self-assemble *in situ* at the final step of the catalytic reaction can be regarded as a sign of recycling or reversibility;[105,106] this gives rise to new centres of self-assembly in the solution of not only single atoms but also atomic groups formed upon fragmentation of the precursor clusters.

Apart from noble metal nanoclusters, excellent catalytic properties in homogeneous and heterogeneous processes are

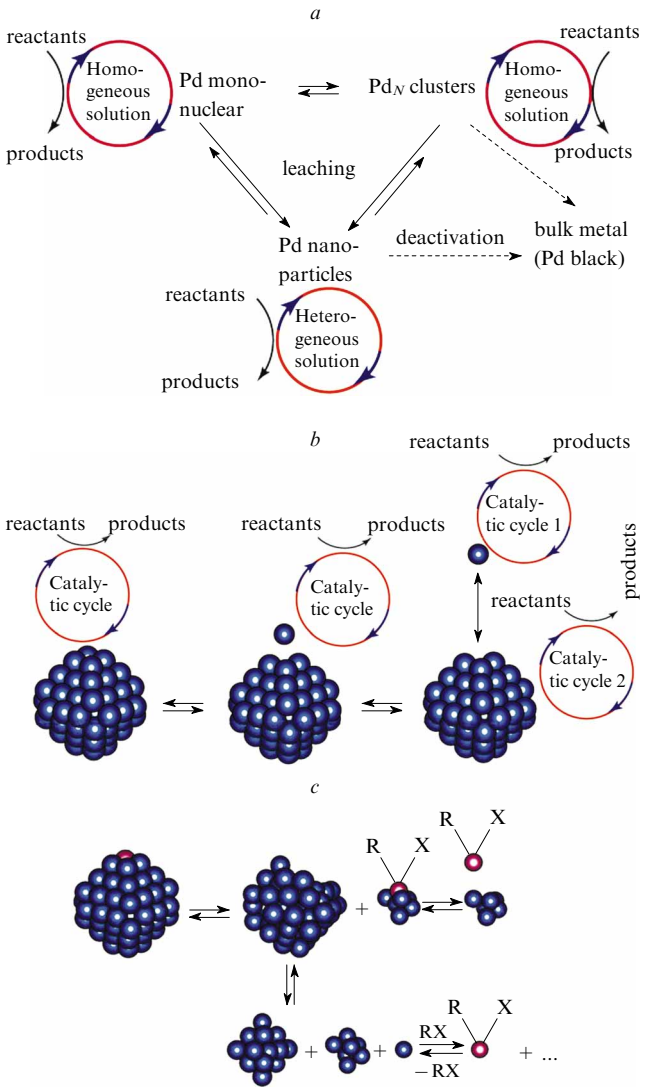


Figure 17. Flow chart of the *in situ* formation of the highly efficient catalytic cocktail (*a*, *b*) and complex leaching of the precursors of cluster catalysts (*c*) upon interaction and successive destruction down to atomization and transfer to the solution.[22]

exhibited by nanoparticles of cheaper nickel and the salts $[M(ZR)_2]_n$, where M is metal; Z = S, Se; and R is organic substituent.[107]

The application of nano-sized catalysts is, in some cases, more efficient and economical if binary stationary systems are used. An example of preparation of such systems is electrodeposition coating of a graphene-supported 2D ensemble of gold nanoparticles (<5 nm size) by a monolayer of palladium atoms.[98] This catalyst having smaller nanoparticles than traditional catalysts of gold particles (~16–19 nm) is structurally stable, environmentally safe and has a higher hydrogen after-burning coefficient.[108, 109]

As the number of atoms in the cluster decreases, the distance between the energy levels increases and the catalytic activity of nanoclusters sharply grows. Taking account of the temperature range of a catalytic reaction, it is possible to determine the optimal size of the clusters (for clusters comprising from 300 to 1000 atoms, it is 1.5 to 7.5 nm).

It has been noted above that the catalytic activity depends on the number of atoms having stationary positions in the most catalytically active sites — at the vertices and edges.[9, 73] In the case of platinum clusters, the highest catalytic activity is manifested when atoms are located in high-coordinate positions on the faces, while the high density of edges on the cluster surface creates an additional potential barrier to the reaction kinetics; hence, the effect can be attained in the case of increased areas of faces, *i.e.*, for large clusters with sizes of >10 nm (up to several tens of nanometres). Thus, the catalyst selectivity and maximum activity are related to both electronic and geometric factors, which predetermine the ratio of the number of atoms on the surface to the number of atoms in the bulk in the cluster catalysts in some chemical process. For example, the highest catalytic activity of nickel and palladium in benzene hydrogenation is achieved if this ratio is close to unity.[75, 76]

These phenomena reveal the nature of the nanocluster states related, on the one hand, to a considerable effect of the surface and, on the other hand, to the quantum restrictions on the nanoscale of cooperative processes.

For increasing the efficiency of catalysts, in addition to thermally stable structure, high density of active sites (vertices and edges) and great total contact surface area, it is necessary to thoroughly select the material of substrates. Depending on the type of catalytic reactions, aluminium, titanium and silicon oxides and carbon materials (graphite, graphene) are widely used. These materials not only serve as substrates for cluster attachment but also affect the process intensity. This effect is especially pronounced in the case of low pH values where the electronic properties of metallic catalysts, including noble metal catalysts, sharply change. The contact of metal clusters with metals induces thermoelectric effect with electron transfer to the metal with lower Fermi energy, while the contact with a dielectric induces polarization; this would exert a 'locking' effect, which will be more pronounced if the metal cluster with relatively low ionization potential is in contact with a dielectric with a high ionization potential.

It is noteworthy that irrespective of the diversity of precursors in the reactions with nano-sized catalysts (this may be metal salts, metal complexes, colloid systems, separate metal particles or supported particles), reverse catalytic leaching processes can occur if organic compounds are present in solutions.[21] An important stage of industrial catalytic processes (including filtration and centrifugation stages) is regeneration of the expensive catalyst. A topical problem is to prevent the environmental pollution by nanofragments, most hazardous among which are the contaminant nanoparticles (Pt, Au) activating metabolism and triggering self-killing of cells in living organisms.[110, 111] One cannot but mention the advances in the field of stabilization of metal clusters in nanostructured matrices of highly cross-linked polystyrene. These catalytic systems were obtained with nanoclusters formed by Pt, Ru, Pd and their alloys (Pt–Pd, Pt–Ru, Pd–Ru, Pt–Pd–Ru). These systems proved to be efficient towards selective oxidation, hydrogenation (including enantioselective version) and fine organic synthesis.[112]

V.2. Interfaces in M/G$_n$ systems

Functional elements with contacting interfaces of cluster-islet metal coatings on oxides and graphene occupy the central place in the development of innovative devices for

optoelectronics, gas detectors, heterogeneous catalysts and so on.[113–116] The adhesion and adsorption properties and thermal stability of these 2D systems depend on many factors: electronic and atomic structure, characteristics of interatomic bonds, charge state, morphology and coherence of the internal coordinations in metal clusters and on the type of fragmenting of deposited films, deposition methods, substrate material and properties, the nature of bonds at the metal/substrate interface, *etc*.

Graphene can be synthesized by using technology-intensive thermal methods, in particular, CVD. The primary stage of the CVD process is the preparation of a vapour–gas mixture from carbon and hydrogen by thermal decomposition of, for example, methane at 1300 K followed by sorption of the carbon atoms on a heated metal foil surface. On cooling, carbon atoms are desorbed, thus enabling controlled formation of one or several graphene layers from these atoms on the metal surface.

A natural criterion for the selection of the foil metal is excluding the development of bulk diffusion. From this standpoint, copper is most workable for the production of monolayer graphene. In the case of a nickel substrate, metastable Ni_2C phase is formed in the near-surface layer. Upon chemical removal of the metal, monolayer graphene sheets can also be produced from this phase (the optimal temperature is 750–980 K).[113–117] Graphene synthesized in this way as a 2D crystal is separated from the metal surface by a polymer adhesive (or by chemical dissolution of the metallic substrate) and is transferred onto the substrate as a functional element.[115–118] The thermophysical characteristics of the metal–graphene composite were found to be high. The thermal conductivity [$\sim$460 W (m K)$^{-1}$] was higher than for crystalline samples [$\sim$380 W (m K)$^{-1}$]; therefore, effective heat withdrawal is possible in the basic blocks of computer equipment such as field effect transistors and switches.

Deposition of metals (including Cu, Pd and Ni) onto graphene or graphene coating of clusters (synthesis of the endohedral clusters $M@C_n$)¶ is of considerable interest for the production of nanomaterials with unusual magnetic properties.[118, 119] The interaction of transition metal atoms with defective graphene induces hybridization of carbon sp^2 orbitals with the s-, p- and d-orbitals of the metal. The metal atom that occupies a single or double vacancy and the surrounding carbon atoms form a cluster dispersed phase with unusual magnetic properties in which the bond energy between the graphene carbon atoms and the transition metal atoms deposited onto it reaches 0.2–1.5 eV.[118]

Note that nanoparticles composed of iron and nickel atoms having even numbers of valence electrons are nonmagnetic, while the nanoparticles of cobalt and copper atoms having odd numbers of such electrons are magnetic. The magnetic properties of copper and gold clusters differ from those of clusters of other transition metals. Since the copper and gold atoms have filled d-orbitals, a substantial portion of atomic magnetism is due to the s- and p-states (50% for Au and 30% for Cu). The other portion of the magnetism is due to the environment of these atoms representing the carbon atoms of the cluster dispersed phase. The formation of magnetic complexes is possible only at very low temperature and precise focusing of cluster beams. Only in this case are the vacancies in graphene filled by transition metal atoms. However, at high temperatures, defects in graphene can also be formed spontaneously. It is not clear as yet how much these defects are stable.[120]

It should be borne in mind that the characteristic vibrations of the fragmented graphene sheets initiate their corrugation and folding, and this induces bond recoordination to give more complex stable structures:[121] depending on the area of the sheets, this may be fullerene molecules or nanotubes,[122, 123] transition metals being exactly the catalysts for the growth of such structures.[124]

The range of materials based on cluster dispersed systems formed by transition metals promising for practical applications is rather broad. Such materials should be not only stable but also chemically inert. For example, unlike noble metals, nanodispersed copper materials having high electrical and heat conductivity are highly chemically reactive: in open air, they are soon coated by an oxide film even at room temperature.[98]

Graphite coating solves the problem of protection of metal nanoparticles, which rapidly degrade under the action of air oxygen and opens the prospects for replacing the functional noble metal particles by carbon-coated particles of cheaper metals (*e.g.*, iron or copper), in particular, for the design of the hardware components for data recording, storage and processing devices and for the manufacture of stable magnetic liquids. It is necessary to add that graphite-coated particles are more compatible with biological tissues than particles of gold and other platinum group metals.

In the absence of dangling covalent bonds (for example, as in fullerites, carbon nanotubes and graphene), graphite-coated particles are not chemically reactive.[110, 111] Encapsulation of nanoparticles changes considerably not only their thermodynamic but also electrophysical (electronic properties and electrical and heat conductivity) and mechanical properties,[125, 126] which are of interest for the developing nanotechnologies.[127–134] Encapsulation is carried out by a variety of physicochemical methods: using arc discharge,[134, 135] pyrolysis of organometallic compounds,[136] CVD,[137, 138] mechanochemical activation[139] and other.[140–144]

The results of experiments on encapsulation of copper[98] and iron[99] nanoclusters by deposition of secondary products of detonation of dispersed precursor phases (ammonium and metal nitrates) are of great promise in this respect. The graphite-coated copper particles were obtained using a highly explosive mixture of approximately the following composition/mass %: (10–20)% ammonium nitrate + (50–70)% copper + (5–8)% carbolite. A study of the morphology of contact surfaces of encapsulated nanoparticles demonstrated that the thickness of the graphite coating shells is 3–5 nm and the maximum size of the copper intercalates in Cu@G did not exceed 20 nm. In the region ($\sim$0.34 nm) between the metal and graphite shell surfaces, there were no voids. The structure of intercalated copper nanoparticles was identified as fcc.

Luo *et al.*[99] reported the noteworthy results of gas-phase synthesis of graphite-coated iron nanocrystals where a mixture of readily ignitable gas (methane), an oxidant and aerosol of a $Fe(CO)_5$ solution in acetone was used as the precursor. A crystallographic study using the selected area electron diffraction (SAED) method revealed clear-cut

¶ Such coated materials are designated by the abbreviation GCN_S (Graphite-Coated-Nanoparticles: Nanocrystalls, Nanoclusters, Amorphous Particles).

reflections corresponding to the bcc-structure of the single crystalline α-Fe phase. The data from X-ray photoelectron spectroscopy confirmed the presence of both iron single crystals (peaks at 706.5 and 720.6 eV) and carbon sp^2-bonds (peak at 284.80 eV). The diameter of the spherical α-Fe single crystals in the α-Fe@G nanoparticles varied from 15 to 50 nm (the average value was ~32 nm). A study of the morphology of α-Fe particles (~45 nm) demonstrated that a 5–8 nm-thick coating had an onion type layered structure and the contacting (002)G/(110)Fe planes were separated by a 0.20–0.34 nm distance. Relying on the experimental results, a schematic structure of the graphite-coated clusters was proposed (Fig. 18).

Experiments on the encapsulation of metal nanoparticles into carbon nanotubes (CNTs) are successfully carried out for the design of novel materials for electronic 1D elements (nanowires) using *in situ* pea-pod technique, scanning and transmission electron microscopy and the SAED method.[145, 146] This chemically inert nanowire with a length of several hundreds of nanometres has a unique mechanical strength at a diameter of several tens of nanometres and represents by itself a unique element for data storage upon appropriate selection of metal particles.[146]

The described 1D material acquires specific properties due to the change in the Fermi energy, density of charge carriers and the band gap width of graphene.[147] Note that liquid metals cannot be inserted into nanotubes due to very high surface tension forces; therefore, salts are used as precursors, which are heat-treated directly in the nanotubes. The endohedral $M@C_{60-90}$ clusters of appropriate size can be inserted.[147–151] Under the action of encapsulated nanoparticles, the CNT walls are markedly deformed; however, they still withstand heating with retention of crystal-like phases in them up to 1550 ± 50 °C, which is higher than the melting point of the corresponding bulk metal phases. Only upon maintenance at this temperatures for two hours, the material starts to flow (melt) under the action of the pressure of walls that has increased upon heating, and subsequently it is actually squeezed out from the tube.[146]

The strength of surface cohesion at the interfaces in encapsulated fullerene-like onions,[98, 99] nanotubes[145–151] and layered materials[152–157] and the intensity of atomic migration in them upon thermal activation are determined, to a large extent, by the strength of the M–C bond being formed, which can be described in terms of the density functional theory. It was shown[152] that the thermal stability of the interface structure of a copper monolayer film on graphene depends appreciably on the parametric incommensurability of the crystal lattices, namely, the fcc lattice of copper and the hexagonal lattice of graphene, which gives rise to considerable stresses. The development of velocity (of about 0.01 nm ns^{-1}) at the borders of graphene sheets related to the characteristic vibrations of the sheets (see above) should also be taken into account. The enhancement of characteristic vibrations with heating and the interaction between copper atoms and graphene carbon atoms give rise to atom recoordinations to give a more complex stable structure.[152, 153]

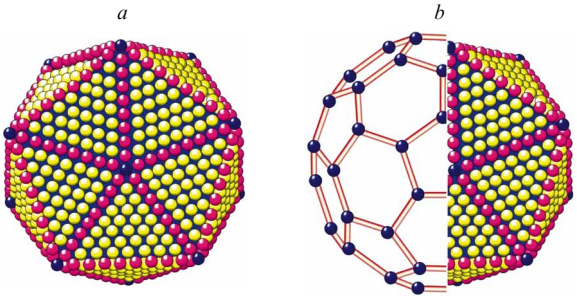


Figure 18. General view (*a*)[9] and cross-section (*b*)[98, 99] of free metal cluster encapsulated into a fullerene-like shell.

V.2.a. Sorption

A graphene layer deposited on a metal surface protects the surface from adsorption and chemical oxidation. By means of MD simulation, it is possible to elucidate how the energy of cohesion of metal–graphene layers, the electron band structure and the transfer properties are related to the formation of the atomic structure of the interface. The bonds formed upon the contact of graphene with most transition metals are weaker than covalent bonds but stronger than van der Waals interactions.[67] In terms of strength of interaction with graphene, metal atoms can be conventionally classified into two types:

— the first type comprises the Fe, Co, Ni and Pd atoms, which are bound to graphene more strongly, thus stabilizing the planar structure of graphene even during heating;

— the second type comprises the Al, Cu, Ir, Ag, Au and Pt atoms, which weakly interact with graphene; this interaction does not prevent reorganization of some planar (clover-like) atomic coordinations into steric coordinations; the latter not only induce the corrugation of graphene planes but also give rise to cluster structures with specific coordination, namely, ring clusters formed by graphene atoms and adatoms of the adjacent (111) surface of the metal.[67] In ring clusters as the sites of the moiré structure being formed, transitions from the planar network of the graphene C=C double bonds to a tetrahedral network of C–C single bonds are possible.

In the transition metal interstitial alloys M_xC_{1-x}, the carbon atoms occupy octahedral positions; hybridization of the carbon atomic orbitals with the metal d-orbitals is possible (the true nature of the M–C bonds in the alloys is not entirely clear as yet).[153–159] Upon the M/G contact, the position of the metal Fermi level changes up to the intersection with the bands of carbon π- and π*-orbitals (*i.e.*, with the occupied and vacant states separated by the carbon Fermi level). As follows from analysis of the curves shown in Fig. 19 and calculations of the tensile strength (18.70 GPa for Ni/G *versus* 2.92 GPa for Cu/G), the greater the binding energy, the higher the tensile strength.[159] This mechanism of formation of the interface with specific properties and interactions is attributable to the short-range character of the dipole dispersion attraction forces initiated by the charge redistribution between the contacting graphene and metal surfaces (Fig. 20).

The results of *ab initio* calculations of the key parameters of the electronic structure of the M/G system are presented in Table 3. The left-hand part of the Table shows data for metals with interfaces (with the cohesion energy E_c in the conventionally chosen range of $0.031 < E_c < 0.046$ eV per atom and the length of interatomic bonds along the normal to the interface plane of $d > 0.296$ nm) classified as physical-adsorption ones, while the right-hand part shows values for interfaces classified as

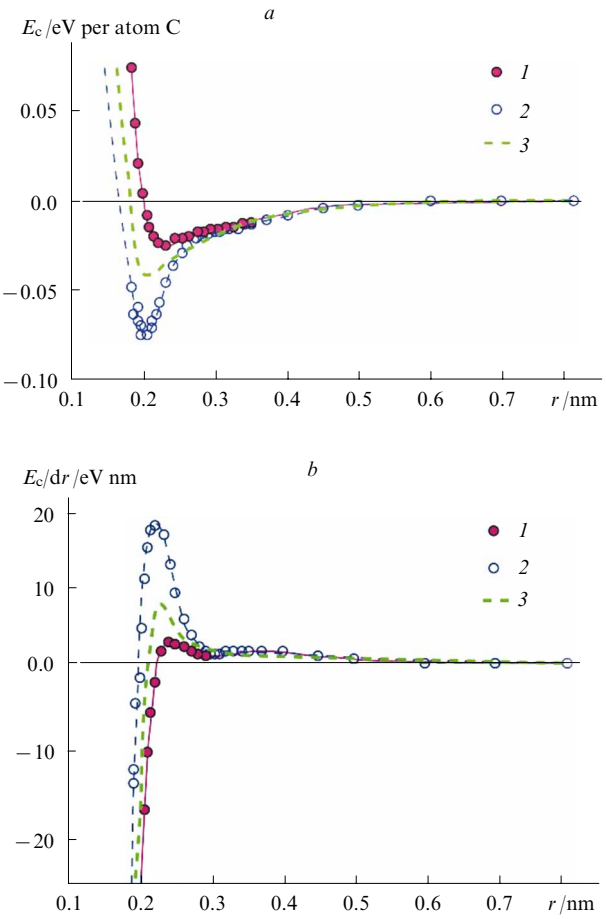


Figure 19. Interface binding energy (E_c) (*a*) and interaction force (*b*) *vs.* the distance (r) between atoms of the (111) face of a metal cluster and C of a graphene substrate.[159]
(*1*) Cu/G, (*2*) Ni/G, (*3*) Pd/G.

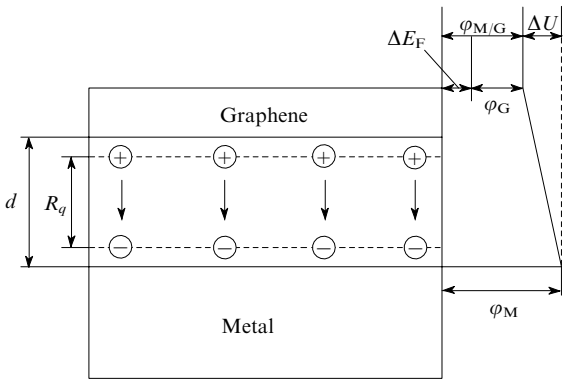


Figure 20. Scheme of the change in the electronic structure (with levelling shift of the Fermi energy ΔE_F) upon formation of the interface with the cohesion energy E_c.[157]
The potential ΔU appears upon charge redistribution and displacement by the distance R_q to the contact zone between the graphene and metal planes spaced by the distance d; φ_M and φ_G are the electron work functions for the metal and graphene, respectively.

chemisorption ones (with the energy E_c in the range of $0.033 < E_c < 0.432$ eV and bonds shorter than $d < 0.344$ nm). The calculated data are similar to experimental results reported in several publications.[156, 161–163]

Since the density of the fermionic states for graphene is low as compared with that for transition metals, the Fermi level shifts upon charge transfer from the metal (for levelling of graphene and metal charge densities): for gold, the shift is ~0.20 eV, and the greatest shift has been found for aluminium (0.49 eV). The bond energies found for the interface pairs in the case of physical adsorption vary from one metal to another in the range from 0.030 to 0.046 eV and the corresponding distances are ~0.3 nm and more (for example, for aluminium, $d = 0.359$ nm). The Fermi energy shift to the Dirac level (point) for interfaces with physical adsorption can be approximately estimated as the difference between the electron work functions for the metal and graphene: $\varphi_{Pd} \approx 4.3$ eV, $\varphi_{Cu} \approx 4.40$ eV (see Ref. 161) and $\varphi_G \approx 4.48$ eV (see Ref. 156).

In the interface formed upon physical adsorption under weak cohesion of contacting surfaces, the electronic structure of graphene remains virtually unchanged. In view of this fact, it was assumed that the φ_G value for the interface is equal to that for an isolated graphene plane. The above-noted dependence of ΔE_F can hold to within 0.5 nm.[153] The change in the work function upon the charge transport with the shift ΔU corresponds to the electron–hole charge transport from the metal to graphene, which specifies the properties of the doped system. Thus, on the contact of the metals

Table 3. Results of quantum mechanical calculations for the M/G interfaces.[155, 157]

Parameter	Physical adsorption (doping)					Chemisorption					
	Al	Ag	Au	Cu	Pt	Ir	Pd	Ru	Co	Ni	Ti
E_c /eV per atom	0.042	0.031	0.037	0.030	0.046	0.033	0.089	0.139	0.432	0.133	0.417
$-\Delta q$ /10^2 e$^-$	0.3	0.7	0.78	0.81	0.11		0.13		0.23	0.21	
d /nm	0.359	0.326	0.327	0.296	0.318	0.344	0.247	0.222	0.211	0.207	0.213
ΔE_F /eV	0.49	0.35	0.20	0.47	−0.31	−0.23					
a_c /nm	0.405	0.409	0.408	0.361	0.392	0.384	0.389	0.271	0.428	0.251	0.295
c_h /nm								0.428	0.409		0.470

Note. The following designations are used: E_c is the cohesion energy of the metal and graphene planes per carbon atom; d is the equilibrium interatomic distance between the contact layers; ΔE_F is the shift of the Fermi energy; Δq is the quantity of charge [153] (doping) transported to align the Fermi levels of the metal and graphene; a_c, c_h are lattice parameters.[158, 160]

discussed here and graphene, which have different electron densities, the Fermi energy is levelled due to the overall electron transport; finally, the charges $\pm\Delta q$ ($+\Delta q$ from graphene and $-\Delta q$ from the metal) are arranged at the distances R_q (see Fig. 20).

The appearance of new levels of states in the band gap caused by hybridization and the considerable shortening of the equilibrium interplanar spacings in the interface result in the complete disappearance of the tunnelling conductance barrier typical of systems that have been formed upon charge doping (physical sorption). The contributions of the repulsive Pauli interactions in the case of chemisorption enhance the effect of hybridization on the change of states in the band gap. This brings about dispersion of the spectrum of π-states, and the hybridization energy levels fall in the region of metal d-states, thus initiating further shift toward the band of high-energy unoccupied π-states. Thus, in the case of chemisorption, hybridization results in overlap of the d- and π-states of the metal and graphene carbon atoms, respectively, and in band gap opening (appearance of occupied levels) in the π-bands with chaotic distribution of the arising states. Under the action of interactions determined by the nature of sorption (chemisorption or adsorption), superposition of the metal and graphene lattices of different topology affords various moiré superstructures or superlattices.[67, 74] The cells of these structures comprise in some cases several thousand atoms.

The MD simulation of the Ni/G,[164] Pd/G[67, 74] and Cu/G[74, 119] interfaces (listed in the order of decreasing strength) with interaction potentials estimated by the density functional theory method[10, 159] involved comparative analysis of the effect of metal subsystems on the thermal evolution of M/G systems depending on the strength of binding of the contacting metals and graphene. Analysis was performed of the influence of heating on the triggering of disordering and melting processes and accompanying structure changes — thermally activated ordering of ring cluster configurations, destruction of the regular structure of the system, quasi-melting and order to disorder transition, the analogue of melting of two-dimensional systems.

For simulation of the contact surfaces of transition metals and ring clusters using the tabulated results of the quantum mechanical calculations of interaction energies, parameters of the Sutton–Chen[10, 66] potentials for Ni and Cu and the Cleri–Rosato[65] potentials for Pd were established. The methods for estimation of interaction potentials were developed deliberately for the simulation of metal surfaces and layers in interfacial contacts[152–157, 165, 166] (including M/G interfaces) and, first of all, for simulation of atomic dynamics in the layers adjoining the interface, taking into account not only many-body interactions but also long-range effects. The interatomic interactions in graphene were described using the Tersoff potential,[167, 168] which was constructed based on the concept of coordination bond ordering. In the calculation of interactions between carbon atoms i and j in the graphene layers, reported[9, 167] parameters of the potential functions were used. The interactions of metal (Cu–Cu, Ni–Ni) atoms in the M/G_n systems were estimated, as in the case of simulation of isolated clusters, by the Sutton–Chen procedure in terms of the EAM formalism.[10]

The arrangement of metal atoms above the unit cells of the hexagonal lattice of monolayer graphene in the zone of M/Ge interface formed at 300 K (where M = Cu, Ni) was uniform but had vacant sites as a result of incommensurability of the metal and graphene lattices:

$$R_{Cu-Cu} = 0.2556 \text{ nm}, R_{Ni-Ni} = 0.2489 \text{ nm}, R_{C-C} = 0.142 \text{ nm}$$

According to the density functional theory estimates,[169] the Cu–C distance was 0.2243 nm and the Ni–C distance was 0.2018 nm. Ultimately, the arrangement of the metal atoms corresponded to the extended (deformed) (111) plane of the fcc structure with a minimum distance between the atoms.

It has been noted above that the thermal stability of the M/G structure (in particular, a copper monolayer on graphene) is affected, apart from the parametric incommensurability of the crystal lattices, by the energy of characteristic vibrations of the graphene plane, which also cause considerable stress and deformation (corrugation). An algorithm has been developed for preventing the deformations by counterbalancing the factors that cause them. The undesired effects were smoothed down upon increase in the coherence scale of covalent interactions in the model from 0.21 to 0.23 nm with introduction of an additional Lennard-Jones potential, which damps the metal and carbon atom dynamics for local coordinations of each hexagonal unit of graphene. In addition, to prevent gyrations of the M/G_n systems, a correcting potential was additionally introduced for each graphene atom according to a publication.[169]

A regular packing of metal atoms in the (111) plane above the graphene surface seemed to be optimal for the interaction with the graphene substrate; however, it was metastable at the initial simulation temperature of 300 K. As was to be expected, at this temperature, the M–M interatomic distances started to decrease and the initial packing geometry started to change. Determination of the size of a copper film implies finding of the average coordinates (x, y) of three terminal copper atoms that have not vaporized. The removal of an atom from all other metal surface atoms to a distance of >0.3 nm served as the criterion for vaporization.

Starting from the initially specified temperature of 300 K, the system temperature was increased by 500 K in every time step, and the calculation was continued. The final calculation corresponded to a temperature of 3300 K. For comparison, the same calculations were performed for the M/G_2 system (G_2 is the bilayer graphene). The mutual arrangement of graphene sheets corresponded to the Bernal packing ($ABAB\ldots$), as in the bulk graphite. The distance between the graphene sheets was taken to be equal to the value predicted by density functional theory calculations (0.3347 nm).[159] The interaction between the carbon atoms belonging to sheets A and B was estimated using a parametrized potential (see Refs 169–171). A graphene sheet containing 210 atoms was extended along the x and y direction upon the use of periodic boundary conditions in the same way as the metal subsystem. Along the z direction, the boundary conditions were free. The total energy of free monolayer graphene found at 300 K was -7.02 eV, which is consistent with the quantum mechanical calculation (-6.98 eV).[172] The calculated copper–graphene interaction energy was -1.4 eV at this temperature. The heat capacity (C_V) of monolayer graphene calculated *via* kinetic energy fluctuations increased from 19 to 28 J (mol K)$^{-1}$ in the temperature range of $300 \leqslant T \leqslant 1300$ K, which

corresponded to experimental values of 23.74–26.80 J (mol K)$^{-1}$ (see Ref. 173).

V.2.b. Thermal diffusion

The atomic dynamics of interfaces in the M/G systems (where M = Pd, Cu, Ni) formed taking account of the structure of G was studied based on analysis of components of the diffusion coefficients (Figs 21–23).[74, 119, 164] Since the placement of metal clusters on a graphene sheet implies, from the geometrical standpoint, transition from a two-dimensional to a three-dimensional system, it was expedient to consider separately the atom mobility within the xy plane (D_{xy} component) and along the z direction perpendicular to this plane (D_z component). The orders of magnitude of these values are often estimated using the expressions

$$\langle \Delta z^2 \rangle = 2 D_z \tau$$

where $\langle \Delta z^2 \rangle$ is the particle displacement in the specified direction (more precisely, the mean square of the displacement along the z axis),[8]

$$D_{xy} = \frac{\langle \Delta r_{xy}^2 \rangle}{4\tau}$$

$$\langle \Delta r_{xy}^2 \rangle = \frac{1}{N n_t} \sum_{i=,1}^{N} \left[r_{xy}^{(i)}(t) - r_{xy}^{(i)}(t_0) \right]$$

where

$$r_{xy} = \sqrt{(x^{(i)})^2 + (y^{(i)})^2}$$

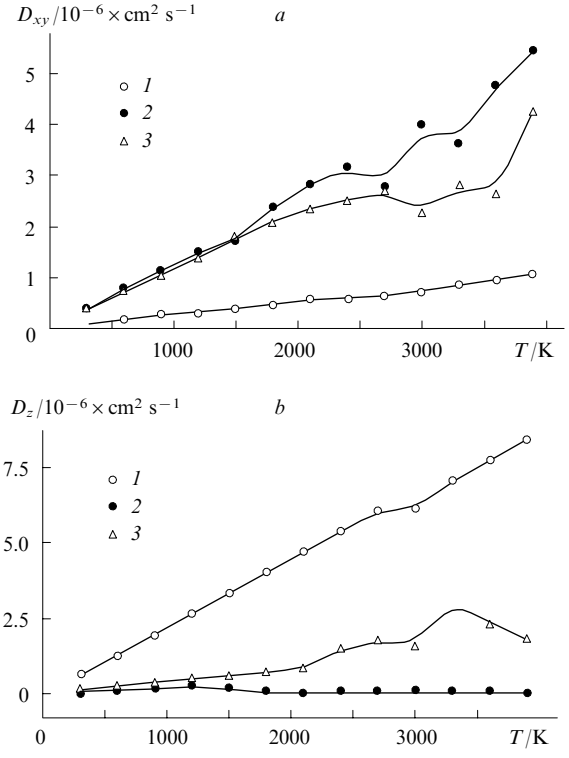


Figure 21. Temperature dependences of components of the diffusion coefficients D_{xy} (*a*) and D_z (*b*) for palladium atoms in the Pd_{13}/G systems with the fcc (*1*), Ih (*2*) and rcp (*3*) structures.[74]

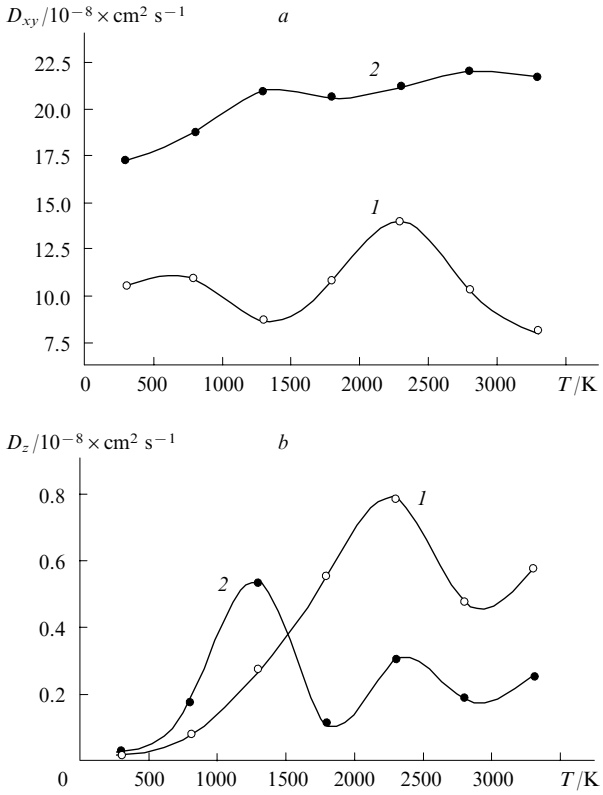


Figure 22. Temperature dependences of components of the diffusion coefficients D_{xy} (*a*) and D_z (*b*) for copper atoms in systems with mono- (Cu/G) (*1*) and bilayer graphene (Cu/G_2) (*2*).[119]

τ is the observation period from time t_0, t is the current time, N is the number of atoms in the two-dimensional system, n_t is the number of initial time periods t_0.

The interaction of the carbon atoms of the monolayer graphene with the nickel and copper atoms in the adjacent (111) planes gives rise to three packing modes as ring clusters with coordinations of ~4–8 carbon atoms in the cells being formed, which is manifested as specific atomic dynamics and the pattern of temperature dependences of the diffusion coefficients of the interfacial heterostructures.[67, 119, 164] In the studies of the latter, it is necessary to take into account the band structure of the metal atoms and the degree of hybridization of the carbon π-states with the transition metal d_z states (this determines the strength of the M–C bonds and, hence, the activation energy of diffusion) and the predominating channels and saddle points in the potential energy curve of diffusion.

Analysis of the temperature changes in the kinetic coefficients D_{xy} and D_z, which characterize the mobility of metal atoms in the temperature range studied for interfaces differing in the character of binding (see Figs 21–23), demonstrated that the increase in the D_{xy} component on heating is most pronounced for the diffusion of copper atoms in the Cu/G system: near 2000 K, the D_{xy} value was almost twice as high as at 1120 K and was $\sim 14 \times 10^{-8}$ cm^2 s^{-1} (see Fig. 22 *a*). This attests to a weaker interaction of copper atoms (and lower activation energy of the diffusion process) with carbon atoms as compared with Pd–C (see Fig. 21) and Ni–C (see Fig. 23) interactions on

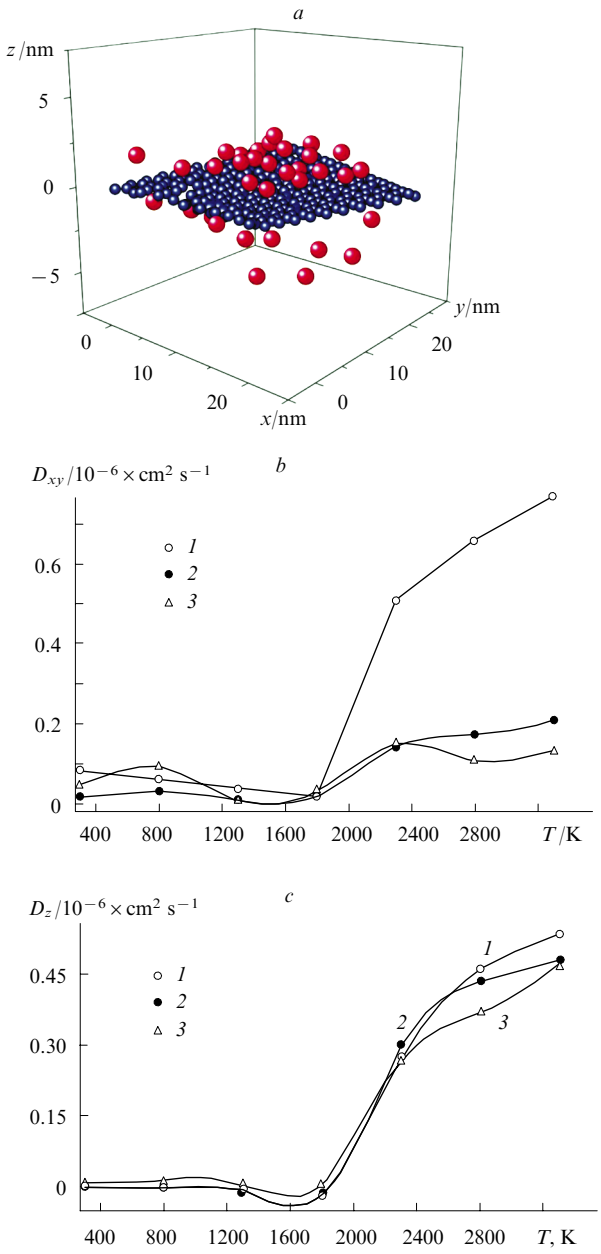


Figure 23. Heating-induced change in the configuration of the nickel–graphene system with two-sided arrangement of nickel clusters on the graphene sheet (*a*) and components of the diffusion coefficient of nickel atoms D_{xy} (*b*) and D_z (*c*).[164]
(*a*): heating up to 1300 K in 200 ps; (*b*, *c*): (*1*) for one-sided arrangement Ni/G; for two-sided arrangement Ni/G/Ni: (*2*) Ni is above, (*3*) Ni is below.

graphene. Upon temperature rise, the D_{xy} component for copper atoms decreases, while the D_z component, conversely, increases (see curves *1* in Fig. 22). The decrease in D_{xy} is due to the gradual drawing together of copper atoms, *i.e.*, consolidation of the contacting metal cluster layer. The increase in D_z is related to enhancement of the atom mobility in the direction free for movement. The substantial growth (surge) of the D_{xy} value near 1150 K for the Cu/G$_2$ system (see Fig. 22 *a*, curve *2*) and the D_{xy} and D_z values at 2150 K for the Cu/G system (see Fig. 22, curves *1*) can be interpreted as approach of the order–disorder transition point (analogue of melting) and more intense disorder in the copper layer adjoining graphene (the melting point of the copper phase is 1357 K). The decrease in D_z at temperatures of <500 and ~2800 K can be regarded as fluctuations caused by adjustment of the structure of the contacting layer of copper atoms (and the arising fluid film) to the graphene structure.

The increase in the atom mobility in nickel-containing systems is also accompanied by thermally activated ejection of carbon atoms (at higher temperature than for Pd/G or Cu/G systems) upon the displacement of metal atoms in contact planes towards the interface being formed (see Fig. 23).The melting point of the fcc Ni_{561} cluster placed on graphene determined by MD-calculations[67] using the Sutton–Chen potential was 1100 ± 50 K (the isolated Ni_{5083} cluster melts at ~1250 K).[74] However, the diffusion coefficients of nickel in the Ni island films in the horizontal (D_{xy}) and vertical (D_z) directions change slightly up to 1800 K (see Fig. 23). This is due to maintenance of the coherence and thermal stability of the cluster atomic structure and the partial consolidation (2%–3%) of this structure caused by strong interatomic interactions, which is also typical of Pd–C contacts at moderate heating temperatures. Above 1800 K, the diffusion coefficients characterizing the atomic dynamics in different directions increase.

All of the considered systems (Cu/G, Ni/G, Pd/G) displayed the following common feature of metal atomic dynamics: as the temperature was raised to 3000 K, in the graphene-adjoining layers of the metal films (faces in the case of palladium clusters), the mobility (D_{xy}) increased and the interatomic distances increased (by $\sim30\%-50\%$) in the longitudinal direction ('zigzag' direction) with respect to the transverse direction ('chair' direction) of the graphene structure. In the presence of Ni clusters, on both sides of the graphene sheet (see Fig. 23 *a*), the carbon atom migration diminished $\sim$4-fold and the structure stability increased due to metal atom interactions through the graphene sheet (their mobility is mutually retarded, most of all, in the *xy* plane). In the case of Ni films located on either one or two sides of the graphene sheet, the pattern of temperature dependence of D_z for the two systems bears more resemblance, which can be attributed to the relaxation recoordinations of the hybridized bonds in film layers adjoining the hexagonal lattice of graphene (*i.e.*, displacements that reduce the energy of deformation stresses caused by the incommensurability of the atomic packings in the metal and graphene layers). Note that the coefficient D_{xy} of graphene is, most often, higher than D_z by a factor of tens. This attests to high strength of bonds between the carbon atoms in graphene, which are not broken upon interaction with the metal atoms deposited onto it even at high temperature.

The temperature dependences of the diffusion coefficients D_{xy} and D_z of carbon atoms were non-monotonic for Pd/G and Ni/G interfaces, which can be attributed to rigidity of the C–C bonds and strong influence of collective interactions, responsible for a complex profile of the potential barriers of the diffusion channels, on the structure formation. As the temperature is raised to 1200–1500 K, the mobility of carbon atoms in the graphene sheet plane in the Pd/G system mainly increases, and on further temperature rise, the mobility of these atoms along the normal to

this plane also increases. As the clusters are destroyed, the contact between the Pd and C atoms becomes closer, while the coefficient D_{xy} becomes more stable.[67,68,74] If the palladium atoms that are mobile at high temperature are located in a confined area (clusters), strong local impact on the graphene sheet takes place and, as a consequence, pronounced oscillations of the function $D_{xy}(T)$ of carbon atoms are observed.

It was shown [119] that heating up to 2300 K of the Cu/G_2 interface activates most appreciably vaporization of copper atoms and defragmentation of the metal subsystem. This is reflected in the two-stage character of the temperature dependences of diffusion coefficients of copper (see Fig. 22): the first noticeable increment is observed in the >500 K and 800–1200 K ranges for Cu/G and Cu/G_2, respectively, due to the onset of quasi-melting of the interfacial pseudophase, while the second increment is at 2000–2300 K at the stage of surface atom vaporization.

The destruction of the periodic metal structure (as the solid–liquid transition analogue) was accompanied by accumulation of most of copper atoms mainly in the central part of the graphene sheet, the major part of the atoms being assembled in a flat drop. This picture was observed at a lower temperature (1300 K) than the melting point of the bulk copper crystal. At 1300 K, the copper atoms were noticeably displaced also in the z direction ($0 < z$ and $z > 0$) without substantially moving away from the major material of the metal film or graphene sheet. It is at this temperature and in this state that the first penetrations of copper atoms to the other side of the graphene sheet were detected, and at 1800 K, vaporization events of single copper atoms were noted. The boiling point of the bulk liquid copper (2840 K) is more than 1000 K above this temperature. The copper atom vaporization and penetration to the other side of the graphene sheet substantially enhanced at 2300 K. However, at 2800 K, the distances between the copper atoms markedly decreased and simultaneously they were drawn closer to the carbon atoms of the adjacent surface. On further heating to 3300 K, the copper atom vaporization and penetration to the other side of the graphene sheet were again intensified.

In the bilayer graphene model, the copper atoms behaved in a different way. At 800 K, the fluctuations of distances between the carbon atoms in graphene were sufficient for their thermally activated diffusion through the adjacent layer, exit into the graphene–graphene interlayer space and formation of bonds with the carbon atoms in the sublayer. However, no diffusion of copper atoms beyond the surface of the second graphene layer was detected even upon long-term maintenance of the system at 3300 K, although the presence of the second graphene layer indirectly intensified the copper atom diffusion both in the xy plane and in the z direction upon weakening of the Cu–C bond (see Fig. 22). On heating to 1300 K, the mobility of copper atoms in the z direction was markedly higher when the atoms were located on the bilayer graphene than on the monolayer graphene. In the case of monolayer graphene, the maxima of the coefficients D_{by} and D_z fell on the temperature of 2300 K; while in the case of bilayer graphene, the highest D_{xy} corresponded to a temperature of 2800 K, while the highest D_z corresponded to 1300 K. The metal atoms that passed through the first layer were attracted by the second graphene layer and were removed from the first layer by a longer distance than in the case of monolayer graphene. However, even at 3300 K, the copper atoms did not penetrate the second graphene layer.

Owing to weaker Cu–C interactions, the thermally activated penetration of the metal atom across the interface occurs at a 200–300 K lower temperature for the Cu/G heterostructure than for the Pd/G and Ni/G heterostructures. Due to increasing fluctuations of graphene bond lengths (and, hence, the sizes of six-membered rings), the probability of more intense penetration of copper atoms, compared to Ni and Pd atoms, through the graphene lattice increases, the metal subsystem being retained as a whole entity as additional fairly strong bonds appear between the metal atoms located on both sides of the graphene sheet.

The anisotropy of atom migration in the graphene planes deserves attention. Indeed, the film dimension in the longitudinal direction of the bilayer graphene decreased more smoothly with temperature rise, while in the transverse direction it decreased less rapidly than in the case of monolayer graphene. At 3300 K, the contraction of the metal film in the longitudinal direction is more pronounced for the bilayer graphene, while in the transverse direction it is more pronounced for monolayer graphene.[119,164] The considerable enhancement of the temperature oscillations and the formation of voids in the 2D hexagonal lattice at 3400 K (Ref. 174) were interpreted in the MD model (using the Brenner potential [175]) as melting of the graphene nanoribbon. However, in another study,[176] MC calculations (using the LCBOPII potentials [177] and the 2D Lindemann criterion) gave a much higher value for the graphene melting point (4900 K). The Pd_{13} clusters with the fcc and random packings were already destroyed on heating in this temperature range. The Pd_{13}/G cluster having random packing proved to be least stable to temperature rise.

V.2.c. Binding energy

In the case of nickel–graphene systems with one-sided (Ni/G) and two-sided (Ni/G/Ni) arrangement of nickel clusters on a graphene sheet, the temperature dependences of the potential energies of interaction of nickel atoms (U_{Ni-Ni}), nickel and carbon atoms (U_{Ni-C}) and carbon atoms (U_{C-C}) (Fig. 24) reflected substantially stronger correlations of the Ni–C bonds, as has already been noted, in comparison with the Cu–C bonds. The decrease in the U_{Ni-Ni} values is already significant at 800 K in the Ni/G system, while in the Ni/G/Ni system it becomes significant only at 1300 K, which is caused by competition between metal atoms in both surfaces for rehybridization with the graphene carbon atoms. The specific partial volume energy of the metal was equal to the binding energy of the considered element, the experimental value of which for nickel at 300 K is -4.44 eV per atom.[178] The close value of U_{Ni-Ni} (-4.39 eV per atom) for a nickel fcc crystal was provided by MD calculation for the NPT ensemble† (see Ref. 179). The u_{Ni-Ni} energy of the Ni_{23} cluster calculated using the Sutton–Chen potential was -3.70 eV per atom.[180] The U_{Ni-Ni} value for the highly stretched Ni film was higher at the considered temperatures.

On further heating, the partial potential energy U_{Ni-Ni} increased, the increase being especially pronounced at

† N is the number of atoms at constant pressure and temperature.

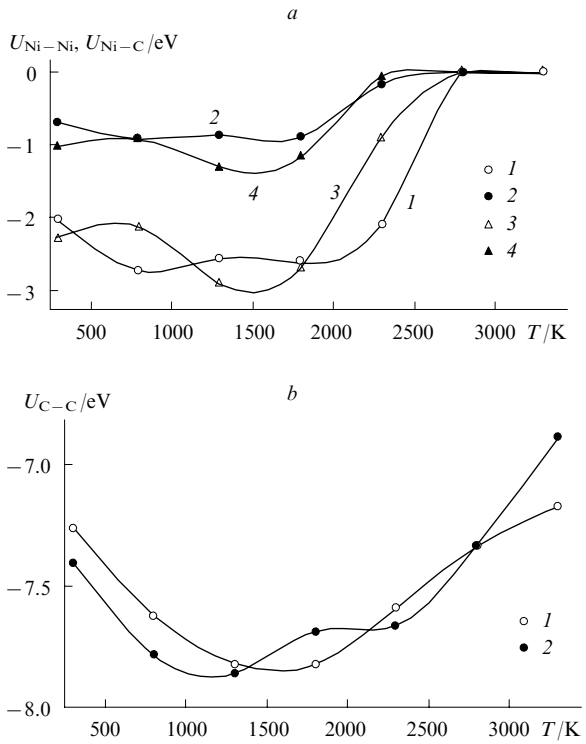


Figure 24. Temperature dependences of the partial potential energies U_{Ni-Ni} (*1*, *3*); U_{Ni-C} (*2*, *4*) (*a*) for the Ni/G (*1*, *2*) and Ni/G/Ni (*3*, *4*) systems and the energy U_{C-C} (*b*) for a free graphene sheet (*1*) and a graphene sheet coated by a Ni film on one or both sides (*2*).[164]

> 2300 K for the Ni/G system and at > 1800 K for the Ni/G/Ni system. The temperature dependence of U_{Ni-C} for both systems changed in approximately the same way, except that no decrease in U_{Ni-C} following the initial heating of the Ni/G system was detected. Only when the temperature of 1800 K was reached, the U_{Ni-C} energy in both systems increased. The potential energy for a neat graphene sheet (bearing no metal film) was minimal at 1800 K (see curve *1* in Fig. 24 *b*). Analysis of the temperature dependences of U_{C-C} for graphene in the presence of one or two Ni films demonstrated that they were fully identical (see curve *2* in Fig. 24 *b*).[164] In the region of $T \leqslant 1300$ K, the presence of a transition metal stabilized the structure of the graphene sheet, so that the energy U_{C-C} decreased as compared with the energy of isolated graphene. This result is in line with the data of Song and Zha,[181] who demonstrated a decrease in the stresses in graphene after deposition of the Ni film. The decrease in the energies U_{Ni-Ni} and U_{C-C} upon contact of a graphene sheet with a nickel surface (including nickel cluster) is attributable to the considerable attractive interaction between them.[182] Only at temperatures of > 1300 K, was an increase in the potential energy detected. The increase in the graphene energy above 1300 K was faster in the presence of metal atoms than without these atoms. The U_{C-C} value at 3300 K for the Ni/G and Ni/ G/Ni systems was ~4% greater than for a neat graphene sheet.

V.2.d. Stress tensors

The shear stress that acts on atom *i* located on the (111) surface of the metal was determined by the tensor[183]

$$\sigma_{\alpha\beta}(i) = \frac{\varepsilon}{2a^2\Omega_i}\sum_{i\neq j}^{k}\left[-n\left(\frac{a}{r_{ij}}\right)^{n+2} + mc\left(\frac{1}{\sqrt{\rho_i}}+\frac{1}{\sqrt{\rho_j}}\right)\left(\frac{a}{r_{ij}}\right)^{m+2}\right] r_{ij}^{\alpha} r_{ij}^{\beta}$$

where ε is a parameter with the dimensionality of energy, a is a parameter with the dimensionality of length, which is usually chosen to be equal to the lattice constant; the volume of single atom Ω_i can be associated with the Voronoy polyhedron volume; m and n are positive integers, where $n > m$; and c is a dimensionless parameter,

$$\rho_i = \sum_{i\neq j}\left(\frac{a}{r_{ij}}\right)^{m}$$

The temperature dependences of the tensor components for monolayer graphene have complex patterns. For the

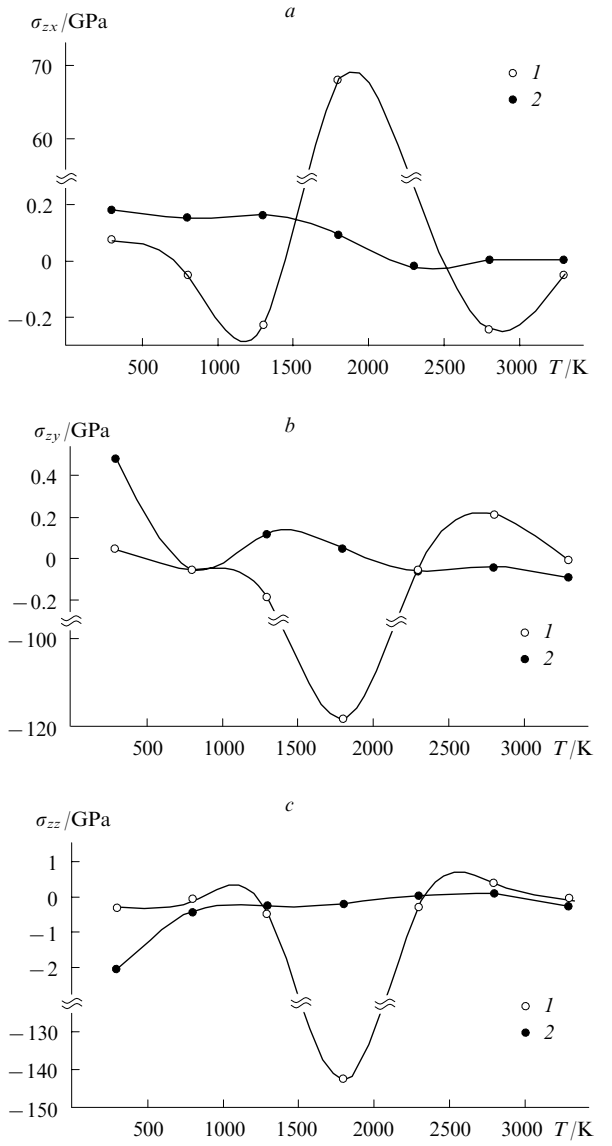


Figure 25. Temperature dependences of the stress tensor components σ_{zx} (*a*), σ_{zy} (*b*) and σ_{zz} (*c*) for copper films.[119]
(*1*) Cu/G system, (*2*) Cu/G_2 system.

Cu/G and Cu/G_2 systems, the temperature dependences of the stress tensor components σ_{zx}, σ_{zy} and σ_{zz} are appreciably different (Fig. 25). A common feature of these dependences is the presence of extrema at 1800 K. At other temperatures, the stress components for the Cu/G and Cu/G_2 systems were commensurable;[119] furthermore, at the highest temperature of 3300 K, the difference between the like components of the mentioned systems is noticeably smaller than that at the minimum temperature (300 K).

Analysis of the results of the temperature stress relaxation in the Ni/G and Ni/G/Ni systems (Fig. 26) demonstrated that the σ_{zx}, σ_{zy} and σ_{zz} stresses decreased with temperature rise.[164] For the Ni/G system, weak actions on the metal atoms were detected (the greatest of them cause the stresses σ_{zz}). The strong interaction of the nickel surfaces with graphene in the Ni/G/Ni system induced the development of substantial stresses in the metal planes. The magnitudes of the stresses acting in the *xy* plane were always greater for the lower Ni film than for the upper one, which is due to the smaller thermal stability of the lower film caused by great fluctuation displacements of atoms in the upper film. The initial minimal distance between the nickel atoms in different layers was almost 2.7 times greater than the distance between the closest neighbours in the bulk metal. Even at the initial temperature of 300 K, the stresses σ_{zz} were negative for both the upper and the lower metal films, as a result of substantial drawing together of atoms at the boundary between the metal and graphene separating two nickel films. The positive value of σ_{zz} at 300 K for the Ni/G system indicates that the attraction of nickel atoms to the graphene sheet is rather weak, *i.e.*, the nickel atoms are bound to a lesser extent. Up to 1800 K, slight reduction of film dimensions was observed for both systems (Ni/G and Ni/G/Ni) due to the initially applied tensile strain. Thus, the effects revealed in the analysis of temperature dependences of the stress tensor components are mainly due to the incommensurability of the lattice parameters of the metal films and graphene.[74, 119, 164]

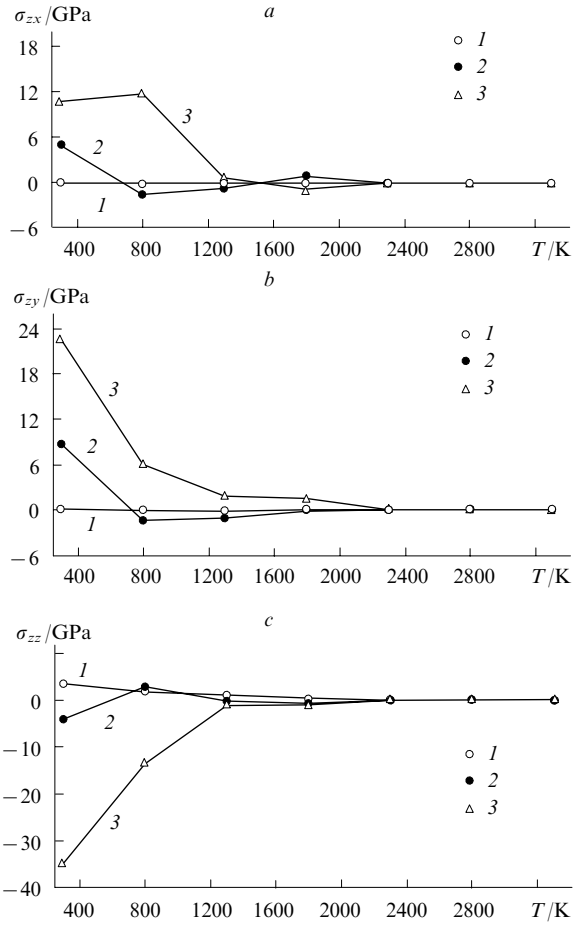


Figure 26. Temperature dependences of the stress tensor components σ_{zx} (*a*), σ_{zy} (*b*) and σ_{zz} (*c*) for nickel films.[164]
(*1*) Ni/G system; Ni/G/Ni system: (*2*) Ni is above, (*3*) Ni is below.

It should be specially emphasized that, unlike the Cu/G, Ni/G and Pd/G systems, in the model Cu/G_2 bilayer graphene system, the horizontal diffusion of copper atoms (D_{xy}) at temperatures of > 1500 K develops more intensively than the vertical diffusion (D_z).[119] This is attributable to the fact that the temperature dependences of the deformation stress tensor components for the Cu/G and Cu/G_2 systems are fundamentally different: the contact of a metal surface with monolayer graphene at >1800 K gives rise to a sharp extremum in the dependences of these components, which may be caused by the increasing amplitudes of the deformations (up to the 'island' fluctuations with partial defragmentation of the closed packing of the metal).

V.2.e. The Pd_N/G clusters (N = 13, 561)

Within the framework of computer simulation, the thermal evolution of Pd_{13} clusters with different initial structures (fcc, Ih, rcp) attached to a graphene substrate (Pd/G) was analyzed (Fig. 27).[67, 74, 152] Since the effects of rehybridization in the Cu/G, Ni/G and Pd/G systems were different, the scales of formation of tetrahedral coordinations in different systems had their own distinctive features.

The diffusing palladium atoms, upon interaction with graphene carbon atoms, form two-dimensional ring structures — ring clusters (as in the case of Cu/G and Ni/G interfaces).[67, 74] They are constructed of graphene unit cells (with the lattice parameters a_G = 0.246 and 0.492 nm) with a shift and arrangement of either four carbon atoms around one central metal atom (as in the case of Ni, Co, Cu) or (as in the case of Pd, Pt, Au, Ag and Al) eight atoms of carbon superlattice around three central metal atoms. For the Pd_{13} fcc cluster, as for the Pd_{561} fcc cluster with the initial Ih structure (Fig. 28 *a*), on heating to 1300 K (Fig. 28 *b*), superlattice points are formed in the of Pd/G contact areas (Fig. 28 *c*) by three carbon atoms of the first and three more carbon atoms of the second coordination around single palladium atoms that have been inserted into the graphene plane.[67] The most pronounced change in the palladium coordination upon temperature rise was noted for the Pd_{13} fcc cluster (see Fig. 27 *b*).

The diversity of structure transformations can be interpreted taking into account the difference between the interaction energies of metal and carbon atoms.[184, 185] Indeed, the lowest Pd–C interaction energies were noted for the system that forms the interface between graphene and Pd_{13} fcc clusters (Fig. 29). The lowest Pd–Pd binding energy was inherent in the Pd_{13} Ih clusters; therefore, they underwent the least structure changes, which is interpreted as the energy autonomy effect. Only for these clusters, the binding energy with graphene changed little up to 4000 K.

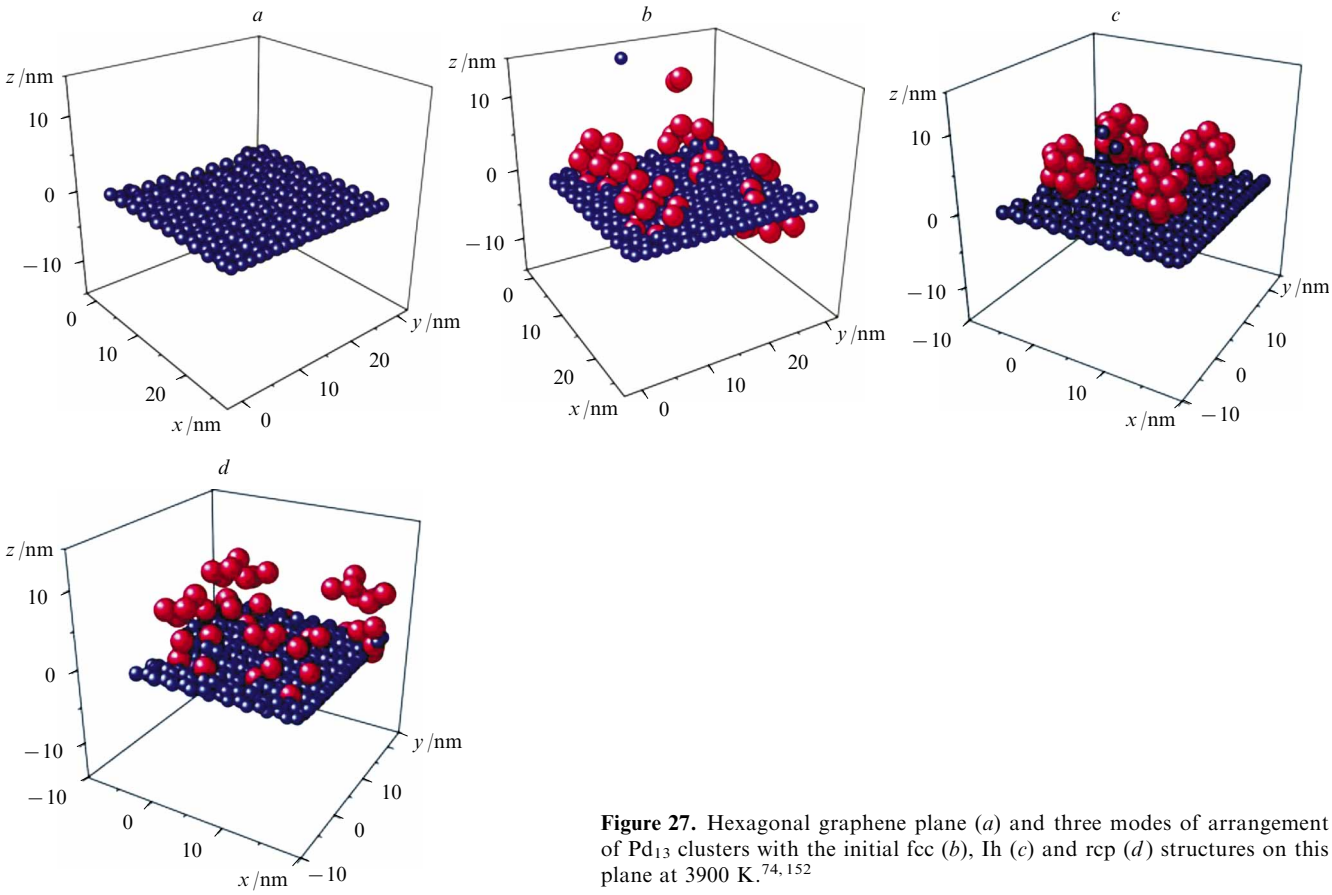


Figure 27. Hexagonal graphene plane (*a*) and three modes of arrangement of Pd_{13} clusters with the initial fcc (*b*), Ih (*c*) and rcp (*d*) structures on this plane at 3900 K.[74, 152]

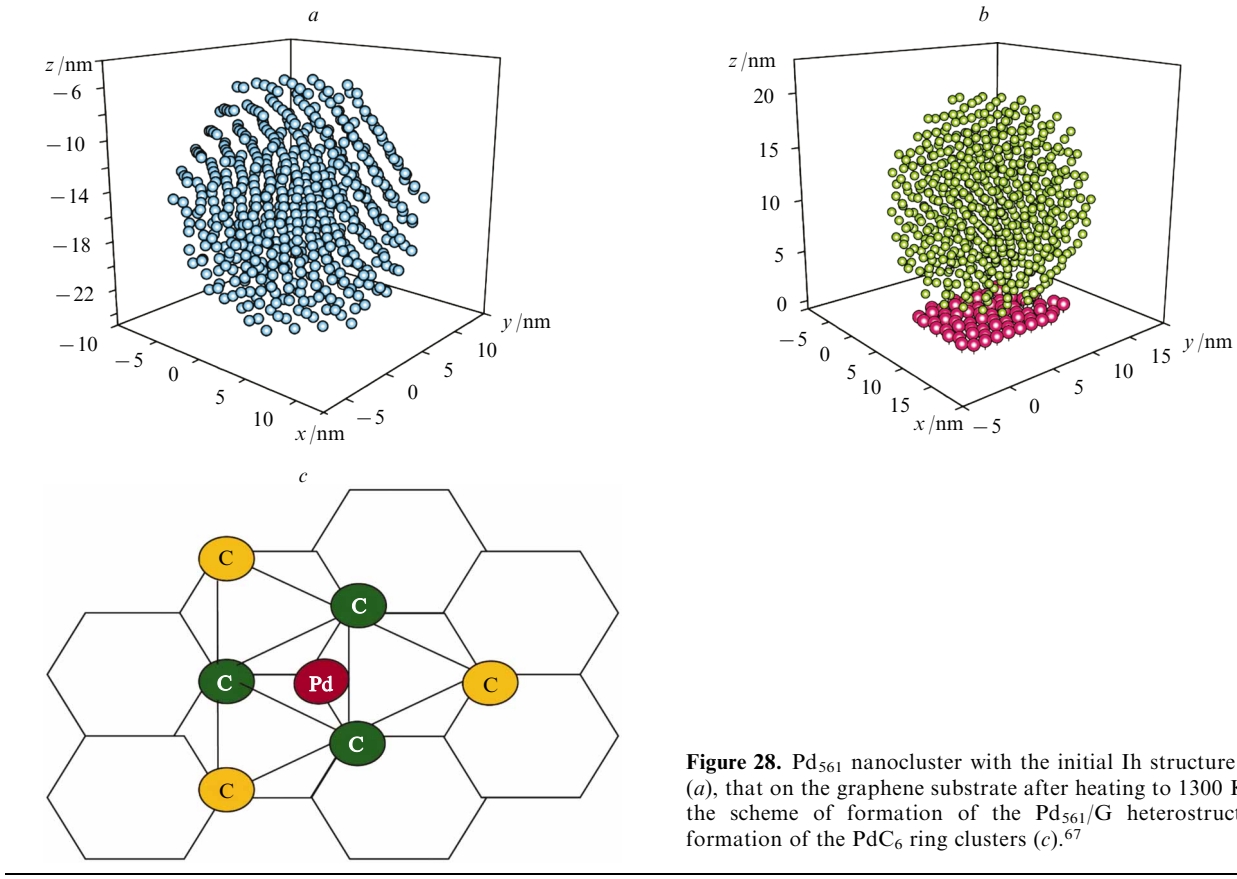


Figure 28. Pd_{561} nanocluster with the initial Ih structure at 300 K (*a*), that on the graphene substrate after heating to 1300 K (*b*), and the scheme of formation of the Pd_{561}/G heterostructure with formation of the PdC_6 ring clusters (*c*).[67]

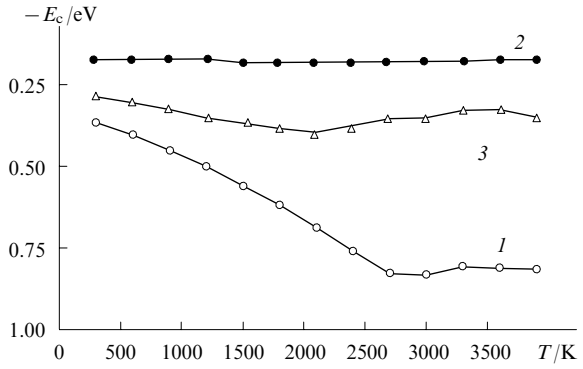


Figure 29. Temperature dependences of the Pd–C interaction energy for the Pd_{13}/G systems with the fcc (*1*), Ih (*2*) and rcp (*3*) cluster structures.[67, 152]

The structures of the Pd_{13} clusters having other types of atomic packings were destroyed under these conditions; randomly packed clusters were least stable: their initial coordinations were completely destroyed under the action of carbon atoms at 3900 K to give mainly Pd–C bonds.

The specific features of atomic dynamics and interaction of Pd clusters with the substrate can be derived from the above analysis of the coefficients D_{xy} and D_z (see Fig. 21). The clusters with the Ih structure either present initially or having appeared after isomerization and transformation of unstable (100) and (110) faces proved to be most stable on heating. Despite the fluidization induced by heating-initiated diffusion of surface shell atoms, the contours of the faceted morphology of clusters were retained but gradually smeared up to complete melting of all shells. The interaction with the graphene substrate changed considerably the heating thermodynamics and the kinetics of cluster 'melting'. This is even more obvious if the clusters are intercalated into a nanotube or are surrounded by a fullerene-like shell.[145, 146]

The character of binding and specific atomic dynamics clarify the thermal evolution of endohedral clusters. Indeed, in the case of physically adsorbed interface of an endohedral copper cluster with relatively low Cu–C binding energy at a temperature 15–20 K higher than the melting point of bulk samples, pressure build-up and, hence, increase in the kinetic energy (k_BT) of copper atoms boost the probability that some of these atoms would migrate beyond the surface of the fullerene-like shell (as through the graphene sheet[119]) with retention of its integrity. In the case of chemisorbed interfaces of endohedral M@C_n clusters with high energy of hybridized bonds, heating above the melting point would induce deformation stresses in the interface followed by stress relaxation accompanied by bond recoordination in graphene, increase in the fraction of M–C bonds and the volume of the endohedral sphere as well as by the formation of a bond network similar to the bond network formed in metcars (*e.g.*, in Ti_8C_{12}). Further heating and increase in the atomic energy to values comparable with the activation energy for metal atom vaporization and increase in the excessive density of bonds of different type would inevitably cause destabilization and destruction of the endohedral structure.[145]

As a Pd_{561} cluster was heated and 'melted' on a graphene substrate, the pattern of temperature dependence of the phonon contribution to the specific heat capacity C_V changed. This contribution can be estimated by integrating, from 0 to ∞, the spectrum of vibration frequencies (ω) of cluster atoms $D(\omega)$ as the Fourier image of autocorrelation functions of atom velocities $v_i(t_0+n\Delta t)$, where n is the number of time steps Δt. In the one-phonon approximation[8, 10]

$$C_V = \frac{3N\int f(\omega)D(\omega)\mathrm{d}(\omega)}{\int D(\omega)\mathrm{d}(\omega)}$$

where $f(\omega)$ is the quantum oscillator statistical function

$$f(\omega) = k_B\left(\frac{\hbar\omega}{k_BT}\right)^2\frac{\exp(\hbar\omega/k_BT)}{[\exp(\hbar\omega/k_BT)-1]^2}$$

The electronic contribution is determined *via* the electron density states at the Fermi level [$N(E_F)$] and is also temperature-dependent

$$C_e = \frac{\pi^2k_BTN(E_F)}{3}$$

If the frequency spectrum is known, it is possible to estimate the diffusion coefficient, which is proportional to the value of the spectrum at zero frequency. However, in MD calculations, it is preferable to estimate diffusion *via* the root-mean-square displacement and to estimate the specific heat capacity C_V *via* the root-mean-square fluctuations of the kinetic (temperature) or internal (potential) energy

$$C_V = \frac{\langle U^2\rangle - \langle U\rangle^2}{Nk_BT^2} \qquad (2)$$

(here N is the number of atoms in the cluster).

The temperature variations of thermodynamic values such as internal energy (caloric curve for the potential energy per atom) and the heat capacity C_V appear equally demonstrative for the thermal size effects and the substrate effect. Note that the non-monotonic temperature dependence of the caloric curve reflects to a larger extent the complex structure transformation processes and states of clusters than the gradual decrease in, for example, shear moduli.

The energy redistribution with increase in the surface component leads to non-additivity of thermodynamic components, which is especially pronounced in the character of the temperature dependence of the heat capacity C_V calculated by relation (2) for an isolated Pd_{561} nanocluster heated from 300 to 1500 K. From the initial stage of heating to the completion of quasi-melting and onset of intense melting of all shells, the heat capacity changes are exceptionally non-uniform.

Under the action of even slight heating or upon weak interaction between metal atoms and graphene, rearrangement of metal atom coordinations takes place in the contact area, which affects the curve $C_V(T)$ of the cluster. The Cu/G and Pd/G systems differ substantially in the degree of hybridization; in view of the stronger Pd–C interactions, it is natural to expect that this would affect the temperature dependences of the heat capacities of these systems (Fig. 30); in particular, the Cu/G system does not show the well-resolved peak on the right from the major peak.

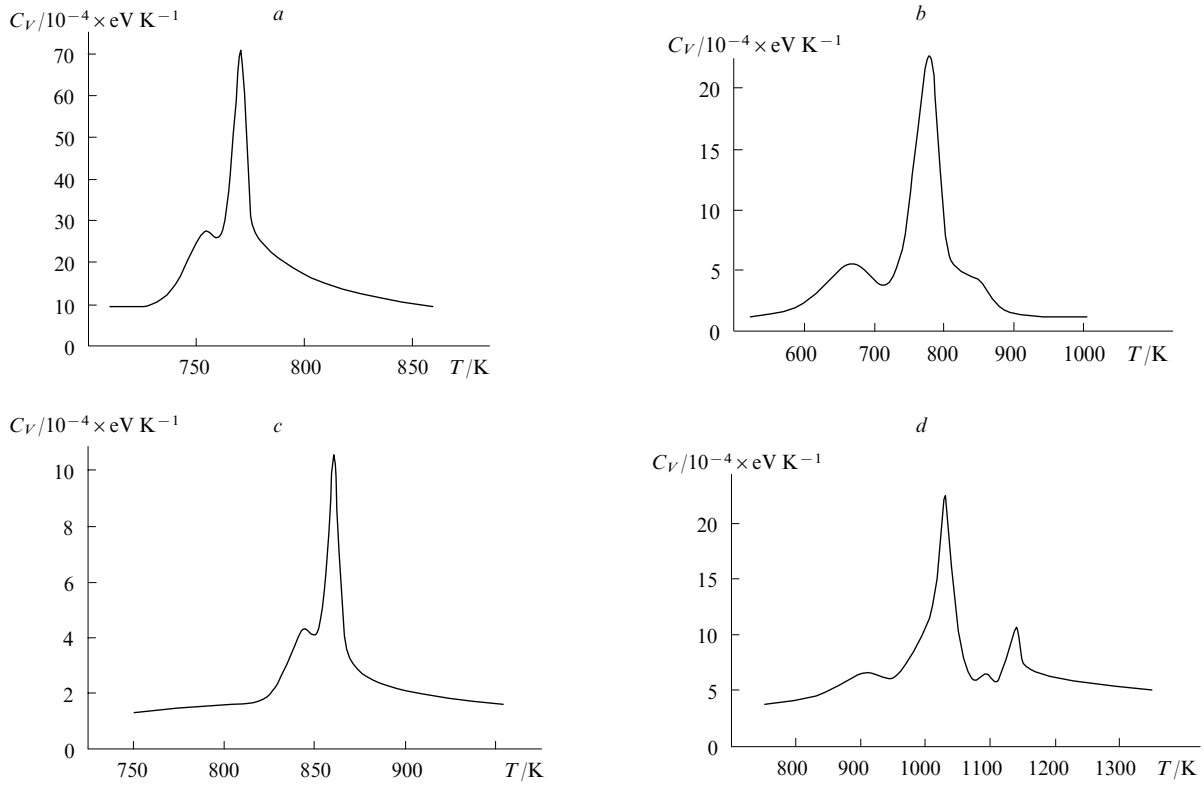


Figure 30. Temperature dependences of the heat capacity C_V on heating from 300 to 1300 K of Cu_{50} (*a*, *c*)[119] and Pd_{561} (*b*, *d*)[74] clusters with the initial fcc and Ih structures, respectively; (*a*, *b*) isolated clusters; (*c*, *d*) clusters on a graphene substrate.

On hardening on the graphene substrate, the structure of Pd_{561} nanoclusters comprising five shells was not the same as the structures of isolated clusters or bulk samples. On the nanoscale, the structure changed from Ih to hcp during various stages of heating and hardening.[186–188] For Ni_{561} on a graphene substrate, a fcc rather than icosahedral structure proved to be most stable from the energy standpoint.

The specific features of interaction of the island films of nickel[164] and palladium clusters[74, 152] with the substrate can be followed from temperature dependences of components of the kinetic coefficients D_{xy} and D_z (see Figs 21–23). It has been noted above that even a slight heating and weak interaction between the metal and carbon atoms induce a mutual rearrangement of metal atom coordinations to give a substructure (moiré) upon superposition of the metal and graphene lattices with incommensurable parameters. As tetrahedral coordinations with incorporation of metal atoms are formed, a contact sphalerite structure appears in which local coordinations can be represented as carbon ring clusters centred at the hcp points or triangular fcc points (with groups of three carbon atoms around the substrate atoms). Recoordination occurred also in a graphene monolayer on heating to 900 K and a relative compression of > 0.4 in the 'zigzag' direction (the Lennard-Jones potential was additionally introduced in the calculations to damp the dynamics of carbon atoms in each hexagonal unit in order to avoid the wave-like corrugation of the graphene plane).[74, 119, 164]

A possible method for stabilization of the diffusion processes at the interface activated by the parametric incommensurability is doping of metal films by deliberately chosen metal atoms. For, example, manganese atoms can initiate restructuring processes to form Mn–M–Mn chains, which not only induce local changes in the interatomic distances (with increase in the contact area by $\sim 1\%$) but also generate a network of randomly oriented local stresses,[189–193] which prevent atom migration. The stabilization energy can be estimated using the formalism that takes into account three factors:[190] the structure disorder, the activation interactions related to phonon transport and impurity migration. Using the MC and MD techniques it is possible to estimate the effect of doping elements (in particular, manganese) by calculating the decrease in the incommensurability potential, which activates the diffusion mobility of atoms.[191, 192] Naturally, the doping elements would also change the electronic spectrum of the interface, namely, additional levels would appear in the band gap.[189, 190]

V.3. Catalysis models

The thermal evolution of transition metal clusters attached to a graphite substrate was analyzed.[194, 195] The thermal stability of catalysts comprising platinum nanoclusters supported on graphite in the region of 200–1700 K was studied as a function of size (clusters composed of 256 to 1372 atoms were considered). The temperature of destruction of the cubic structure (analogue of melting) markedly increased with increase in the number of atoms in the nanocluster: from 850 K at $N = 256$ to 1100 K at $N \approx 1400$.

Molecular dynamics simulation[124, 195] of the thermal growth of the single-walled carbon nanotubes catalyzed by

nickel nanoclusters of various shapes and morphologies was carried out starting from nucleation and formation of the cap covering the nanotube end up to the formation of an extended cylindrical body up to 10 nm long.

The processes that can occur with high probability during a real transition metal-catalyzed synthesis of nanotubes from the carbon vapour phase formed upon laser ablation were reproduced.[196–199] The initial stage of nucleation and nanotube growth was distinguished and its duration was determined (~150 ps). This stage started with the adhesion of separate atoms and terminal chains consisting of several carbon atoms from the vapour phase or penetration of these atoms into the outer shell of the nickel cluster followed by formation of graphene networks on the cluster surface. The following question remains open: how important for the intensity of synthesis is the initial supersaturation of the vapour–gas phase with carbon? The supersaturation is a short-term phenomenon (in view of the high rate of the process) difficult for experimental or computer investigations. After a period of 2860 ps, the step of tube cap formation ended and the formation of the cylindrical walls started. By varying the substrate, it is possible to enhance its interaction with the cluster atoms and control its thermal stability, thus considerably increasing the melting point. As >10% of the cluster surface atoms have been attached, the melting point in the contact zone sharply increases and the strongly acting bonds in this zone affect the atoms of adjacent layers.

To study the substrate effect on the electron charge distribution on the cluster surface and conditions for the appearance of tunnelling current in the system of 2D spacers, it is necessary to utilize other quantum statistical methods for estimation of electron states. From known geometry of the possible overlap of the long-range electron density profiles, one can estimate the distances between the nanoclusters without allowance for the quantum mutual effects of electron densities. To intensify a chemical reaction at high density of catalytic sites with a specifically changed local electronic structure, conditions are necessary for the most low-energy electron (or proton) transfer between the adsorbed reactant molecules and a nearby catalytic site. The most active sites are formed upon the overlap of oscillating electron density profiles, which is sufficient to provide for tunnelling current.

The electronic 'long-range action'[4,5] within 1 nm, depending on the Fermi wave vector, ensures the required overlap even at distances of $r = 1.7–2.0$ nm with a nanocontact tunnelling conduction determined by the probability that is proportional to the exponent $\exp[-2r(2\varphi)^{1/2}]$ (φ is the electron work function, which is much greater than the electric potential of the nanocontact).

It should be taken into account that the maximal activity of nano-sized clusters can be associated with a change in the conduction of the immobilizer material, which can thus acquire a semiconductor behaviour as a result of electron density redistribution throughout the whole catalytic assembly. This redistribution would actually enhance the catalytic activity at a certain (optimal) number of atoms in the nanocluster, while in the presence of a fraction of larger clusters, it would not have the desired effect.[3] Evidently, the appearance of additional charge on active sites should enhance the efficiency of the catalysis.

In the nickel and palladium nanoparticle assemblies with the size comparable with the critical value (~2 nm), non-activated electron transfer mechanism is implemented even at a moderate packing density. The average conductivity of this assembly actually depends not only on the nanocluster size and shape but also on the nanocluster mutual positions and packing density. As the packing density factor increases, nanoparticle assemblies forming extended structures may switch from the tunnelling thermally activated conduction to a metallic conduction (up to superconductivity). For instance, a monolayer coating of copper nanoparticles may change the conductivity of the resulting film by nine orders of magnitude.[76,200] Thus, apart from the influence on the general surface topology and internal structure, the electronic and charge state of the substrate determines the cluster self-assembly processes by participating in their cooperative interaction and electron density redistribution, and, finally, affects the catalytic activity.

V.4. The interface in the Ag/SiO_2 system

Even the first studies of catalysis by deposition of transition metal nanoclusters on oxides demonstrated[200–203] that the size effect with a high degree of regio-, stereo- and nanoselectivity in chemical transformations accompanied by low energy expenditures but having unexpected efficiency would give the key for controlling other chemical processes that have been considered impossible. Silver is widely used in photography and catalysis; it is also demanded in the manufacture of new optoelectronic devices.[204] Silica nanoparticles coated by a 15–20 nm silver layer or by gold exhibit a therapeutic effect in tumour treatment.[205–207] Such a nanoparticle is able to convert the absorbed IR radiation energy into thermal energy and induce cell destruction. Experimental studies of the behaviour of $(Au)_i(SiO_2)_n$ nanoparticles demonstrated that their optical response is caused by hybridization of plasmons of the inner and outer shells.[208] A study[209] of binding of gold atoms to small silica clusters demonstrated that this system may have the same therapeutic effect on tumours as larger nanoparticles. The adsorption of silver on the surface of the α-SiO_2 cluster enhanced the Raman effect.

Galashev and Polukhin[201] performed MD calculations for the adsorption of silver atoms on a α-SiO_2 surface and formation of the cluster/island Ag/α-SiO_2 interface. The absorption and transmission IR spectra, Raman spectra and the numbers of IR-active electrons were calculated. The major effect of the attachment of silver atoms to a silica cluster is the considerable increase in the thermal emission power. The electronic properties of $Ag(SiO_2)_n$ small clusters, where $n = 1–7$, were studied by the density functional theory.[210] In the researchers' opinion,[210] these clusters could serve as an alternative to more expensive $(Au)_i(SiO_2)_n$ systems with $n = 1–7$, as they have the same functional properties. The interaction of atoms in the SiO_2 group of $Ag(SiO_2)_n$ was represented by the Coulomb and Morse potentials.[211]

The interaction between silver atoms can be described by a different potential the parameters of which have also been reported (see Ref. 212). The Si–Ag and O–Ag atom–atom interactions were estimated based on the parametrized Lennard-Jones potential.[213] In the calculation of molecular interactions, bond flexibility should be taken into account by using the deliberately developed procedure in terms of Hamiltonian dynamics.[214]

The initial packing of SiO_4 tetrahedra representing a quartz nanoparticle $(SiO_2)_{50}$ with isolated structural units was obtained using GRINSP software.[215] The positions of silver atoms were determined using a virtual fcc lattice piercing the $(SiO_2)_{50}$ cluster. The lattice constant was 0.6 nm. The lattice points most proximate to the silica nanoparticle occupied by silver atoms were spaced by not more than 0.6 nm from each silicon or oxygen atom. Three calculations were accomplished for different numbers of silver atoms ($N_{Ag} = 10$, 30 and 50) surrounding the $(SiO_2)_{50}$ nanoparticle. Examples of some elementary cluster configurations (Fig. 31) with ring groups of adsorbed Ag_n clusters ($n = 2-7$) on the α-SiO surface were reported.[216]

Examination of the $Ag_{50}(SiO_2)_{50}$ structure formed in 250 ps (Fig. 32) demonstrated that the interaction of silicon dioxide with silver atoms does not prevent the aggregation of SiO_2 islands, the spheroid cluster shape being retained. The silver atoms are in close contact with silicon and oxygen

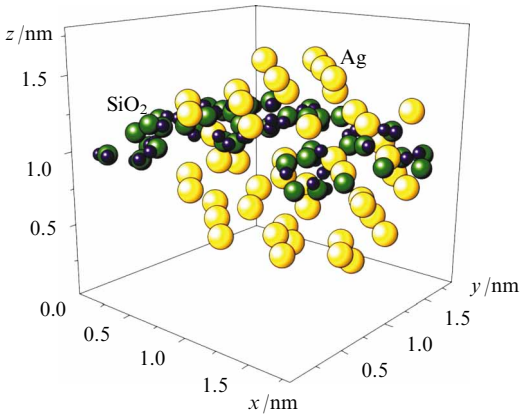


Figure 32. Configuration of a $Ag_{50}(SiO_2)_{50}$ nanoparticle formed at 300 K in 250 ps.[201]

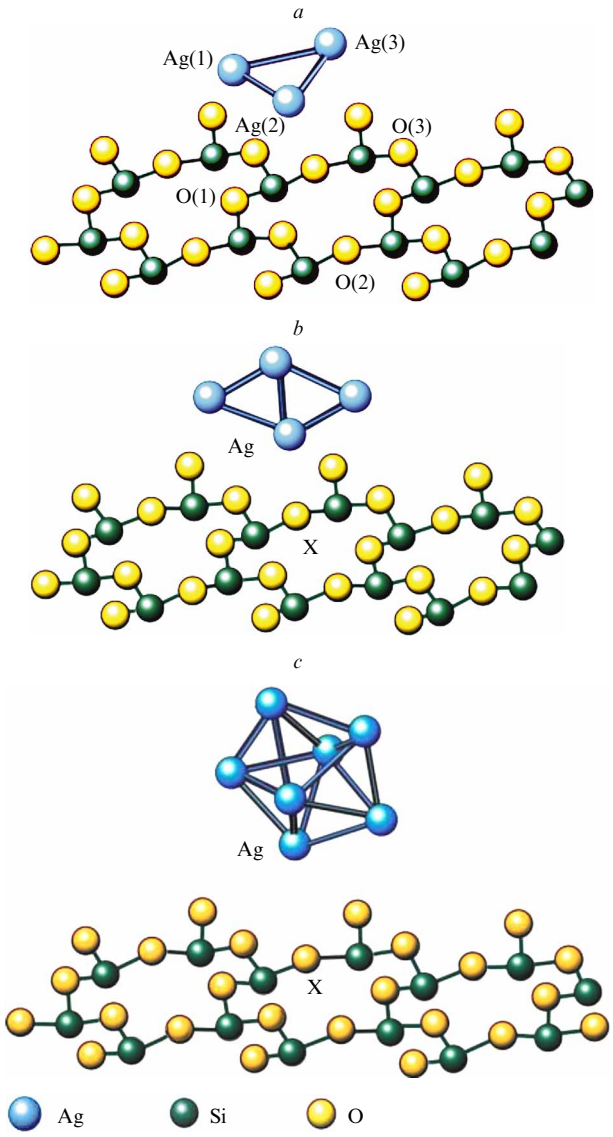


Figure 31. Examples of some elementary configurations from the adsorbed Ag_n clusters ($n = 2-7$) on the α-SiO surface.[216]
The crosses mark the centres of the SiO rings.

atoms, as they fill the gaps between the SiO_2 structural units. The inner part of a silver cluster contacting with SiO_2 islands is disordered. However, the crystal order inherited from the initial fcc lattice of silver can be followed at the periphery. The observed structural relaxation is mainly associated with migration of lighter and more mobile SiO_2 groups.

The integral intensity of the Raman spectrum (Fig. 33) for the considered model decreases as more silver atoms are attached to $(SiO_2)_{50}$. The integral intensities of systems I–IV obey the ratio: 1 : 0.81 : 0.56 : 0.34. The location of the first peak (with a 87 cm^{-1} frequency) does not change, and the diffuse second peak shifts to higher frequency. The experimental Raman spectrum of α-quartz[217] has four peaks in the frequency range from 100 to 500 cm^{-1}, the major peak being at 467 cm^{-1}.

The dependence of the number of electrons (N_e) involved in the interaction with IR radiation on the number of silver atoms in the cluster (i) has a maximum at $i = 30$

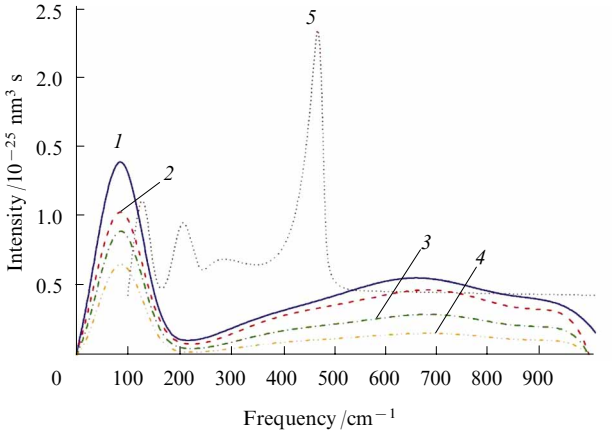


Figure 33. Raman spectra for the systems formed by a self-assembled cluster from $(SiO_2)_{50}$ particles and adsorbed silver atoms.[201]
(*1–4*) Calculation for systems I–IV containing 0, 10, 30 and 50 silver atoms, respectively, on a α-SiO_2 nanoparticle; (*5*) experimental Raman spectrum[217] of α-quartz at 300 K.

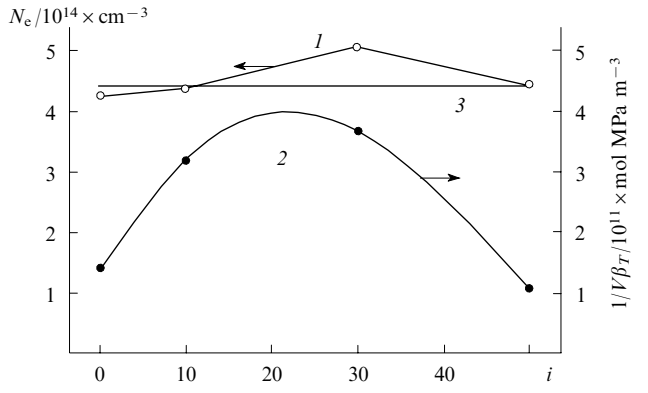


Figure 34. Number of electrons interacting with external electromagnetic radiation (*1*), mechanical stability factors $1/V\beta_T$ (*2*) for the $Ag_i(SiO_2)_{50}$ clusters and α-quartz (*3*) *vs.* the number of silver atoms.[201]

(curve *1* in Fig. 34). The N_e value for the cluster of thirty silver atoms is 1.6 times higher than that for the $(SiO_2)_{50}$ cluster. The silica cluster containing 30 silver atoms is also most stable according to the mechanical criterion of stability $1/V\beta_T > 0$, where V is the volume, β_T is the isothermal compressibility coefficient of the cluster (the method for calculating this value has been reported [115]). The stability factor $1/V\beta_T$ for the $Ag_i(SiO_2)_{50}$ clusters in question has a dome of stability at $i = 15-30$ (see curve *2* in Fig. 34). The $1/V\beta_T$ values for the clusters are lower than that for α-quartz (see curves *2* and *3* in Fig. 34).

Thus, the deposition of silver atoms on a silica cluster does not induce an increase in the absorption coefficient of IR radiation but decreases the intensity of Raman spectra and substantially enhances the power of heat radiation emitted by the clusters; also, the number of IR-active electrons increases and, at a moderate number of absorbed silver atoms, the mechanical stability of the cluster increases. Owing to high heat conductivity of silver, effective transfer of the emitted energy to the objects contacting with the clusters is expected.

VI. Stability and thermal size effects of silicon clusters determined by the specific character of covalent bonds

Clusters with a different character of interatomic bonds, namely, silicon clusters with covalent bonds were examined for comparison with the evolution of metal clusters. These clusters are a sort of semiconductor materials and important functional elements in opto- and nanoelectronics (nanoparticles including crystallites and nanoclusters are demanded in the manufacture of microchips). Semiconductor clusters with covalent bonds are synthesized at a low vapour pressure under the strict control over physicochemical properties, which depend on the change in the chemical composition, energy dissipation, vaporization and atom-and-molecular transformations occuring over picosecond time periods.

Extensive studies were mainly carried out for hydrogenated silicon clusters with up to 45 silicon atoms;[11,218–222] the $S_NH_x^-$ ($N \leqslant 44$)[221,222] and $Si_{10}H_x^+$ ions [223,224] were detected, quantum statistical stability estimates for the hydrides $Si_NH_x^+$ and $Si_NH_x^-$ were performed [220,225] and computer simulation of the thermal evolution of diamond-like fragments of the clusters was carried out.[226] It was found experimentally that upon formation of Si_NH_x nanoclusters in porous silicon, the silicon acquires photoluminescent properties.[227,228] It was also shown [228] that temperature rise induces dehydrogenation of the Si_NH_x nanoclusters down to the minimum hydrogen content — from $x = 28$ at 301 K to $x = 8$ at 943 K; stoichiometric clusters are very thermally stable.

Currently, research into silicon clusters comprising 60 atoms and more, *i.e.*, fullerene analogues, is topical, in view of the fact that silicon and carbon are neighbours in Group IV of the Periodic Table.[11,229] The optimistic view concerning the possible synthesis of these silicon clusters is related to the experimentally detected [230] and theoretically confirmed [231] the presence of five-membered rings in amorphous silicon.

Silicon nanoparticles of up to 50 nm size are transparent for light up to UV range and upon deposition of these particles (up to 10 nm-thick layer) onto light-absorbing surfaces of solar cells, the efficiency of the cells increases due to the ultraviolet re-emission effect. This result is impressive in view of the considerable researchers' effort aimed at increasing the efficiency of such devices by at least 1%. An equally noteworthy effect is observed if spherical silicon nanoparticles coated by a shell of inert triplet oxygen atoms are illuminated by a laser beam: oxygen converts from the triplet to singlet state and becomes a very potent oxidant. Being surrounded by malignant cells, such a cluster can accumulate light energy upon laser irradiation and burn out the cells. Nanofragments with a graphene monolayer packing composed of carbon and silicon atoms formed on metal nitride substrates can serve to create an element base of transistors/switches with a high degree of miniaturization.[5–11]

The physical well adjusted the model, which directly depends on the appropriately selected interaction potential, and the high accuracy of calculations not only help to understand the essence of the phenomena being studied but also open up the possibility to predict particular effects. It is this approach that provided the design, over shortest periods since the discovery of carbon nanotubes and fullerenes, of unique dislocation-free nanocrystalline silicon phases and various Si nanostructures of 5 to 60 nm size — spherical assembled ligands with oxygen or hydrogen outer shells, onions, nanotubes (hollow, intercalated or having outer shells) and pea pods hundreds of nanometres long. The nanostructured silicon phases are formed upon varying the temperature and the cooling rate of the argon plasma with silicon pre-injected into it at 6000 °C in the presence of transition metal atoms.[9,49]

The sizes of clusters used in optoelectronics occur in the range in which quantum effects influence the electronic properties. The nano-sized materials for microelectronics are subject to stringent requirements for purity, size and perfection of shape of the clusters as functional elements. A considerable portion of the fractional composition in the vapour–gas condensation processes are small particles, which rapidly coagulate. The size of primary spherical particles and the degree of agglomeration of the ultradispersed fraction depend on the ratio between the durations of particle collision and coalescence processes. Coalescence predominates if the time of processes limiting its

rate exceeds the characteristic period between the collisions. The variation of the ratio between these time periods provides for the control of the nanoparticle morphology and size required by the technology regulations. Practically, the particle size is controlled either by varying the characteristic time between the collisions upon change in the particle concentration in the flow or by varying the characteristic time of coalescence. Further progress in the studies of the mechanisms of increasing the thermal stability of such devices can be achieved by experimental studies and computer simulation of phase transitions in nano-sized systems.[49, 229]

The models are based on the data on electronic structures and nature of interatomic interactions obtained by computational MD and MC methods. These methods make it possible to simulate the changes in the structure and chemical composition of various composites. For instance, the MD calculations that use the density functional theory method and the electronic structure theory demonstrated the ability of silicon drops comprising 274 to 323 atoms to form distorted icosahedral structures on cooling. Computer simulation can be used for predicting the structure and properties of new non-crystalline materials for improvement of the production processes. The simulation showed that in the case of free boundaries, the silicon nanostructures composed of 20 slightly distorted face-sharing tetrahedra are unstable but upon assembly into a dense extended structure, they can form a slowly relaxing irregular solid medium, *viz*., glass.[9]

The influence of hydrogenation on the optical and electronic properties of semiconductors in different states receives increased attention,[232] especially in the development of functional nano-sized components of new technical equipment[233] (in particular, for the design of high-speed and compact chromatographs for separation and rapid analysis of multicomponent gas mixtures, polymer membranes for the production of non-traditional fuels, *viz*., gaseous hydrogen and methanol).[234, 235] The necessity of further research into nanostructured semiconductor nanomaterials is due to the unique optical, magnetic and surface properties they possess and the quantum effects that are demanded in the design of high-tech equipment.

According to Mousseau and Lewis,[236] the Si_{60} cluster with 'open surface structure',‡ unlike hydrogenated $Si_{60}H_{60}$ with the closed surface structure, has a non-zero spin and, hence, it is an example of a single-molecule magnet. Relying on the results derived from theoretical models,[236] the fullerene structure is preferred for Si_{60} over the network structure (similar to naphthalene) or cylindrical structure. The fullerene structure corresponds to a local minimum on the potential energy surface but it is unstable for silicon and susceptible to relaxation to a structure with restoration of the tetrahedral coordination.[11]

Several publications[218–220] were concerned with the properties of intercalated silicon nanoparticles constructed as fragments of a diamond-like lattice and a random atom packing and a nanoassembly of 60-atom fullerene containing an embedded 13-atom icosahedron in comparison with the same systems with hydrogen-passivated dangling bonds of the silicon atom.

‡ A surface with non-passivated external bonds.

In the initial system consisting of fullerene intercalated with a distorted icosahedron, an icosahedron atom is coordinated to five atoms of the fullerene structure with the bonds of length $L_b \sim 0.24$ nm. The total number of bonds between the fullerene-like outer shell and intercalated icosahedral shells reaches 60. The neighbour atoms in the icosahedron are spaced by a distance ~ 1.9 times longer than L_b. The central atom of the icosahedron is removed from the peripheral extended icosahedral shell by a distance 1.8 times greater than L_b, which, in principle, makes it possible to enhance the intraicosahedral coordinations by additional tetrahedral atomic groups. The Tersoff potential parameters for silicon were reported by Tersoff;[167, 168] the Lennard-Jones potential parameters were reported by Zhang and Jiang.[237] The repulsion (Lennard-Jones potential) was taken into account only if the atoms approached one another to inadmissibly short distances in the simulation of nanoassembly of an icosahedron and fullerene. The Tersoff potential is applicable to simulation of the systems with, on average, 3–4 covalent bonds per atom.[3, 5] The initial system had 5 fullerene atoms per each atom located on the icosahedron surface. Five closest neighbours of an icosahedron surface atom were not taken into account because the distance to them was ~ 1.9 times longer than the bond length L_b. In the absence of repulsion, the atoms rapidly approached one another to inadmissibly short distances with a surge in the internal pressure; therefore, the interatomic repulsion was included into the model algorithm.

VI.1. Model of the Si_{73} nanoassembly

The algorithm of integration of the motion equations in the simulation of Si_{73} nanoassembly was based on the fourth-order Runge–Kutta procedure with the time step of $\Delta t = 10^{-2}$ ps. The calculations involved three stages, 100 ps long each, starting from the same temperature of 35 K with heating in 90 K steps up to 1560 K. In one series of calculations, an onion nanoassembly of a 60-atom fullerene-like cage intercalated with an icosahedron with the lattice parameter $L_b = 0.24$ nm served as the initial structure (the lattice parameter of the bulk crystal is 0.235 nm). In another series of calculations, a diamond lattice fragment as a sphere comprising the coordination of 72 closest atoms around one of the lattice points was taken as the initial structure. Yet another calculation series was performed for the initial structure obtained by mimicking the cluster growth upon vapour condensation to form interatomic distances corresponding to a crystal. In subsequent calculations,[225] the same models were used to study stabilization of silicon clusters by passivating the dangling bonds with hydrogen, *i.e*., based on MD simulation of $H_{60}Si_{73}$ clusters.

The observed fast destruction of the local environment of atoms belonging to the icosahedron surface in the Si_{73} intercalate was due not only to their binding to fullerene but also to the absence of the tetrahedral angle (109.47°) between the bonds. The collapse of the nanoassembly in the case of using only the Tersoff potential was prevented by inclusion of repulsion forces (Lennard-Jones potential) in the consideration for atoms that approach each other to a distance of < 0.28 nm.[203, 218, 229] Three series of calculations were performed for silicon nanoparticles. The initial temperature was taken to be 10 K for each series; the computing duration was 100 ps for each temperature; the temperature for every subsequent computation was raised by

100 K, and the final computation was carried out at 1710 K.

To determine the initial configuration of the nanoparticle, in a series of calculations using the random packing of atoms, a sphere of a definite radius was filled with silicon atoms by means of the random number generator. In the initial state, the minimum distance between silicon atoms in the random packing did not exceed this value for the corresponding bulk crystal (0.24 nm). Therefore, and also due to reduction of the sphere filling time, the density of the initial atomic packing was not more than 0.6 of the density of the corresponding nanocrystal. In the series of nanoassembly computations, the initial configuration was a 60-atom fullerene structure containing an intercalated 13-atom icosahedron. The minimal distance between the atoms in this packing corresponded to the same characteristics of the bulk crystal of silicon.[229]

During the simulation, the temperature dependences of the potential energy and the volume of the silicon clusters were calculated (Fig. 35). The energy for a nanoparticle with a random packing of atoms is negative over the whole temperature range considered, while for particles with the initial crystal packing of atoms, a sharp peak is present in the curve $u\,(T)$ for $u > 0$ at 710 K. In the temperature range covered by this peak ($500 \leqslant T \leqslant 900$ K), the u values were found to be higher for a crystalline nanoparticle than for other nanoparticles. Similarly, the potential energy for a nanoparticle with the random packing of atoms in the region of the major peak ($1100 \leqslant T \leqslant 1300$ K) in the curve $u(T)$ was higher than for other nanoparticles. In all other cases, the u values for nanoassembled nanoparticles were higher than the energies of other particles.

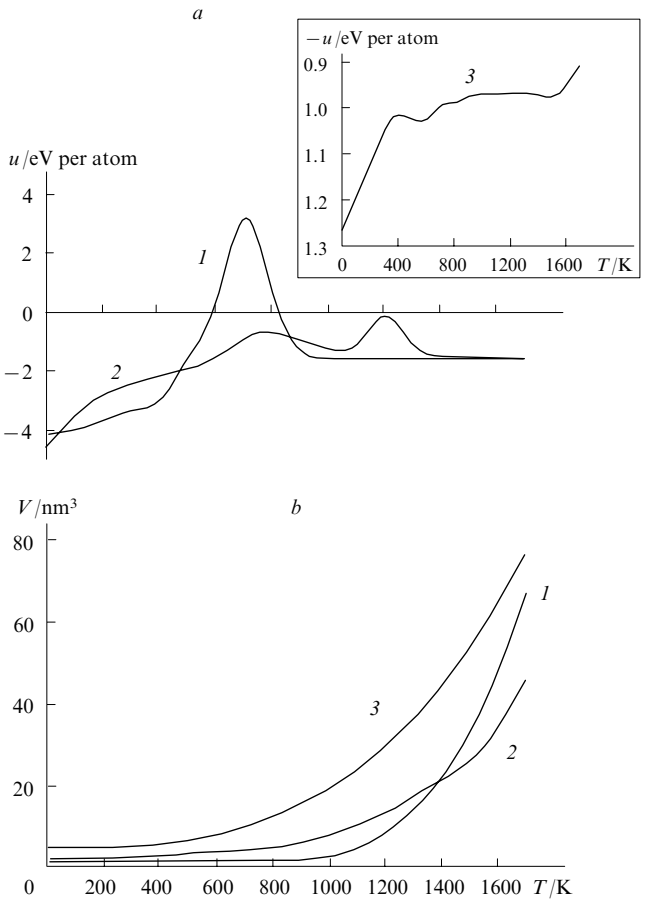


Figure 35. Temperature dependences of the specific potential energy (*a*) and volume (*b*) of nanoparticles comprising 73 silicon atoms.[218]
(*1*) Particle with diamond-like structure, (*2*) randomly packed particle, (*3*) nanoassembly of 60-atom fullerene and 13-atom icosahedron.

The volume containing 73 atoms was defined as the volume of a sphere circumscribed around the centre of mass of all the atoms that initially form the nanoparticle. The radius of this sphere was equal to the distance from the centre of mass to the centre of the most remote atom. In the case of a crystalline nanoparticle, a sharp growth took place at temperatures of >1010 K due to vaporization of various atoms. For other nanoparticles the increase in the volume with temperature rise was more gradual. A fast growth of the volume was detected starting from 510 K for a particle assembled from fullerene and icosahedron and starting from 910 K for a nanoparticle based on the random packing of atoms. Thus, the crystalline nanoparticle proved to be most resistant to atom vaporization.

The heat capacities of the models

$$C_P = \frac{\mathrm{d}H}{\mathrm{d}T}$$

were calculated by numerical differentiation of the enthalpy

$$H = E + PV$$

where E is the internal energy. The resulting value was compared with the heat capacity C_P of crystalline silicon.[238] In the case of the crystalline nanoparticle, a divergence of the C_P values was observed near the vicinity of the temperature of 710 K (Fig. 36), and the isobaric heat capacity of randomly packed nanoparticles had two maxima, at 610 and 1210 K. For the nanoassembled nanoparticle, the C_P value was especially low in the range of $1000 < T < 1300$ K.

To ensure the required spherical symmetry in the construction of radial distribution functions (RDFs) of atoms, the atom located most closely to the centre of mass was chosen as the reference point in the models. At 1710 K, the RDFs for three types of nanoparticles were found and compared with the experimental RDF (Ref. 239) for amorphous silicon. The limiting distance (2.5 nm) for which the RDFs were determined corresponded to the volume of ~ 65 nm^3; hence, it reflected the contributions of not only the nanoparticle atoms but also of most of vaporized atoms. As the temperature was raised, the pattern of the RDF of a nanoparticle with crystalline atomic packing was smeared but some of the peaks were still well-resolved even at 1710 K.

The density of randomly packed nanoparticles decreased following the increase in temperature, which was accompanied by displacement of the principal RDF peak from 0.25 to 0.28 nm. Initially (at 10 K), the RDF curve for the nanoassembled nanoparticle had the highest first peak. The increase in the scale of RDF correlations at 10 K for the assembled nanoparticle is caused by considerable displacements of the central and outer atoms resulting from strong repulsion from the neighbours. The number of vaporized atoms for such a nanoparticle was 8 at 1710 K, while for the randomly packed particle it was 6, and for a

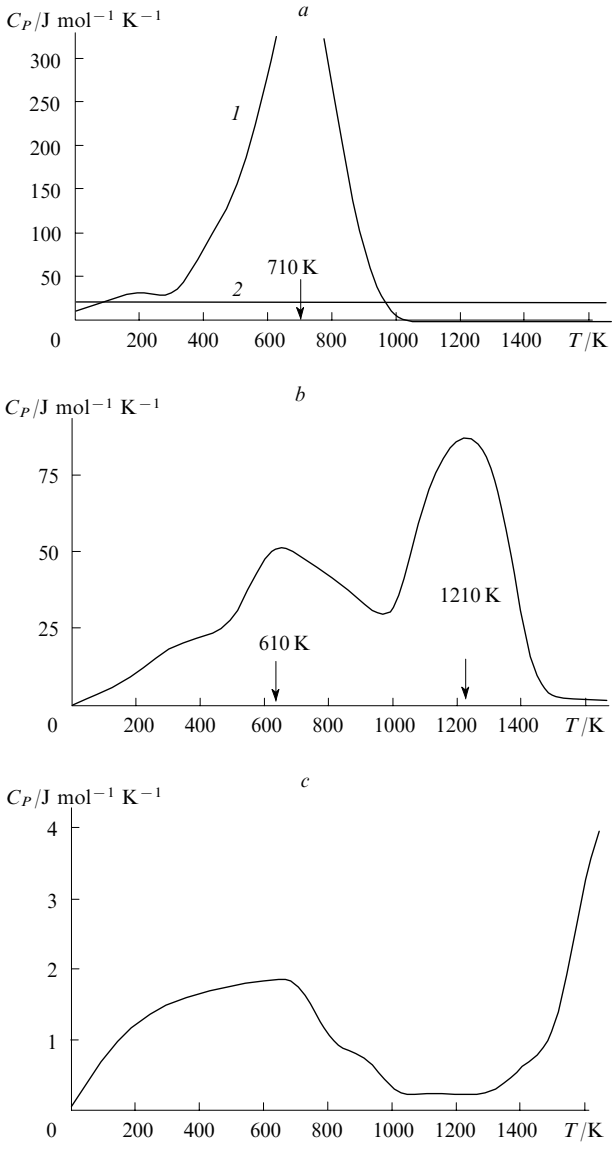


Figure 36. Temperature dependences of the isobaric heat capacity of silicon nanoparticles comprising 73 atoms.[218]
Initial structure: (*a*) diamond-like: (*1*) MD calculation, (*2*) experimental value for crystalline silicon;[238] (*b*) randomly packed; (*c*) icosahedron intercalated into fullerene.

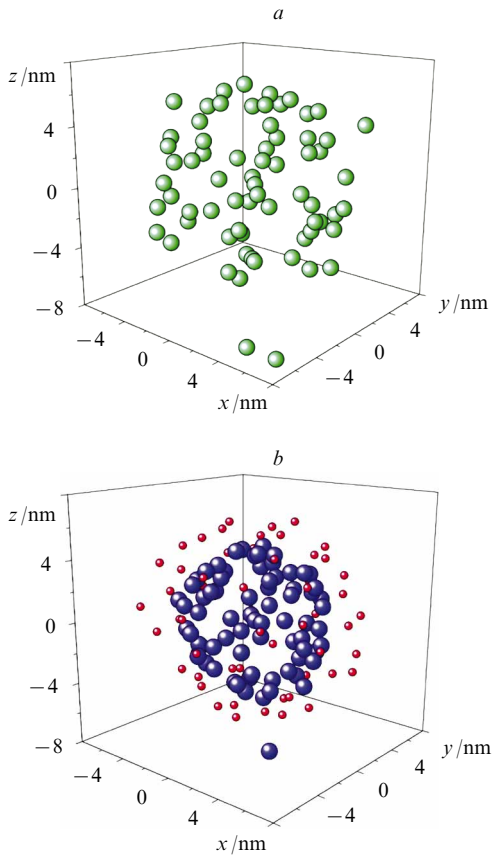


Figure 37. Structures Si_{73} (*a*)[203] and $H_{60}Si_{73}$ (*b*)[225, 229] at a temperature of 1560 K in the final point of the MD trajectory after 10^6 steps.

crystalline nanoparticle it was 4.[203] From analysis of the initial configuration of the nanoassembled nanoparticle (Fig. 37*a*) and its projections, it followed that the positions of atoms had considerably changed and the whole cluster structure had transformed. At high temperature, the particle was an amorphous entity in which close packing fragments alternated with voids.[225, 229]

The average number of bonds $\bar{n}_b$ per inner atom of the nanoparticle was determined by direct counting of the number of interatomic distances not exceeding 0.3 nm for 12 atoms located most closely to the nanoparticle central atom. The number $\bar{n}_b$ found in this way was maximum for the crystalline Si_{73} nanoparticle ($\bar{n}_b = 4.19$) at 10 K and minimum for the nanoassembled nanoparticle ($\bar{n}_b = 1.78$) at 1710 K. In the crystalline nanoparticle at 10 K, all bond angles coincided with the tetrahedral angle to an accuracy of up to 1.5°; however, as temperature increased, the angular distribution spectrum in the nanocrystal considerably changed. At 1710 K, the most intense range of the angular spectrum was from 90 to 146°, and the position of the principal peak was 117°.[229]

The diffusion coefficient of atoms was calculated by a standard procedure as the limit of the root-mean-square atomic displacement over a time period of 50 ps corresponding to atom migrations. It was shown [229] that the atom mobility in the nanoparticles in question increased with increasing temperature approximately according to a linear law (Fig. 38). In the case of a regular atomic packing, the local deviations of the temperature dependence of the diffusion coefficient $D(T)$ from linearity were more substantial and $D(T)$ determined for 73-atom nanoparticles was more than twice greater than the experimental diffusion coefficient of atoms on the surface of crystalline silicon at 1273 K.[240]

The difference between the physicochemical properties of nanoparticles is largely determined by their different initial structures. The high peak in the temperature dependence of the potential energy of a crystalline nanoparticle at 710 K is caused by its melting , which starts on the surface. The minor peaks at 710 and 1200 K in the $u(T)$ curve of a randomly packed silicon particle corresponded to the orientational structure ordering. The structural rearrangements in a nanoassembled nanoparticle were smooth. Only small peaks were present at 410 and 1200 K. Computer simulation using the MC method and the EDIP potential [241]

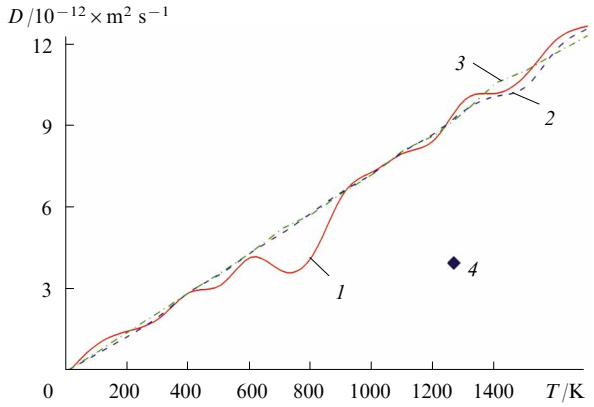


Figure 38. Temperature dependences of the diffusion coefficient of atoms in silicon nanoclusters.[203, 229]
(*1*) Particle of diamond-like structure, (*2*) particle with a random packing, (*3*) nanoassembly of 60-atom fullerene and 13-atom icosahedron, (*4*) experiment.[241]

for the crystalline and liquid phases of silicon at zero pressure revealed a feebly expressed liquid–liquid transition at 1135 K and a fluid to amorphous state transition at 843 K.

According to the Ehrenfest classification, phase transitions accompanied by a jumpwise change in the first derivatives of the thermodynamic potential (TP) are classified as the first-order phase transitions, while transitions with a sharp change of the second derivatives of the TP are referred to as second-order transitions.[242] Melting of bulk crystals is a first-order transition as both the volume and the entropy change jumpwise.

For small nanoparticle sizes, the changes in the volume and the entropy are slight, so that the melting phase transition in nanoparticles can be conventionally classified as a second-order transition.[243] For normally melting compounds, the increase in the nanoparticle volume upon melting can be counterbalanced by its compression under the action of Laplace pressure. Since the Laplace pressure is inversely proportional to the nanoparticle size, the counterbalancing is not effective for large particles, melting in which is thus a first-order transition. In the case of silicon, the situation is different. On melting of a silicon crystal, the volume decreases, *i.e.*, the transition to a closer packing takes place. The decrease in the volume upon melting could also be expected for Si nanoparticles, but due to the short-range character of Si–Si interactions, the more free surface atoms are easily detached from the bulk part. This gives rise to a negative radial density gradient and brings about the necessity to minimize the change in the volume upon the disordering of the pre-melting structure. Due to the specific character of the interatomic Si–Si interaction, the Laplace pressure should not affect the coordination.

The temperature dependence of C_P for a crystalline nanoparticle exhibited a sharp peak at 710 K. Less clear-cut peaks were noted in this curve at this temperature for randomly packed nanoparticles. The specific features of the $C_P(T)$ curve that were found for a nanoassembled particle can be regarded as fluctuations. The temperature of 710 K corresponded to the maximum deviation (to lower values) of the diffusion coefficient for a crystalline nanoparticle from the linear dependence.[226] This is attributable to the fact that the irreversible destruction of the crystal structure was immediately preceded by retartadion of the thermal motion of atoms through chaotization.[244]

The essence of this phenomenon is as follows. The arrangement of atoms in a crystal lattice can be represented as a packing of atom layers alternating in a particular way. The silicon atoms are held in the lattice by strong short-range interactions. Initially, the lattice has no point defects (vacancies or interstitial atoms). At high temperature, the crystal lattice is distorted, the atomic layers are highly deformed and it is difficult to identify them. In the vicinity of the melting point, the amplitudes of atomic vibrations increase so that some atoms can cleave the bonds with atoms of the same layer; however, they are not free to migrate to the second layer. The transition from a regular to irregular atom packing is a collective process in which separate atom motion is hampered.[245] The kinetic complications in the structural rearrangement are reflected in the sharp decrease in the diffusion coefficient. On further heating of the system, atom collisions become more frequent and more intense. The number of broken bonds sharply increases and specific translational motion of atoms is detected as a considerable increase in the diffusion coefficient upon transition of the model system into the fluid (liquid) state.

A highly important problem of the synthesis of silicon nanoclusters is their calibration according to size with efficient control over the coalescence process in gas flow as a result of decrease in the number of reactive collisions, for example, upon cluster ionization.[225, 229, 246–248] An alternative way for decreasing the reactivity of collisions is hydrogen passivation of dangling bonds on the surface of Si particles in the temperature range of 300–1800 K.[11] The presence of hydrogen atoms on the nanoparticle surface imparts elasticity to the atom collisions in controlled gas flows and even in liquids. Indeed, Murphy *et al.*,[247] who proposed *a priori* the hypothetical possibility of the existence of a fullerene-like Si_{60} structure and estimated its electronic characteristics, concluded that the existence of a set of 'open' and 'closed' fullerene-like structures based on the truncated Si_{60} icosahedron is possible. The question of synthesis of a new class of supramolecular magnets based on this structures remains open as the problem of thermal stability of the clusters has not been solved.

In the study of thermal stability of the disperse states by chemical nanomechanics,[11] intercalated Si_{73} particles were taken as the initial cluster structures and onion compositions were constructed based on them (the model particles were surrounded by a shell of hydrogen atoms). In the $Si_{73}H_{60}$ structures thus formed,[225] hydrogen atoms were located at a 0.22 nm distance from each other and from the closest silicon atoms (see Fig. 37*b*). The construction of this structure resulted in the hydrogen ligand density of $\sim$42–45 kg m^{-3}, which is almost twice lower than the real density of liquid hydrogen at 20 K (70 kg m^{-3}). The initial temperature for the MD simulation of this ligand was 35 K, which was higher than the boiling point of liquid hydrogen (20 K); in other words, the ligand corresponded to a dense gas if the adjacent Si_{60} shell was neglected.

Comparison of the thermal evolution of the cluster ligands with different initial structures upon temperature rise demonstrated the monotonic increase in their internal energy from -5.18 eV per atom at 35 K to -2.65 eV per atom at 1560 K for Si_{73} (a diamond lattice fragment). For the nanoassembled cluster and randomly packed cluster, the energy changes were more abrupt. In the case of a nanoassembled cluster at 2/3 of the complete heating range, the

energy was found to be close to −4.33 eV per atom, which corresponded to the energy of bulk crystal (−4.36 eV per atom).[249] During heating of the randomly packed cluster ligand, the same value was attained at a lower temperature (about 750 K). For all of the simulated cluster ligands, the RDFs around the atoms proximate to the centre of mass were calculated. The nanoassembly had the most stable structure, judging from the fact that the initial RDF form was retained: the two initial peaks corresponding to the first (comprising 12 atoms) and second (a 60-atom fullerene cage) coordinations at 1560 K coalesced into one peak. More complex RDF peaks of nanocrystals and a randomly packed cluster changed with heating: mainly, they gradually shifted due to increase in the interatomic distances (lowering of density). Noteworthy are also the transformations of the distribution functions of angles between the Si–Si bonds where the predominant angle of 91.8° was retained for all of the considered clusters. As the temperature increased, the angle distribution in the Si_{73} nanocrystal changed fundamentally (the peak at 110 K disappeared).

The dependence of the cluster size on temperature was elucidated by analyzing the thermal expansion caused by the change of bond lengths and by vaporization of atoms from the cluster surface. Overally, this resulted in either a monotonic or stepwise increase in the cluster radius (R_{cl}) defined as the distance from the centre of mass to the most remote silicon atom on the surface. The temperature dependence of R_{cl} for Si_{73} passes through a maximum, which is indicative of a pronounced influence of vaporization.[229] The less clear-cut peaks at higher temperature are characteristic of the nanoassembled and crystalline clusters, which confirms their higher thermal stability as compared with clusters with different structure. The smallest radius at 1560 K was found for the nanoassembly, which was most stable out of the three clusters. Yet another criterion of cluster thermal stability was the heating-initiated penetration of hydrogen atoms into the cluster shell determined by the ratio[250]

$$\xi = \frac{R_{cl} - R_H}{R_{cl}}$$

where R_H is the distance to the hydrogen atom located most closely to the centre of mass. The kinetic penetration for the nanoassembled cluster was maximum at 1100 K; for the nanocrystallite, a similar dependence had two maxima on heating to 1150 K; for the randomly packed cluster, the value was the highest, the dependence was generally monotonic and had a slight peak at 690 K.[229]

It is noteworthy that the extrema in the temperature dependences of R_{cl} and ξ were parallel. The penetration process was activated with the onset of heating and occurred as intense transitions of hydrogen atoms from the state of adatoms to the absorbates (this was most pronounced for the cluster having random and looser packing), which was reflected in the increase of the diffusion mobility. The shell of adatoms was most thermally stable over the whole heating range and had a considerable stabilizing effect at $T < 600$ K *via* the Laplace pressure (enhanced by the H–H mutual repulsion) on the adjacent shells of silicon atoms. Also, single cases of spontaneous vaporization of some silicon atoms were detected. The feebly pronounced tetrahedral angle of 109.5° and the highest density at 1560 K were characteristic of the nanoassembled cluster upon coalescence of two concentric shells (he fullerene cage and the intercalated icosahedron), while retention of a high degree of tetrahedral coordinations on heating was characteristic of the nanocrystallite.[251] Note that the linear expansion coefficient β for the Si_{60} cluster with additional stabilization of the fullerene-like core by intercalation of 60 hydrogen atoms[11] was negative, as opposed to other models considered above ($\beta = -1.51 \times 10^{-5}$ K^{-1}). This is caused by the capillary contraction of the shell and the action of surface tension of the proper Si_{60} cluster.[229]

VI.2. Silicene, germanene and stanene

The successful application of the beam epitaxy and gas-phase synthesis techniques[252] for the formation of graphene sheets and stacks of acceptable sizes stimulated the attempts to prepare by the same methods silicene, stanene and germanene[253–255] — two-dimensional crystals of silicon, tin and germanium, respectively. In the case of graphene, the interface is formed upon sorption (adsorption or chemisorption) largely owing to the nanorange and the specific character of interplane interaction. The specific interface structure in the contact areas upon the epitaxial deposition of silicon, germanium and tin atoms as island films on metallic substrates is caused by the superposition of the incommensurable lattices of these films and the metals.

The early attempts to obtain germanene as a two-dimensional germanium crystal on the (111) silver surface, which would have reproduced the successful synthesis of silicene [on the (111) surface of Ag, Ir, ZrB_2 and Au],[253] failed due to the instability of germanium (the structure formed by the Ag_2Ge phase proved to be more stable; one-third of the silver atoms of the contact monolayer were replaced by the germanium atoms). The surface of silicene deposited on Ag(111) was corrugated and the Si/Ag(111) interface was clear-cut. However, attempts to synthesize germanene on metallic substrates resulted in not only uncontrolled structure distortions of coordinations of the monoatomic germanium sheet but also undesirable changes in its electronic properties. It was only in 2014 that attempts of Davila *et al.*,[254] who used Pt and Au substrates, led to the synthesis of germanene with a complex ring cluster superlattice.

Gao and Zhao[256] carried out comparative analysis of the formation and thermal evolution of two-dimensional C_N and Si_N clusters and layered C_N/M and Si_N/M composites (M = Pd, Ni, Cu, Al) based on MD simulation using interparticle interaction potentials calculated in terms of the modified density functional theory.[152] The silicene interface proved to be non-planar (the overall interface thickness was 1.6 nm) but ribby (corrugated) (Fig. 39) and having no so clear-cut sp^2- and sp^3-hybridized coordinations as model Si spheroids[229] (fullerene analogues). The charge transfer in silicene occurs as a flux of weightless high-speed fermions ($\sim 10^5$–10^6 m s^{-1}).[253]

Analysis of the silicene surface for model structure *I* (see Fig. 39 *a*) demonstrated that the double rings (six-atom inner rings and twelve-atom outer rings) are formed by only one-third of the silicon atoms, which is consistent with the STM experiment data,[253] whereas in the case of structure *II*, the superlattice cells involve only pairs of silicon atoms spaced by 0.576 nm and comprising ~1/7 of all silicon atoms located on the outer surface (see Fig. 39 *b*).

Each of the hexagonal rings of superstructure *III* involves one outer silicon atom. Thus, in the series of structures *I*–*III*, the number of silicon atoms that violate the planar structure of silicene decreases (see Fig. 39 *c*), which is in line with experimental results.[253] The studies using STM methods and low-energy electron diffraction also revealed the specific features of the hexagonal struc-

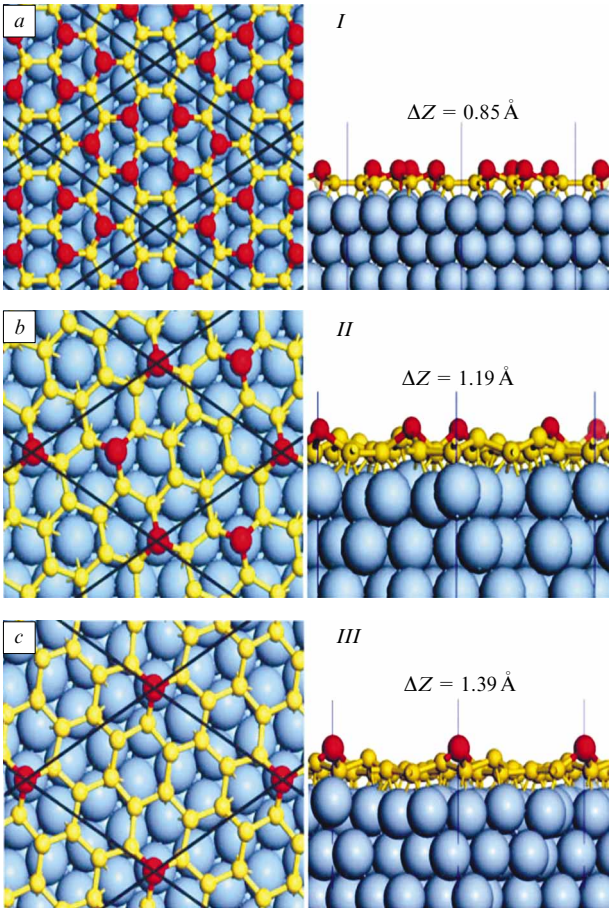


Figure 39. Atomic structures of silicene [deposition of silicon atoms on the (111) surface of silver].[256]
Type of structure: *I* (*a*), *II* (*b*), *III* (*c*); on the left is top view, on the right is side view: ΔZ is deviation from the Ag(111) surface; the most remote atoms (by ~0.2 nm) are enlarged and darker coloured.

tures of germanene and established the degrees of distortion.[254]

However, the results of quantum mechanical calculations of characteristics of stanene and stanane (stanene passivated by hydrogen atoms, in essence, analogue of graphane) proved to be most surprising. According to the data of prognostic calculations,[255–257] a tin nanoribbon decorated by fluorine or chlorine atoms on the edge can be classified by a superconductor.

VII. Conclusion

The review presents a discussion of the results of computer experiments studying clusters not only as nanophase precursors but also as an intermediate form of atomic-and-molecular organization with structure and specific properties brought about by a small volume and the non-autonomous surface layer composed of several shells (<1 nm) and, most of all, the last one with the highest bond unsaturation. Full description of nano-sized objects such as clusters requires the idea of scaling, superposition of quantum states and statistical characteristics in the bulk and in the surface shells, interfacial states and bond hybridization upon contact of clusters with the substrate.[9, 164, 165] A topical problem is development of effective methods for the synthesis and attainment of thermodynamic stability of cluster-dispersed materials with promising properties, in view of the high potential of the energy of dissipative structures they store, and retention of the service characteristics upon subsequent operation.

The studies of interactions of nanoparticles with the substrate material, which is far from being inert in the general case, are also important. Apart from enhancement of the cooperative effect of the interface, the substrate in a cluster-dispersed 2D system increases substantially the thermal stability of the clusters as the integrating tunnelling current appears. The substrate also prevents intense leaching — atom emissions and migration appearance of reactive zones in the stationary states of catalysts.

The destruction of the regular structure (as analogue of melting of bulk systems) of isolated metal nanoclusters and their cluster/substrate interfacial compositions is not a phase change but is an order–disorder transition with high the atom mobility. This transition has a more complex mechanism than melting of bulk crystals, as it is accomplished in a wider temperature range (~1/3 of the heating range), involves several stages (isomerization, quasi-melting, disappearance of the faceted morphology and shell structure). The disorder processes and stability of clusters are affected by not only the substrate material but also the specific features of sorption in the contact area, which is either chemisorption or adsorption on the metal/graphene interface depending on the electronic structure of the metal. In the case of chemisorption, the stability of the metal subsystem is 200–300 K higher than in the case of adsorption. The melting temperature in the case of graphite (graphene) coating of endohedral clusters $M@C_n$ or metal intercalation into CNTs can be more than 50 K higher than the melting point of bulk phases.[145, 146] The thermal stability of silicon in the nanorange decreases less abruptly than for metallic nanosystems. For example, it increases upon intercalation of fullerene-like silicon clusters with metal atoms or clusters or introduction of hydrogen to saturate the dangling —Si—Si— bonds.[225, 229] The thermal stability of two-dimensional Si_n clusters (nanocrystals) is controlled by selecting appropriate substrates [Ag(111), Pt(111) and so on].[253, 256]

An efficient increase in the thermal stability of the atomic structure and control over the electron band structure [retention of the linear or parabolic dependence $E(k)$ shaped like the Dirac cone] in interfaces with graphene[258] and silicene[259] can be achieved by intercalation doping. First of all, this refers to sandwich type interfaces (M/G/M, M/Si/M) in which films of, for example, Group VIII ferromagnetic metals serve as two-sided electrodes. Indeed, the Ni/G/Ni system is able to separate (filter) electrons according to their spin states.[258] The separation mechanism is as follows: the charge transport of electrons of only one spin state occurs *via* the overlap of the metal and graphene Fermi levels.[260] The synthesis of such materials is highly important for the development of spintronics considering both the high speed of electrons in graphene- (M/G) or silicene- (M/Si) reinforced composites and a substantial increase in the capacity of data storage media and data processing rate. The high-precision intercalation of interlayer M/G/M structures is achieved by epitaxial (or CVD) deposition of an additional protector monolayer (of either d-metals having adsorption properties such as Au, Cu, Pt[258] or other metals such as alkali metals or aluminium) for doping the structure with electrons.[259–262] The intercalation doping of the interface by, for example, a gold sublayer (Ni/G/Ni + Au, Ni/Au/G/Ni) to prevent the deg-

radation of electronic characteristics caused by atomic structure disordering results in the position of the Dirac cone band structure exactly corresponding to the Fermi level,[258] while intercalation doping with alkali metals or aluminium[261] results in the position below the Fermi level.[260, 262]

The simulation reproduces processes that are still difficult to observe experimentally but that occur with high probability during the real synthesis of nanoelectronic elements. For instance, a computer analogue of the catalytic synthesis of nanotubes on transition metal clusters in a reactor with the carbon vapour phase of the same composition as in real experiments was implemented by the MD method and studied in detail at the atomic and molecular level.

Thus, computer simulation making use of physically substantiated interatomic interaction potentials[263] reveals the atomic and molecular details of the key features of nucleation, nanocluster growth, successive and defect-free formation of coordination shells, structure transitions and morphological details of the cluster surfaces, provides for effective control of functional properties during hybridization of cluster bonds with substrates and ensures the retention of other physicochemical parameters of nanosystems during the material synthesis.

The obtained simulation data and analysis of their agreement with experimental results prompt that computer simulation using quantum mechanical estimates of interatomic interactions would also make it possible to predict the structure and thermodynamic properties of some new noncrystalline materials.

The authors are grateful to colleague E D Kurbanova for her invaluable help in the computer preparation of the text and graphics.

The review was prepared with the financial support of the Division of Chemistry and Materials Science of the Russian Academy of Sciences (Project No. 12-T-3-1022).

References

1. I Prigogine *Introduction to Thermodynamics of Irreversible Processes* (New York: Wiley, 1961)
2. H Haken *Information and Self-Organization. A Macroscopic Approach to Complex Systems (Springer Series in Synergetics)* (Berlin, Heidelberg: Springer, 2006)
3. G B Sergeev *Nanokhimiya* (Nanochemistry) (Moscow: Moscow State University, 2003)
4. A L Buchachenko *Russ. Chem. Rev.* **75** 1 (2006)
5. A A Eliseev, A V Lukashin *Funktsional'nye Nanomaterialy* (Functional Nanomaterials) (Moscow: Fizmatlit, 2010)
6. I P Suzdalev *Nanotekhnologiya: Fiziko-Khimiya Nanoklasterov, Nanonostruktur i Nanomaterialov* (Nanotechnology Physical Chemistry of Nanoclusters, Nanostructures and Nanomaterials) (Moscow; KomKniga, 2006)
7. M I Alymov *Poroshkovaya Metallurgiya Nanokristallicheskikh Materialov* (Powder Metallurgy of Nanocrystalline Materials) (Moscow: Nauka, 2007)
8. D K Belashchenko *Komp'yuternye Modeli Zhidkikh i Amorfnykh Veshchestv* (Computer Models of Liquid and Amorphous Compounds) (Moscow: Moscow Institute of Steel and Alloys, 2005)
9. V A Polukhin, N A Vatolin *Modelirovanie Razuporyadochennykh i Nanostrukturirovannykh Faz* (Modelling of Disordered and Nanostructured Phases) (Ekaterinburg: Ural Branch of the Russian Academy of Sciences, 2011)
10. G F Mansuri *Principles of Nanotechnology: Molecular-Based Study of Condensed Matter in Small Systems* (World Scientific, 2005)
11. V A Polukhin *Modelirovanie Nanostruktury i Prekursornykh Sostoyanii* (Modelling of Nanostructures and Precursor States) (Ekaterinburg: Ural Branch of the Russian Academy of Sciences, 2004)
12. A P Shpak, Yu A Kunitskii, V I Lysov *Klasternye i Nanostrukturnye Materialy* (Cluster and Nanostructured Materials) (Kiev: Akademperiodika, 2002)
13. A G Vorontsov, B R Gel'chinskii, A E Korenchenko *J. Exp. Theor. Phys.* **115** 789 (2012) [*Zh. Eksp. Teor. Fiz.* **142** 837 (2012)]
14. U Backman, J K Jokiniemi, A Auvinen, K E J Lehtinen *J. Nanopart. Res.* **4** 325 (2002)
15. V Rotello *Nanoparticles: Building Blocks for Nanotechnology (Nanostructure Science and Technology)* (Berlin: Springer, 2003)
16. H C Andersen *J. Chem. Phys.* **72** 2384 (1980)
17. Yu Ya Gafner, S L Gafner, L V Redel, Zh V Goloven'ko *J. Nanosci. Nanotechnol.* **14** 5138 (2014)
18. S N Pronkin, P A Simonov, V I Zaikovskii, E R Savinova *J. Mol. Catal. A* **265** 141 (2007)
19. L A Kibler, A M El-Aziz, R Hoyer, D M Kolb *Angew. Chem., Int. Ed.* **44** 2080 (2005)
20. F Hernandez, H Baltruschat *Langmuir* **22** 4877 (2006)
21. A S Kashin, V P Ananikov *J. Org. Chem.* **78** 11117 (2013)
22. V P Ananikov, I P Beletskaya *Organometallics* **31** 1595 (2012)
23. S S Zalesskiy, A E Sedykh, A S Kashin, V P Ananikov *J. Am. Chem. Soc.* **135** 3550 (2013)
24. A T N'Diaye, T Gerber, C Buss *New J. Phys.* **11** 103045 (2009)
25. M Gao, Y Pan, C Zhang *Appl. Phys. Lett.* **96** 053109 (2010)
26. Y L Wang, A A Saranin, A V Zotov, M Y Lai, H H Chang *Int. Rev. Phys. Chem.* **27** 317 (2008)
27. Z Xu, M J Buehler *J. Phys.: Condens. Matter* **22** 485301 (2010)
28. R M Lyndenbell, D J Wales *J. Phys. Chem.* **101** 1460 (1994)
29. P M Aiagan, L D Marks *Phys. Rev. Lett.* **80** 585 (1988)
30. M J Cini *Catalysis* **37** 187 (1975)
31. B M Smirnov *Fizika Fraktal'nykh Klasterov* (The Physics of Fractal Clusters) (Moscow: Nauka, 1991)
32. J P K Doye, D J Wales *Phys. Rev. Lett.* **86** 5719 (2001)
33. G G Rusina, S D Borisova, E V Chulkov *J. Phys. Chem. A* **87** 233 (2013) [*Zh. Fiz. Khim.* **87** 236 (2013)]
34. S A Nepiiko *Fizicheskie Svoistva Malykh Metallicheskikh Chastits* (Physical Properties of Small Metal Particles) (Kiev: Naukova Dumka, 1985)
35. Yu I Petrov *Klastery i Malye Chastitsy* (Clusters and Small Particles) (Moscow: Nauka, 1986)
36. D I Ryzhonkov, V V Levina, E L Dzidziguri *Nanomaterialy* (Nanomaterials) (Moscow: Binom. Laboratoriya Znanii, 2008)
37. V V Starostin *Materialy i Metody Nanotekhnologii* (Materials and Methods of Nanotechnology) (Moscow: Binom. Laboratoriya Znanii, 2008)
38. A W Castleman, K H Bowen *J. Phys. Chem.* **100** 12911 (1996)
39. C P Poole Jr, F J Owens *Introduction to Nanotechnology* (New York: Wiley 2003)
40. V Ya Shevchenko *Nanotekhnol. Ekolol. Proizvod.* **4** 108 (2010)
41. V Ya Shevchenko, A L Mackay *Glass Phys. Chem.* **34** 1 (2008)
42. M M Dzugutov *Phys. Rev. Lett.* **70** 2924 (1993)
43. V A Polukhin, R M Belyakova, L K Rigmant *Russ. Metallurgy (Metally)* (8) 681 (2010) [*Rasplavy* (1) 12 (2010)]
44. V Ya Shevchenko, V A Blatov, G D Ilyushin *Glass Phys. Chem.* **39** 229 (2013) [*Fiz. Khim. Stekla* **39** 3 (2013)]
45. V A Blatov, G D Ilyushin *Russ. J. Inorg. Chem.* **56** 729 (2011) [*Zh. Neorg. Khim.* **56** 778 (2011)]
46. T Aste *J. Phys: Condens. Matter* **17** S2361 (2005)
47. J Conway, N Sloane *Proc. R. Soc. A* **453** 2369 (1997)

48. M N Vargaftik, N Y Kozitsyna, N V Cherkashina, R I Rudyi, D I Kochubei, B N Novgorodov, I I Moiseev *Kinet. Catal.* **39** 740 (1998) [*Kinet. Katal.* **39** 806 (1998)]
49. A I Gusev *Nanomaterialy, Nanostruktury, Nanotekhnologii* (Nanomaterials, Nanostructures, Nanotechnology) (Moscow: Fizmatlit, 2005)
50. D Gittins, D Bethel, D Shifrin, R Nichols *Nature (London)* **408** 67 (2000)
51. R Z Valiev, I V Aleksandrov *Nanostrukturnye Materialy, Poluchennye Intensivnoi Plasticheskoi Deformatsiei* (Nanostructured Materials, Production by Intensive Plastic Deformation) (Moscow: Logos, 2000)
52. R A Andrievski, A V Ragulya *Nanostrukturnye Materialy* (Nanostructured Materials) (Moscow: Akademiya, 2005)
53. D M Mittleman, R W Schoenlein, J J Shiang, V L Colvin, A P Alivisatos, C V Shank *Phys. Rev.* **49** 14435 (1994)
54. Y Nosaka, K Tanaka, N Fujii *J. Appl. Polym. Sci.* **47** 1773 (1993)
55. V S Baidyshev, Yu Ya Gafner, V M Samsonov, A G Bembel *Crystallogr. Rep.* **60** 95 (2015) [*Kristallografiya* **60** 104 (2015)]
56. E Blaistenbarojas, M R Zachariah *Phys. Rev. B* **45** 4403 (1992)
57. R S Berry *C.R. Phys.* **3** 319 (2002)
58. J A Alonso *Structure and Properties of Atomic Nanoclusters* (London: Imperial Colledge Press, 2011)
59. Y Wang, S Teitel, C Dellago *J. Chem. Phys.* **122** 214722 (2005)
60. L J Lewis, P Jensen, J-L Barrat *J. Phys. Rev.* **56** 2248 (1997)
61. S L Gafner, L V Redel, Z V Goloven'ko, Y Y Gafner, V M Samsonov, S S Kharechkin *J. Exp. Theor. Phys. Lett.* **89** 364 (2009) [*Pis'ma Zh. Eksp. Teor. Fiz.* **89** 425 (2009)]
62. Y N Gornostyrev, I N Kar'kin, M I Katsnel'son, A V Trefilov *Phys. Met. Metall.* **96** 135 (2003) [*Fiz. Met. Materialoved.* **96** (2) 19 (2003)]
63. V A Polukhin, L K Rigmant, N A Vatolin *J. Phys., Conf. Ser.* **98** U333 (2008)
64. V A Polukhin, E D Kurbanova, L K Rigmant, A E Galashev, N A Vatolin *Perspekt. Mater.* (4) 13 (2009)
65. F Cleri, V Rosato *Phys. Rev. B* **48** 22 (1993)
66. S Sato, D R Chen, D Y H Pui *Aerosol Air Qual. Res.* **7** 278 (2007)
67. V A Polukhin, E D Kurbanova, A E Galashev *Russ. Metallurgy (Metally)* (8) 696 (2012) [*Rasplavy* (3) 15 (2012)]
68. A N Sirenko, D K Belashchenko *Nanotechnol. Russ.* **8** 239 (2013) [*Ros. Nanotekhnol.* **8** (3 – 4) 76 (2013)]
69. D L Tytik, D K Belashenko, A N Sirenko *J. Struct. Chem.* **49** 109 (2008) [*Zh. Strukt. Khim.* **49** 115 (2008)]
70. P V Lebedev-Stepanov, R M Kadushnikov, S P Molchanov, A A Ivanov, V P Mitrokhin, K O Vlasov, N I Rubin, G A Yurasik, V G Nazarov, M V Alfimov *Nanotechnol. Russ.* **8** (3 – 4) 137 (2013) [*Ros. Nanotekhnol.* **8** (1 – 2) 5 (2013)]
71. S L Gafner, L V Redel, Yu Ya Gafner *J. Exp. Theor. Phys.* **108** 784 (2009) [*Zh. Eksp. Teor. Fiz.* **135** 899 (2009)]
72. V A Polukhin, E D Kurbanova, A E Galashev *Vestn. Kazan. Tekhnol. Univ.* (1) 75 (2010)
73. C L Cleveland, W D Luedtke, U Landman *Phys. Rev. B* **60** 5065 (1999)
74. V A Polukhin, Yu Ya Gafner, I V Chepkasov, E D Kurbanova *Russ. Metallurgy (Metally)* (2) 112 (2014) [*Rasplavy* (6) 3 (2013)]
75. V I Bukhtiyarov *Russ. Chem. Rev.* **76** 553 (2007)
76. T N Rostovshchikova, V V Smirnov, V M Kozhevin *Ros. Nanotekhnol.* **2** 47 (2007) [a]
77. G V Vstovskii, A G Kolmakov, I Zhunin *Vvedenie v Mul'tifraktal'nuyu Parametrizatsiyu Struktur Materialov* (Introduction to Multifractal Parameterization of Material Structures) (Izhevsk: NITs RKhD, 2001)
78. B K Barakhtin, V F Chashnikov *Vopr. Materialoved.* (4) 10 (2001)
79. Yu Ya Gafner, Zh V Goloven'ko, S L Gafner *J. Exp. Theor. Phys.* **116** 252 (2013) [*Zh. Eksp. Teor. Fiz.* **143** 288 (2013)]
80. I V Chepkasov, Yu Ya Gafner, E D Kurbanova, V A Polukhin *Lett. Mater.* **4** 249 (2014)
81. V A Polukhin, E D Kurbanova, L K Rigmant *Butlerovskie Soobshcheniya* **25** 1 (2011)
82. V A Polukhin, E D Kurbanova, in *Sovremennye Metallicheskie Materialy i Tekhnologii (SMMT-2011): Trudy Mezhdunarodnoi Nauchno-Tekhnicheskoi Konferentsii* (Advanced Metal Materials and Technologies, 2011: Proceedings of International Scientific and Technical Conference) (St Petersburg: St Petersburg Polytechnic University, 2011) p. 262
83. V A Polukhin, E D Kurbanova, A E Galashev, in *The 14th International Conference on Liquid and Amorphous Metals (Ser. EPJ Web of Conferences), Rome 2011* Vol. 15, p. 03002
84. V A Polukhin, E D Kurbanova, L K Rigmant, N A Vatolin *Perspekt. Mater.* (11) (Special Issue) 93 (2011)
85. J P K Doye *Global Optimization. Nonconvecs Optimization and its Applications* **85** 103 (2006)
86. S L Gafner, Yu Ya Gafner *J. Exp. Theor. Phys.* **107** 712 (2008) [*Zh. Eksp. Teor. Fiz.* **134** 831 (2008)]
87. S L Gafner, Zh V Redel', Yu Ya Gafner *Metallofiz. Noveishie Tekhnol.* **29** 981 (2007)
88. P Hegra, O Stenzel, N Kaiser *Proc. SPIE* **5250** 21 (2004)
89. M M Mariscal, O A Oviedo, E P M Leiva *Metal Clusters and Nanoalloyas. From Modeling to Applications* (New York, Heidelberg, London: Springer Science and Business Media, 2013)
90. L J Lewis, P Jensen, J-L Barrat *Phys. Rev. B* **56** 2248 (1997)
91. S Ino *J. Phys. Soc. Jpn.* **27** 941(1969)
92. X S Li, W W Cai, J H An, S Kim, J Nah, D X Yang, R Piner, A Velamakanni, I Jung, E Tutuc *Science* **324** 1312 (2009)
93. A G Vorontzov, B R Gel'chinskii, A E Korenchenko *J. Exp. Theor. Phys.* **115** 789 (2012) [*Zh. Eksp. Teor. Fiz.* **142** 897 (2012)]
94. K Yasuoka, X C Zeng *J. Chem. Phys.* **126** 124320 (2007)
95. S Braun, F Roemer, T Kraska *J. Chem. Phys.* **131** 064308 (2009)
96. N Lumenn, T Kraska *Comput. Mater. Sci.* **35** 210 (2006)
97. A Y Galashev, V A Polukhin *Phys. Met. Metall.* **115** 697 (2014) [*Fiz. Met. Metalloved* **115** 621 (2014)]
98. N Luo, K X Liu, X J Li, Z W Wu, S Y Wu, L M Ye, Y Shen *Mendeleev Commun.* **22** 248 (2012)
99. N Luo, T Chen, K Liu, Y Shen *Mendeleev Commun.* **23** 153 (2013)
100. A N Simonov, P A Pyrjaev, B L Moroz, V I Bukhtiyarov, V N Parmon *Electrocatalysis* **3** 119 (2012)
101. J K Nørskov, F Abild-Pedersen *Nature (London)* **461** 1223 (2009)
102. I P Beletskaya, A N Kashin, I A Khotina, A R Khokhlov *Synlett* (10) 1547 (2008)
103. M Lamblin, L Nassar-Hardy, J-C Hierso, E Fouquet, F-X Felpinb *Adv. Synth. Catal.* **352** 33 (2010)
104. T D Blumke, F M Piller, P Knochel *Chem. Commun.* **46** 4082 (2010)
105. G Schmid, D Fenske *Philos. Trans. R. Soc. A* **368** 1207 (2010)
106. E G Mednikov, L F Dahl *Philos. Trans. R. Soc. A* **368** 1301 (2010)
107. V P Ananikov, I P Beletskaya *Dalton Trans.* **40** 4011 (2011)
108. F A Al-Odail, A Anastasopoulos, B E Hayden *Phys. Chem. Chem. Phys.* **12** 11398 (2010)
109. L V Beletskaya, D A Pichugina, N E Kuz'menko *Nanotechnol. Russ.* **6** 717 (2011) [*Ros. Nanotekhnol.* **6** (11 – 12) 53 (2011)]
110. F T Andón, B Fadeel *Acc. Chem. Res.* **46** 733 (2013)
111. K A Rumyantsev, A A Shemetov, I R Nabiev, A V Sukhanova *Nanotechnol. Russ.* **8** 700 (2013) [*Ros. Nanotekhnol.* **8** (11 – 12) 18 (2013)]
112. A V Pastukhov, Author's Abstract of Doctoral Thesis in Chemical Sciences, Institute of Organoelement Compounds, RAS, Moscow, 2009
113. J M Delgado, A Rodes, J M Orts *J. Phys. Chem.* **111** 14476 (2007)
114. K S Kim, Y Zhao, H Jang *Nature (London)* **457** 706 (2009)
115. J Wintterlin, M L Bocquet *Surface Sci.* **603** 1841 (2009)

116. M Moors, H Amara, T V de Bocarme, C Bichara, F Ducastelle *ACS Nano* **3** 511 (2009)
117. M Eizenberg, J M Blakely *Surface Sci.* **82** 228 (1979)
118. V K Portnoi, A V Leonov, S N Mudretsova, S A Fedotov *Phys. Met. Metall.* **109** 153 (2010) [*Fiz. Met. Metalloved.* **109** 165 (2010)]
119. A E Galashev, V A Polukhin *Phys. Solid State* **55** 1733 (2013) [*Fiz. Tv. Tela* **55** 1620 (2013)]
120. A Y Galashev, V A Polukhin *Russ. J. Phys. Chem. A* **88** 995 (2014) [*Zh. Fiz. Khim.* **88** 997 (2014)]
121. V A Polukhin, N A Vatolin *Rasplavy* (4) 3 (1998) [b]
122. S S Gupta, R C Batra *J. Comput. Theor. Nanosci.* **7** 1 (2010)
123. V V Alyokhin, B D Annin, A V Babichev, S N Korobeinikov *Dokl. Phys* **58** 487 (2013)
124. P B Balbuena, J Zhao, S Huang *J. Nanosci. Nanotechnol.* **6** 1247 (2006)
125. E K Athanassiou, R N Grass, W J Stark *Nanotechnology* **17** 1668 (2006)
126. F Banhart, P H Redlich, P M Ajayan *Chem. Phys. Lett.* **292** 554 (1998)
127. B H Davis *Catal. Today* **84** 83 (2003)
128. D L Huber *Small* **1** 482 (2005)
129. A B M Giasuddin, S R Kanel, H Choi *Environ. Sci. Technol.* **41** 2022 (2007)
130. A H Lu, E L Salabas, F Schueth *Angew. Chem., Int. Ed.* **46** 1222 (2007)
131. S Enthaler, K Junge, M Beller *Angew. Chem., Int. Ed.* **47** 3317 (2008)
132. S Shylesh, V Schünemann, W R Thiel *Angew. Chem., Int. Ed.* **49** 3428 (2010)
133. P Qiu, C Jensen, N Charity, R Towner, C B Mao *J. Am. Chem. Soc.* **132** 17724 (2010)
134. Z Chen, G S Hong, H L Wang, K Welsher, S M Tabakman, S P Sherlock *ASC Nano* **6** 1094 (2012)
135. J Y Dai, J M Lauerhaas, A A Setlur, R P H Chang *Chem. Phys. Lett.* **258** 547 (2006)
136. J Jiao, S Seraphin *J. Appl. Phys.* **83** 2442 (1998)
137. A K Schaper, H Hou, A Greiner, R Schneider, F Phillipp *Appl. Phys. A* **78** 73 (2004)
138. C Mattevi, H Kim, M Chhowalla *J. Mater. Chem.* **21** 3324 (2011)
139. S Wang, X Huang, Y He, H Huang, Y Wu, L Hou, X Liu, T Yang, J Zou, B Huang *Carbon* **50** 2119 (2012)
140. F Kh Urakaev, V S Shevchenko, N P Pokhilenko *Mendeleev Commun.* **20** 95 (2010)
141. X Li, W Kang, B Xi, Y Yan, H Bi, Y Zhu, Y Qian *Carbon* **48** 464 (2010)
142. J C Lo, J C Lu, M H Teng *Diamond Relat. Mater.* **20** 330 (2011)
143. N Sano, H Akazawa, T Kikuchi, T Kanki *Carbon* **41** 2159 (2003)
144. Q F Liu, W C Ren, Z G Chen, B L Liu, B Yu, F Li *Carbon* **46** 1417 (2008)
145. S Manzetti *Adv. Manuf.* **1** 198 (2013)
146. Y Hayashi, T Tokunaga, T Iijima, T Iwata, G Kalita, M Tanemura, K Sasaki, K Kuroda *Nanoscale Res. Lett.* **7** 448 (2012)
147. D Obergfell, J C Meyer, M Haluska *Phys. Status Solidi, B* **243** 3430 (2006)
148. M D Gimenez-Lopez, A Chuvilin, U Kaiser *Chem. Commun.* **47** 2116 (2011)
149. J Li, H Kim, S J Kahng *Nature (London)* **415** 1005 (2002)
150. A La Tore, M D Gimenez-Lopez, M W Fay *ACS Nano* **6** 2000 (2012)
151. G Caruntu, D Caruntu, C J O'Connor *Scanning Microscopy for Nanotechnology. Techniques and Applications* (Ed U Zhu, Zh L Uanga) (New York: Springer Science + Business Media, 2007)
152. V A Polukin, E D Kurbanova, A E Galashev *Russ. Metallurgy (Metally)* (8) 633 (2014) [*Rasplavy* (3) 37 (2014)]
153. P A Khomyakov, G Giovannetti, P C Rusu, G Brocks, J van den Brink, P J Kelly *Phys. Rev., B* **79** 195425 (2009)
154. P A Khomyakov, A A Staricov, G Brocks, P J Kelly *Phys. Rev., B* **82** 115437 (2010)
155. C J Gong, G Lee, B Shan, E M Vogel, R M Wallace K Cho *J. Appl. Phys.* **108** 123711 (2010)
156. H B Mchaelson *J. Appl. Phys.* **48** 4729 (1977)
157. C J Gong, D Hinojos, W C Wang, N Nijem, B Shan, R M Wallace, K Cho, Y J Chabal *ACS Nano* **6** 5381 (2012)
158. R E Smallman, R J Bishop *Modern Physical Metallurgy and Materials Engineering: Science, Process, Applications* (Oxford, Boston, Melbourne: Butterforth-Heinemenn, Elsevier, 1999)
159. V A Polukhin, E D Kurbanova *Russ. J. Phys. Chem. A* **89** 531 (2015) [*Zh. Fiz. Khim.* **89** 533 (2015)]
160. *Fizicheskaya Entsiklopediya* (Physical Encyclopedia) (Moscow: Bol'shaya Ross. Entsiklopediya, 1988 – 1998) Vols 1 – 5, p. 587
161. C Oshima, A J Nagashima *J. Phys.: Condens. Matter* **9** 1 (1997)
162. W Liu, J Wei, X Sun, H Yu *Crystals* **3** 257 (2013)
163. G Henkelman, A Arnaldsson, H Jonsson *Comput. Mater. Sci.* **36** 354 (2006)
164. A E Galashev, V A Polukhin *Phys. Solid State* **55** 2368 (2013)
165. S Numazava, M Ranjan, K-H Heining, S Facsko, R Smith *J. Phys.: Condens. Matter* **23** 222203 (2011)
166. S Barraza-Lopez, M Vanevic, M Kindermann, M Y Chou *Phys. Rev. Lett.* **104** 076807(2010)
167. J Tersoff *Phys. Rev. Lett.* **61** 2879 (1988)
168. J Tersoff *Phys. Rev. B* **39** 5566 (1989)
169. M Moseler, F Cervantes, S Hofmann, G Csanyi, A C Ferrari *ACS Nano* **4** 7587 (2010)
170. S J Stuart, A V Tutein, J A Harrison *J. Chem. Phys.* **112** 6472 (2000)
171. M C F Wander, K L Shuford *J. Phys. Chem.* **114** 20539 (2010)
172. S Yu Davydov *Phys. Solid State* **54** 875 (2012) [*Fiz. Tv. Tela* **54** 821 (2012)]
173. G K White, S J Collocott *J. Phys. Chem. Ref. Data* **13** 1251 (1984)
174. J Hu, X Ruan, Y P Chen *Nano Lett.* **9** 2730 (2009)
175. D W Brenner *Phys. Rev. B* **42** 9458 (1990)
176. K V Zakharchenko, A Fasolino, J H Los, M I Katsnelson *J. Phys: Condens. Matter* **23** 202202 (2011)
177. J H Los, L M Ghiringhelli, E J Meijer, A Fasolino *Phys. Rev. B* **72** 214102 (2005)
178. S Erkoc, B Gunes, P Gunes *Int. J. Modern. Phys. C* **11** 1013 (2000)
179. T Cagin, G Dereli, M Uludogan, M Tomak *Phys. Rev., B* **59** 3468 (1999)
180. S K Nayak, S N Khanna, B K Rao, P Jena *J. Phys. Chem. A* **101** 1072 (1997)
181. H-Y Song, X-W Zha *Commun. Theor. Phys. (Beijing, China)* **54** 143 (2010)
182. Y Shibuta, J A Elliott *Chem. Phys. Lett.* **472** 200 (2009)
183. H Rafii-Tabar *Phys. Rep.: Rev. Sect. Phys. Lett.* **325** 240 (2000)
184. A H Castro Neto, F Guinea, N M R Peres, K S Novoselov, A K Geim *Rev. Modern. Phys.* **81** 109 (2009)
185. K S Novoselov, A K Geim, S V Morozov, D Jiang, M I Katsnelson, I V Grigorieva, S V Dubonos, A A Firsov *Nature (London)* **438** 197 (2005)
186. Y H Chui, G Grochola, I K Snook, S P Russo *Phys. Rev., B* **75** 033404 (2007)
187. F R Negreiros, E A Soares, V E De Carvalho *Phys. Rev., B* **76** 205429 (2007)
188. J V Goloven'ko, Yu Ya Gafner, S L Gafner, L V Redel' *Phys. Met. Metall.* **114** 1038 (2013) [*Fiz. Met. Metalloved.* **114** 1041 (2013)]
189. K Boubaker *Mendeleev Commun.* **23** 160 (2013)
190. F Meng, R Cui, W Z Shen *J. Appl. Phys.* **90** 3387 (2001)

191. E Restrepo-Parra, C D Salazar-Enríquez, J Londoño-Navarro, J F Jurado, J Restrepo *J. Magn. Magn. Mater.* **323** 1477 (2011)
192. E Rozenberg, M Ausilender, I Felner, A Shames, G Gorodetsky, Y M Mukovskii *IEEE Trans. Magn.* **46** 1299 (2010)
193. Y Chen, B G Ueland, J W Lynn, G L Bychkov, S N Barilo, Y M Mukovskii *Phys. Rev., B* **78** 212301(2008)
194. G-W Wu, K-Y Chan *Surface Sci.* **365** 38 (1996)
195. S-P Huang, P B Balbuena *Mol. Phys.* **100** 2165 (2002)
196. S Iijima, T Ichihashi *Nature (London)* **363** 603 (1993)
197. T W Ebbesen, P M Ajayan *Nature (London)* **358** 220(1992)
198. P N D'yachkov *Elektronnye Svoistva i Primenenie Nanotrubok* (Electronic Properties and Application of Nanotubes) (Moscow: Binom. Laboratoriya Znanii, 2010)
199. L Sheng, A Jin, L Yu *Mater. Lett.* **81** 222 (2012)
200. S Ghosh, I Calizo, D Teweldebrhan, E P Pokatilov, D L Nika, A A Balandin, W Bao, F Miao, C N Lau *Appl. Phys. Lett.* **92** 151911 (2008)
201. A E Galashev, V A Polukhin *Colloid J.* **73** 761 (2011) [*Kolloid. Zh.* **73** 764 (2011)]
202. O A Novruzova, O P Rakhmanova, A E Galashev *Russ. J. Phys. Chem. A* **81** 1825 (2007) [*Zh. Fiz. Khim.* **81** 2033 (2007)]
203. A E Galashev, V A Polukhin, I A Izmodenov, O P Rakhmanova *Glass Phys. Chem.* **33** 86 (2007) [*Fiz. Khim. Stekla* **33** 119 (2007)]
204. S-H Kim, G Medeiros-Ribeiro, D A A Ohlberg, R Stanley Williams, J R Heath *J. Phys. Chem. B* **103** 10341 (1999)
205. M Brongersma *Nat. Mater.* **2** 296 (2003)
206. L R Hirsch, J B Jackson, A Lee, N J Halas *Anal. Chem.* **75** 2377 (2003)
207. Q Sun, O Wang, B K Rao, P Jena *Phys. Rev. Lett.* **93**186803 (2004)
208. W-T Chan, R Fournier *Chem. Phys. Lett.* **315** 257 (1999)
209. G-F Zhao, L-L Zhi, L-J Guo, Z Zeng *J. Chem. Phys.* **127** 234705 (2007)
210. P Tangney, S Scandolo *J. Chem. Phys.* **117** 8898 (2002)
211. L A Girifalco, V G Weizer *Phys. Rev.* **114** 687 (1959)
212. C Tautermann, D Clery *Phys. Chem. Chem. Phys.* **8** 1437 (2006)
213. H L Lemberg, F H Stillinger *J. Chem. Phys.* **62** 1677 (1975)
214. A Rahman, F H Stillinger, H L Lemberg *J. Chem. Phys.* **63** 5223 (1975)
215. A Le Bail *J. Appl. Cryst.* **38** 389 (2005)
216. N I Vakula, G M Kuramshina, Yu A Pentin *Russ. J. Phys. Chem. A* **87** 296 (2013) [*Zh. Fiz. Khim.* **87** 301 (2013)]
217. M Ocana, V Fornes, J V Garcia Ramos, C J Serna *Phys. Chem. Miner.* **14** 527 (1987)
218. A E Galashev, V A Polukhin *J. Surf. Invest.* **8** 1082 (2014)
219. D A Drabold, S Klemm, O F Sankey, in *Atomic Scale Calculations of Structure in Materials (Ser. Materials Research Society Symposium Proceedings* Vol. 193) (Pittsburg, PA: Materials Research Soc., 1990) p. 177
220. N A Borshch, N S Pereslavtseva, S I Kurganskii *Semiconductors* **40** 1423 (2006) [*Fiz. Tekhn. Poluprovod.* **40** 1457 (2006)]
221. W M M Kessels, M C M van de Sanden, D C Schram *Appl. Sci. Technol.* **16** 3199 (1998)
222. H Murakami, T Kanayama *Appl. Phys. Lett.* **67** 2341(1995)
223. M O Watanabe, H Murakami, T Miyazaki, T Kanayama *Appl. Phys. Lett.* **71** 1207 (1997)
224. K Raghavachari *J. Chem. Phys.* **96** 4440 (1992)
225. A E Galashev *Semiconductors* **42** 596 (2008) [*Fiz. Tekhn. Poluprovod.* **42** 611 (2008)]
226. V P Meleshko, Y N Morokov, V A Schveigert *Chem. Phys. Lett.* **300** 118 (1999)
227. M Rohlfing, S G Louie *Phys. Rev. Lett.* **80** 3320 (1998)
228. G A Rechtsteiner, O Hampe, M F Jarrold *J. Chem. Phys.* **105** 4188 (2001)
229. A Ye Galashev, V A Polukhin, in *Computer Investigation of the Stability and Structure of Si and SiO_2 Nanoparticles* (New York: Nova Sci. Publ., 2012) p. 130
230. A Filipponi, A Dicucco, M Benfatto, C R Natoli *Europhys. Lett.* **13** 319 (1990)
231. E F Cheka, E A Nikitina *Dokl. Chem.* **378** 129 (2001) [*Dokl. Akad. Nauk* **378** 208 (2001)]
232. A B Filonov, A N Kholod, V E Borisenko *Phys. Rev., B* **57** 1394 (1998)
233. B Yu, M Meyapan *Solid-State Electron.* **50** 536 (2006)
234. Zh Xiao *J. Micromech. Eng.* **10** 2014 (2006)
235. K D Wise *Sens. Actuators, A* **136** 39 (2007)
236. N Mousseau, L J Lewis *Phys. Rev., B* **43** 9810 (1991)
237. L Zhang, S Jiang *J. Chem. Phys.* **117** 1804 (2002)
238. *Spravochnik Khimika* (Chemist's Handbook) Vol. 1 (Ed. V P Nikol'skii) (Leningrad: Khimiya, 1971)
239. R Bellisent, A Menelle, W S Howells, A C Wright, T M Brunier, R N Sinclair, F Jansen *Physica B* **156** 217 (1989)
240. T Hawa, M R Zachariah *J. Chem. Phys.* **121** 9043 (2004)
241. C R Miranda, A Antonelli *J. Chem. Phys.* **120** 11672 (2004)
242. M A Leontovich *Vvedenie v Termodinamiku. Statisticheskaya Fizika* (Introduction to Thermodynamics. Statistical Physics) (St Petersburg: Fizmatlit, 2008)
243. Y Kawazoe, T Kondow, K Ohno *Clusters and Nanomaterials. Theory and Experiment* (Berlin: Springer, 2002)
244. K Nishio, T Morishita, W Shinoda, M Mikami *Phys. Rev., B* **72** 24532 (2005)
245. V P Skripov, V P Koverda *Spontannaya Kristallizatsiya Pereokhlazhdennykh Zhidkostei* (Spontaneous Crystallization of Supercooled Liquids) (Moscow: Nauka, 1984)
246. A E Galashev, V A Polukhin, I A Izmodenov, O R Rakhmanova *Glass Phys. Chem.* **32** 99 (2006) [*Fiz. Khim. Stekla* **32** 137 (2006)]
247. R B Murphy, D M Philipp, R A Friesner *J. Comput. Chem.* **21** 1442 (2000)
248. P Plufgradt, M Matthes, F Bechstedt *Phys. Rev. B* **89** 155418 (2014)
249. M T Yin, M L Cohen *Phys. Rev., B* **26** 5668 (1982)
250. A E Galashev, I A Izmodenov *Glass Phys. Chem.* **34** 173 (2008) [*Fiz. Khim. Stekla* **34** 222 (2008)]
251. I Kwon, R Biswas, C M Soukoulis *Phys. Rev. B* **45** 3332 (1992)
252. B M Baloyan, A G Kolmakov, M I Alymov, A M Krotov *Klassifikatsiya, Osobennosti Svoistv, Primenenie i Tekhnologii Polucheniya Nanomaterialov* (Classification, Characteristics of Properties, Application and Production Technologies of Nanomaterials) (Moscow: Dubna International University for Nature, Society and Man, 2007)
253. P Vogt, P De Padova, C Quaresima, J Avila, E Frantzeskakis, M C Asensio, A Resta, B Ealet, G Le Lay *Phys. Rev. Lett.* **108** 15550 (2012)
254. M E Davila, L Xian, S Cahangirov, A Rubio, G Le Lay *New J. Phys.* **16** 095002 (2014)
255. Y Xu, B Yan, H-J Zhang *Phys. Rev. Lett.* **111** 136804 (2013)
256. J Gao, J Zhao *Sci. Rep.* **2** 861 (2012)
257. P Ballet, C Thomas, X Baudry, C Bouvier, O Crauste, T Meunier, G Badano, M Velleret, J P Barnes, P H Jouneau, L P Levi *J. Electron. Mater.* **43** 2954 (2014)
258. S Kwon, M Kang *J. Korean Phys. Soc.* **61** 589 (2012)
259. R Quhe, Y Yaun, J Zheng, Y Wang, Z Ni, J Shi, D Yu, J Yang, J Lu *Sci. Rep.* **4** 5476 (2012)
260. E N Voloshina, A V Generalov, M Wesser, S Bottcher, K Horn, Y S Dedkov *New J. Phys.* **13** 113028 (2011)
261. N Ligato, A Cupolillo, L S Caputi *Thin Solid Films* **543** 59 (2013)
262. A V Generalov, E N Voloshina, Y S Dedkov *Appl. Surf. Sci.* **267** 8 (2013)
263. N E Dubinin, L D Son, N A Vatolin *J. Phys.: Condens. Matter* **20** 114111 (2008)

[a] — *Nanotechnol. Russ. (Engl. Transl.)*
[b] — *Russ. Metallurgy (Metally) (Engl. Transl.)*